

**Engineering Dissipation to Generate Entanglement Between Remote
Superconducting Quantum Bits**

by

Mollie Elisheva Schwartz

A dissertation submitted in partial satisfaction of the
requirements for the degree of
Doctor of Philosophy

in

Physics

in the

Graduate Division

of the

University of California, Berkeley

Committee in charge:

Professor Irfan Siddiqi, Chair
Professor Holger Müller
Professor K. Birgitta Whaley

Fall 2016

**Engineering Dissipation to Generate Entanglement Between Remote
Superconducting Quantum Bits**

Copyright 2016
by
Mollie Elisheva Schwartz

Abstract

Engineering Dissipation to Generate Entanglement Between Remote Superconducting
Quantum Bits

by

Mollie Elisheva Schwartz

Doctor of Philosophy in Physics

University of California, Berkeley

Professor Irfan Siddiqi, Chair

Superconducting quantum circuits provide a promising avenue for scalable quantum computation and simulation. Their chief advantage is that, unlike physical atoms or electrons, these “artificial atoms” can be designed with nearly-arbitrarily large coupling to one another and to their electromagnetic environment. This strong coupling allows for fast quantum bit (qubit) operations, and for efficient readout. However, strong coupling comes at a price: a qubit that is strongly coupled to its environment is also strongly susceptible to losses and dissipation, as coherent information leaks from the quantum system under study into inaccessible “bath” modes. Extensive work in the field is dedicated to engineering away these losses to the extent possible, and to using error correction to undo the effects of losses that are unavoidable.

This dissertation explores an alternate approach to dissipation: we study avenues by which dissipation itself can be used to generate, rather than destroy, quantum resources. We do so specifically in the context of quantum entanglement, one of the most important and most counter-intuitive aspects of quantum mechanics. Entanglement generation and stabilization is critical to most non-trivial implementations of quantum computing and quantum simulation, as it is the property that distinguishes a multi-qubit quantum system from a string of classical bits. The ability to harness dissipation to generate, purify, and stabilize entanglement is therefore highly desirable.

We begin with an overview of quantum dissipation and measurement, followed by an introduction to entanglement and to the superconducting quantum information architecture. We then discuss three sets of experiments that highlight and explore the powerful uses of dissipation in quantum systems. First, we use an entangling measurement to probabilistically generate entanglement between two qubits separated by more than one meter of ordinary cable. This represents the first achievement of remote entanglement in a superconducting qubit system, which will be a critical capability as quantum computers and simulators scale. We then use a nearly-quantum limited amplifier to unravel individual quantum trajectories of the system under that entangling measurement, performing the first systematic explo-

ration of entangled trajectories in any physical implementation. We finally demonstrate deterministic entanglement by engineering a lossy quantum environment to efficiently generate and stabilize entangled states with both frequency and symmetry selectivity. These experiments provide evidence that explicitly building dissipation into an engineered quantum system can enable, rather than hinder, the study of fundamental quantum mechanics and complex many-body Hamiltonians.

Nothing works unless you do.
Maya Angelou

Contents

Contents	ii
List of Figures	v
1 Introduction	1
1.1 Superconducting Qubits	2
1.2 Strong Coupling: A Blessing and a Curse	3
1.3 Complementary Approaches to Dissipation	4
1.4 Overview and Summary of Results	5
2 Dissipation and Continuous Measurement	7
2.1 Introduction to Weak Quantum Measurements	8
2.1.1 Projective Measurements	8
2.1.2 The Stern-Gerlach Experiment: Projective Regime	9
2.1.3 The Stern-Gerlach Experiment: Weak Measurement Regime	11
2.2 The Quantum Bayesian Formalism	14
2.3 The Stochastic Master Equation	16
2.3.1 Dissipation via Fluctuation: Lindblad Operators	17
2.3.2 Measurement in the SME formalism	19
2.4 Measurement Rate and Inefficient Measurements	20
2.5 Summary of Measurement and Dissipation	22
3 Entanglement: A Primer	23
3.1 Introduction to Entanglement	24
3.2 Defining Entanglement	25
3.3 Useful Measures of Entanglement	26
3.3.1 Von Neumann entanglement entropy	26
3.3.2 Entanglement of formation	27
3.3.3 Entanglement witnesses	28
3.3.4 CHSH measurement	28
3.3.5 Tomographic methods	29

4 The Superconducting cQED Architecture	32
4.1 Superconducting Qubits	33
4.1.1 The transmon qubit	34
4.2 The Jaynes Cummings Hamiltonian	37
4.2.1 Derivation	37
4.2.2 Near-resonant case	38
4.2.3 Dispersive (far-detuning) limit	39
4.3 Dispersive Readout	40
4.3.1 Semiclassical treatment	41
4.3.2 Coherent states and measurement uncertainty	42
4.3.3 Unconditioned master equation	43
4.3.4 Dispersive measurement: Bayesian approach	46
4.3.5 Dispersive measurement: Master equation approach	47
4.4 Parametric Amplification	48
4.4.1 The lumped Josephson parametric amplifier	49
4.4.2 Phase-sensitive amplification	50
4.5 Summary: The Superconducting Qubit Toolbox	52
5 Remote Measurement-Induced Entanglement	53
5.1 Historical Perspective	54
5.2 Design of an Entangling Continuous Measurement	56
5.2.1 Joint dispersive measurement	56
5.2.2 Tuning the entangling measurement	59
5.2.3 Verification of the half-parity measurement	60
5.3 Bayesian Theory of the Entangling Measurement	60
5.4 Full Calibration of the Experimental Apparatus	64
5.4.1 Detailed experimental setup	65
5.4.2 Cavity parameters	65
5.4.3 Qubit lifetimes and coherences	67
5.4.4 Calibration of photon number, dispersive shifts, and inter-cavity transmission efficiency	67
5.4.5 Calibration of η_{meas}	68
5.5 Tomographic Reconstruction of Entanglement Dynamics	69
5.5.1 Characterizing the tomographic reconstruction	71
5.5.2 Entanglement dynamics	74
5.6 Discussion of Results	77
6 Quantum Trajectories	79
6.1 Experimental Generation and Verification of Entangled Trajectories	80
6.1.1 Generating quantum trajectories	81
6.1.2 Validating the quantum trajectories	82
6.2 Statistical Properties of Concurrence Trajectories	85

6.2.1	Concurrence-readout relationship	85
6.2.2	Probability density function for concurrence trajectories	87
6.2.3	Distribution of time to maximum concurrence	90
6.3	Conclusion	91
7	Symmetry-Selective Bath Engineering	93
7.1	Experimental Design and Protocol	94
7.1.1	Entangling protocol	95
7.1.2	Symmetry-selectivity of protocol	98
7.2	Theoretical Treatment of the Bath Drives	98
7.2.1	Dynamics	100
7.2.2	Effective driven-dissipative XY model	100
7.2.3	Protocol for generating entanglement	104
7.3	Full Experimental Calibration	106
7.3.1	Detailed Experimental Setup	106
7.3.2	Coupling of the cavities	108
7.3.3	Qubit parameters	109
7.3.4	Path length calibration	111
7.3.5	Balancing the cooling drive amplitudes	111
7.3.6	Tomography calibration	113
7.4	Experimental Implementation of the Bath Engineering Protocol	115
7.5	Discussion	118
8	Conclusions and Outlook	120
8.1	Extensions of Measurement-Induced Entanglement	121
8.2	Further Applications of Dissipation-Induced Entanglement	122
Bibliography		124

List of Figures

2.1	Stern-Gerlach Experiment (Strong)	11
2.2	Stern-Gerlach Experiment (Weak)	12
4.1	Josephson Junctions	33
4.2	Cooper Pair Box Spectrum	35
4.3	Transmon Qubit	36
4.4	cQED Readout Schematic	41
4.5	Dispersive measurement	44
4.6	Lumped Josephson Parametric Amplifier	50
4.7	Phase-Sensitive Amplification	51
5.1	Hong-Ou-Mandel Effect	55
5.2	Simplified experimental setup	57
5.3	Sequential joint dispersive measurement	58
5.4	Choosing an operating frequency	59
5.5	Fiducial state readout histograms	61
5.6	Full experimental setup	66
5.7	\bar{n} , η_{loss} , and χ calibration	68
5.8	Calibration of η_{meas} and G_{chain}	69
5.9	Pulse sequence for entanglement generation and verification	70
5.10	Tomography calibration	74
5.11	Entangled density matrix dynamics	75
5.12	Selected full density matrices	76
5.13	Evolution of concurrence of entangled state	76
6.1	Modified setup for trajectories	80
6.2	Conditional tomography at fixed time	83
6.3	Full tomographic mapping	84
6.4	An exemplar quantum trajectory	85
6.5	Readout histograms	87
6.6	Concurrence probability distribution function	88
6.7	Time-to-maximum concurrence distribution	90

7.1	Base-Temperature Schematic	94
7.2	Avoided crossings in cavity and qubit sectors	96
7.3	Protocol for symmetry-selective cooling	97
7.4	Detailed experimental setup	107
7.5	Calibration of g and χ	110
7.6	Path length calibration	112
7.7	Cooling drive amplitude calibration	113
7.8	Tomography pulse crosstalk calibration	114
7.9	Pulse sequence for entanglement generation and verification	115
7.10	Demonstration of symmetry- and frequency- selective bath engineering	116
7.11	Cooling dynamics	117

Acknowledgments

Graduate school is alternately an exhilarating, terrifying, rejuvenating, depressing, elating, anxiety-baiting, and confidence-building experience - and often, it is all of these things simultaneously. I am so grateful for the network of people that bolstered me through the last five years. I have grown tremendously as a woman and as a scientist, and I have many people to thank for shepherding me through this process.

Professionally and scientifically, I could not have asked for a more competent, generous, and supportive group of people to work with than the members of the Quantum Nanoelectronics Laboratory. Of course the credit for this begins with our adviser Irfan Siddiqi, whose scientific acumen, collegiality, and thoughtful leadership set the tone for our group. I have enjoyed our technical, strategic, and personal conversations over the years, and you have set a strong example for what a career in science can become. I'm particularly thankful to Chris Macklin, who answered many stupid questions during my first year in lab; to Nicolas Roch, with whom I spent many mornings, evenings, and weekends fighting with microwaves and qubits and from whom I learned a great deal technically and professionally; to Leigh Martin and Manu Flurin, who engineered baths with me and helped me pull off an extraordinary eleventh-hour result; and to the entire group, for demonstrating that openness, curiosity, teamwork, ambition, and mutual support can grow and thrive in an academic setting.

I also must acknowledge the people who guided me along the path to graduate school. The Pennsylvania Governor's School for the Sciences gave me an early taste of rigorous scientific study and physics research, and I am so glad that this program has survived budget cuts and economic downturns through the heroic work of the PGSS Alumni Association. Prof. Tom Solomon, my first research adviser during my undergraduate degree, treated me as a colleague, and gave me room to experiment, fail, and grow. He taught me to be technically creative and resourceful, skills that have carried through my career. Horst Stormer, Philip Kim, and Erik Henriksen introduced me to the excitement of research at the forefront of a "hot" field, and have served as mentors and friends in the years since. I am also grateful to my colleagues at the Science and Technology Policy Institute, particularly Sarah Ryker, Sarah Rees, and Jason Gallo, for giving me the opportunity to explore the role and limitations of science in society at large.

I am deeply grateful to the Fannie and John Hertz Foundation, which funded my graduate degree. The Hertz fellowship represents far more than the financial means to pursue a Ph.D.: it also has provided professional development to build an expanded perspective about scientific career paths, and an invaluable community of peers and alumni who have provided commiseration, perspective, and reinforcement throughout the course of my degree. I have loved being a part of this community, and hope to benefit from and give back to it over the course of my career.

Physics can be a lonely enterprise for women, and even more so for other under-represented minorities. I am grateful for the talented, brilliant, sassy women with whom I found solidarity and inspiration: Natania Antler, Sydney Schreppler, Allison Dove, Kristi Beck, Tova Holmes, Kate Kamdin, Abi Polin, Hilary Jacks, Simca Bouma, Tess Smidt, Shawna Seth, Justine

Sherry, and so many others. Our afternoon teas, evening ports, and weekend brunches brought levity and lightness to my time at Berkeley, and I look forward to seeing the paths you travel.

The support of my family has been central to my success and happiness over the last five years. My parents, Jan and Elaine, never doubt my abilities, and help give me confidence to push myself deeper and farther into my work. My brothers, Eben, Isaac, and David, keep me grounded and provide comic relief in themselves, their fabulous spouses (Kate, Elyse, and Joni, who are sisters to me), and their adorable children (Margot, Asa, Haim, Lida, and counting). And the influence of my grandparents Howard, Harriet and Mary, whom I miss very much, reverberates in my life and my profession. I am so grateful for the example they set with their lives and their counsel.

Finally, to my husband Itamar. I never would have imagined that going to the Physics Social Hour to relax after handing in a problem set would lead to meeting the love of my life and kicking off a lifetime adventure together. Thank you for your love, support, patience, compassion, company, laughter, and strength. We have stuck together through different cities, opposite coasts, late nights, early mornings, high moments and low, and I can't imagine doing any of this without you.

Chapter 1

Introduction

All the mental effort of an assiduous investigator must indeed appear vain and hopeless, if he does not occasionally run across striking facts which form incontrovertible proof of the truth he seeks, and show him that after all he has moved at least one step nearer to his objective.

Max Planck, *The Origin and Development of the Quantum Theory*,
1920

Entanglement is perhaps the most puzzling component of quantum theory, one that challenges classical conceptions of causality and locality. Two quantum objects that are entangled with one another carry coherent quantum information in their joint correlations, rather than in their individual states. The information shared between the two quantum systems remains entangled, even if the systems are separated by light years. As a result, making a measurement of one of the system causes an instantaneous projection of the other. This “spooky action at a distance”, as famously described by (and philosophically reviled by) Albert Einstein, is at the heart of quantum physics.

In addition to the fascinating philosophical questions raised by the existence of entanglement, it also is fundamental to a number of very practical applications of quantum mechanics. Quantum computation, networking, cryptography, and simulation all rely on the ability to generate, manipulate, and measure entangled states. However, bringing entanglement out of the abstract world of thought-experiments and into the physical realm of experimental apparatuses requires us to grapple with the inevitable nonidealities of the physical world. Even the most highly-isolated quantum systems must interact with their environment in some way, and therefore gradually lose information to it in dissipative processes. Moreover, a perfectly isolated and noninteracting quantum object by definition cannot be measured, and therefore cannot be useful for the study of fundamental physics or for more practical applications. We therefore need to develop an understanding of how noisy processes affect entangled states.

In this dissertation, we will explore the interfaces between entanglement, measurement, and dissipation. We will see that entanglement is critical to the process of measurement, even as measurement of an entangled state generally destroys that entanglement. We will also discover that dissipation and measurement are complementary processes: they both involve carrying information away from a quantum system, and either observing or losing that information. We will then describe a series of experiments that demonstrate the potential for noisy processes to serve as a resource for generating and stabilizing entanglement. We will do all of this in the context of the superconducting quantum circuit architecture, which represents a promising approach to scalable quantum experiments.

1.1 Superconducting Qubits

In order to study fundamental quantum mechanics or to work toward a practical quantum computer or simulator, we must move beyond the realm of *gedanken* experiments and build a physical apparatus for trapping, stabilizing, and manipulating single quantum degrees of freedom. Deep interest in exploring the details of quantum physics has led to an explosion of experimental efforts dedicated to designing and perfecting long-lived, addressable quantum systems. This is no mean task: we do not feel quantum effects in daily life because quantum information is quickly destroyed when a coherent quantum system is brought into contact with the larger classical world occupied by bulk experimental equipment and brutish, macroscopic physicists.

Most practical quantum systems are based around conceptual building blocks of quantum systems that are restricted to two levels. In analogy with classical computational building blocks, these are known as quantum bits, or qubits: these are two-level quantum systems that, unlike their classical binary counterparts, are able to exist in a superposition of their two states and to become entangled with one another so that information is distributed across the entire qubit array. There are a broad range of physical qubit implementations, all of which have advantages and disadvantages. A number of quantum information implementations, including trapped ions [1–6], neutral atoms [7–11], nitrogen-vacancy (NV) centers in diamond [12, 13], and semiconductor quantum dots [14–16] utilize a physical atom or electron to carry quantum information. The advantage of these approaches is that the system under study is inherently a fully quantum object, whose well-defined energy levels are unevenly spaced such that individual transitions can be readily and uniquely addressed. However, electrons and atoms are inherently tiny, and have a small scattering cross-section. Generating large dipole interactions between the qubit and a macroscopic electromagnetic measurement apparatus can therefore be quite challenging [17–19]. Similarly, generating significant couplings between these spins in order to create entanglement can be difficult; these systems typically require relatively long gate times.

Superconducting qubits [20–22], the physical system that we will use to study quantum physics in this dissertation, represent an artificial atom generated from the collective behavior of Cooper pairs as they tunnel across a weak barrier. The superconducting qubit is a

macroscopic object that, rather amazingly, behaves like a single quantum degree of freedom. Because of its macroscopic nature, it is straightforward to design the superconducting qubit circuit to have an intrinsically large dipole moment: its physical extent can be on the order of millimeters (in comparison to the nanometer-sized dipole of a physical atom). As we will see in Chapter 4, the designability of the form factor in the superconducting qubit is one of its chief strengths and defining features. The strong coupling limit, in which the qubit-cavity coupling g_{qc} is larger than the cavity leakage rate κ and the qubit decay rate γ can be met using superconducting qubits with minimal design effort.

1.2 Strong Coupling: A Blessing and a Curse

The inherent strong coupling in the superconducting qubit architecture is one of its greatest strengths. The ease of generating strong interactions means that performing single-shot qubit state readout mediated by a cavity (Chapter 4.3) is relatively straightforward [9, 23–25]. In addition, two-qubit gates can be accomplished quickly: qubits that can be strongly coupled to the environment can also be strongly-coupled to one another, either directly or via cavity-mediated coupling [26–31]. As a result, single- and multiple-qubit gates can be performed on the nanosecond timescale. The ease of readout and tunable multi-qubit coupling have made superconducting qubits one of the most promising avenues for scalable quantum computation. This is evidenced by growing investment in the technology on the part of profit-driven industrial leaders, building on decades of fundamental research in universities and national laboratories.

While strong coupling is critical to the operation of superconducting qubits, it also comes with significant drawbacks. Superconducting qubits couple not only to one another and to a carefully engineered readout mechanism: they couple strongly to virtually everything! Although the collective behavior of Cooper pairs in an aluminum substrate causes them to act like a single quantum object, the physical circuit can extend over hundreds of micrometers to millimeters. The qubit interacts with defects in the silicon or sapphire substrate, with impurities in the superconductor, with quasiparticle excitations, with residual photons in the cavity, and with any number of other spurious quantum systems that form the qubit’s environment. These local interactions carry quantum information away from the system, storing it instead in “bath” modes. This information still exists, but it is no longer in a form that the experimenter can capture or utilize; from our perspective, it is lost. Often, these inaccessible degrees of freedom fluctuate stochastically: as qubits interact with a noisy variable, they themselves take on random behavior that makes it increasingly difficult to reliably prepare and maintain a desired state.

From the standpoint of the observer, local interactions that cannot be detected appear as dissipation, or lost information. Dissipation generally manifests as qubit decay (if the dissipation is caused by the qubit directly exchanging photons with a lossy mode) or as decoherence (if the interaction causes un-measured shifts in the qubit frequency). For superconducting qubits, state-of-the-art coherence times are in the tens to hundreds of microseconds [32–35].

This is orders of magnitude longer than the lifetime of coherent oscillations observed in the first Cooper pair box qubit [36], but still well short of the lifetimes in atomic systems. Qubit decoherence and decay puts a ceiling on the achievable fidelity of a quantum gate, which is performed in finite time. The effects of dissipation diminish the quality of quantum manipulations in operations that require multiple gates and a significant fraction of the qubit coherence times. As superconducting qubit circuits grow to include tens of qubits in increasingly sophisticated circuits, perhaps including several chips organized in a quantum network, dissipation therefore rapidly becomes a limiting effect.

1.3 Complementary Approaches to Dissipation

Dissipation, unsurprisingly, is almost universally viewed as the enemy of coherent quantum computation. Great efforts are taken to prevent, mitigate, and correct for the effects of dissipation. Historically, this has taken the form of improved microwave engineering [32, 37–40], intelligent sculpting of the electromagnetic environment [41, 42], and detailed materials study in order to limit quasiparticle and dielectric loss [43–49]. If the intrinsic error rate is sufficiently limited (even to 1% for some applications), it then becomes possible to introduce active error correction in order to extend the effective lifetime of the qubits and perform extended algorithms [50–52]. There are already a number of exciting experiments that implement active error correction [53–57].

In this dissertation, we will take a complementary and somewhat counterintuitive approach. We take dissipation as a given in our system, and explore ways in which we can actively *use* that dissipation as an asset, rather than as a liability. This is a methodology inspired by the axiom “if you can’t beat them, join them”: understanding that one can never fully eliminate dissipation from a physical system, it behooves us to find ways to explicitly build dissipation into our quantum protocols and take advantage of its presence. This dissertation will probe a number of powerful contexts in which dissipation can be channeled and harnessed to generate and stabilize entanglement between superconducting qubits. We focus particularly on generating entanglement between remote qubits.

We utilize dissipation in two primary ways, the first of which is in the form of measurement. It may be slightly odd at first to think of measurement as a form of dissipation. However, measurement, as we will see in Chapter 2, is achieved by entangling a quantum system of interest with a noisy degree of freedom, and then recording the fluctuations of that degree of freedom. From the standpoint of the quantum system, the dynamics are identical to information being dissipated in a lossy mode; the only difference is that when the observer monitors that lossy channel, she is able to reconstruct the effects of the dissipation and update her estimate of the quantum state accordingly. We will utilize a carefully designed measurement, coupled with a high-efficiency amplification chain, to probabilistically generate entanglement between remote superconducting qubits. This is a critical capability: generating entanglement between quantum objects that do not directly interact with one another is not a trivial task, but may play an important role in a distributed quantum

network.

We are also interested in using purely dissipative protocols to generate entanglement. This approach is often referred to as “bath engineering” for its reliance on tailoring the spectrum of the lossy bath modes. Bath engineering, which originated in the ion trapping community [58, 59] and has seen a recent resurgence in the superconducting qubit community [60–64], typically relies on Raman-type scattering processes: we off-resonantly drive the bath mode(s) such that the detuning between the drive and the bath corresponds to a relevant transition in the qubit system. Suppose the drive is red-detuned from the bath: In order for a drive photon to dissipate into the bath, it must first absorb the requisite energy from the system in order to satisfy the conservation of energy. When the photon is absorbed in the bath, it projects the quantum system into its lower energy state. This is the equivalent of cooling the system. If instead the drive is blue-detuned from the bath, emitting a photon requires exciting a transition in the system, or bath-mediated heating. Should the system, via some other fluctuating interaction, decay to its original state, the drive re-pumps the system into the target state at a rate limited by the dissipation rate in the bath mode. Thus, bath engineering relies explicitly on dissipative processes in order to stabilize the quantum system into a target state. In this dissertation, we will use bath engineering to deterministically generate and stabilize entanglement, thus harnessing dissipation to preserve entanglement rather than to destroy it.

1.4 Overview and Summary of Results

In this dissertation, we explore the uses and limitations of dissipation, through the lens of generating entanglement in superconducting quantum systems. In Chapter 2, we will provide an introduction to a fully quantum treatment of dissipation, as well as to a more sophisticated mathematical and conceptual understanding of quantum measurement. In doing so, we will uncover the deep connections between dissipation and measurement, which will be critical for understanding the remainder of the dissertation. In Chapter 3, we will review quantum entanglement: what it is, what it is not, and how we can quantify it in a physical system. Chapter 4 is a broad overview of the constituents of the superconducting qubit toolbox: the Josephson junctions and transmon circuits that form the qubits we utilize in this dissertation; the coupling of those qubits to microwave cavities that we use to perform sensitive, non-demolition measurements; and the parametric amplifiers that we use to bring those measurements into the nearly quantum-limited regime.

In Chapters 5–7, we present a range of experiments in which we utilize dissipation to generate, stabilize, and study entanglement. Chapter 5 describes the first demonstration of entanglement between distant superconducting qubits: we house two qubits in cavities that are separated by more than one meter of ordinary copper cable, and use a finely-tuned measurement in order to probabilistically entangle them. In Chapter 6, we take a deep dive into this measurement-induced entanglement scheme: we use highly-sensitive quantum amplifiers to unravel the instantaneous back-action of the measurement on the cascaded qubit

system, peering into the ensemble to study the distribution of individual system trajectories. In Chapter 7, we utilize a purely dissipative protocol (requiring no measurement) to generate and stabilize bipartite entanglement. By engineering the symmetry of the dissipative environment, we are able to selectively stabilize entangled states of a dynamically tunable symmetry, while suppressing states of the opposite symmetry due to parity selection rules. This demonstrates the power of engineering not just the energetic density of states, but also the symmetry profile of lossy modes in a system. In Chapter 8, we discuss several avenues for future developments of this work.

The original work reported in Chapters 5-7 was initially published in the following publications:

- Chapter 5: Roch, N. et al. Observation of measurement-induced entanglement and quantum trajectories of remote superconducting qubits. *Phys. Rev. Lett.* 112, 170501 (2014).
- Chapter 6: Chantasri, A., Kimchi-Schwartz, M. E., Roch, N., Siddiqi, I. & Jordan, A. N. Quantum trajectories and their statistics for remotely entangled quantum bits. (2016). at <http://arxiv.org/abs/1603.09623>
- Chapter 7: 1. Kimchi-Schwartz, M. E. et al. Stabilizing Entanglement via Symmetry-Selective Bath Engineering in Superconducting Qubits. *Phys. Rev. Lett.* 116, 240503 (2016).

Other research undertaken and published during the course of the author's Ph.D training, but not substantially included in this dissertation, include:

- Macklin, C. et al. A near-quantum-limited Josephson traveling-wave parametric amplifier. *Science* 350, 307-10 (2015).
- Weber, S. J., Murch, K. W., Kimchi-Schwartz, M. E., Roch, N. & Siddiqi, I. Quantum trajectories of superconducting qubits. *Comptes Rendus Phys.* 17, 766-777 (2016).
- McClean, J. R., Kimchi-Schwartz, M. E., Carter, J. & de Jong, W. A. Hybrid Quantum-Classical Hierarchy for Mitigation of Decoherence and Determination of Excited States. (2016). <http://arxiv.org/abs/1603.05681>

Chapter 2

Dissipation and Continuous Measurement

[O]ne can hardly view the quantum theoretical description as a complete representation of the physically real. If one attempts, nevertheless, so to view it, then one must assume that the physically real in B undergoes a sudden change because of a measurement in A. My physical instincts bristle at that suggestion.

Albert Einstein, *Letter to Max Born*, 1948

This dissertation, at its heart, is an exploration of the connections between measurement and dissipation and the ways in which those connections can be harnessed. Quantum measurement is typically thought of as a process, more or less mysterious, that brings a system from an initial superposition state into a single, final state: an electron exists everywhere until it is detected, a quantum bit is simultaneously in its ground and excited state until it is stochastically projected into one or the other. Dissipation plays a similar role in reducing quantum coherence, by carrying quantum information away from the system under study and storing it instead in inaccessible environmental degrees of freedom. Key to both of these processes is a lack of fore-knowledge about what the ultimate state of the quantum system will be. One could therefore speculate that perhaps there is a connection between dissipative processes and measurement.

In this chapter, we will see that indeed, dissipation and measurement are intimately connected. We will show that measurement can be considered a special case of a dissipative process, one in which the environmental modes into which information dissipates can be monitored, and the information thus extracted and preserved. In order to elucidate this connection, we will require a more sophisticated understanding of quantum measurement, and particularly of *continuous* quantum measurement. We will begin with a phenomenological overview of quantum measurement in both the strong and weak regimes, and then will present two mathematical formalisms - the quantum Bayesian approach, and the stochastic

master equation - that allow us to treat and understand both measurement and dissipative processes. This will provide us with a foundation and a context for the studies of entanglement under measurement and dissipation that will follow in this dissertation.

2.1 Introduction to Weak Quantum Measurements

In a typical quantum mechanics course, measurements are introduced as an instantaneous, fully projective process. As we will see, this is a gross over-simplification of the physical processes that underlie an experimentally-realizable quantum measurement. However, it is useful to briefly review the physics of projective measurements in order to provide a starting point for the more complicated discussion of continuous measurements.

2.1.1 Projective Measurements

For a measurement operator \hat{A} with measurement outcomes a_n and non-degenerate eigenstates $|\psi_n\rangle$, we can construct projection operators $\Pi_n = |\psi_n\rangle\langle\psi_n|$. The postulates of quantum mechanics [66] then provide the following relations, for an arbitrary initial pure state $|\psi_i\rangle = \sum c_n |\psi_n\rangle$:

$$P_{a_n} = \frac{\langle\psi_i|\Pi_n|\psi_i\rangle}{\langle\psi_i|\psi_i\rangle}; \quad (2.1a)$$

$$\langle\hat{A}\rangle = \frac{\langle\psi_i|\hat{A}|\psi_i\rangle}{\langle\psi_i|\psi_i\rangle} = \sum_n a_n P_n; \quad (2.1b)$$

$$|\psi_f\rangle|_{a_n} = \frac{\Pi_n|\psi_i\rangle}{\sqrt{\langle\psi_i|\Pi_n|\psi_i\rangle}}. \quad (2.1c)$$

These postulates state that the probability of measurement outcome a_n is given by the normalized matrix product of the starting state with the n -th projector [Eq. (2.1a)]; that the expectation value of \hat{A} is given by the weighted sum of the measurement outcome probabilities [Eq. (2.1b)]; and that the final state of the system after measuring the outcome a_n is given by the n -th projector acting on the initial state [Eq. (2.1c)]. The final postulate represents the famous "collapse" postulate [67].

In order to discuss mixed states, it is useful to translate these postulates into the language of density matrices. The density matrix construction of these postulates, for arbitrary pure

or mixed initial density matrix ρ_i is given by the following:

$$P_{a_n} = \text{Tr}\{\rho_i \Pi_n\}; \quad (2.2a)$$

$$\langle \hat{A} \rangle = \text{Tr}\{\rho_i \hat{A}\}; \quad (2.2b)$$

$$\rho_f|_{a_n} = \frac{\Pi_n \rho_i \Pi_n}{\text{Tr}\{\Pi_n \rho_i \Pi_n\}}. \quad (2.2c)$$

In order to create a quantum *non-demolition* (QND) measurement, the eigenstates $|\psi_n\rangle$ of \hat{A} must be identical to the eigenstates of the unperturbed system Hamiltonian \hat{H}_0 . Equivalently, \hat{A} must commute with \hat{H}_0 . If $|\psi_n\rangle$ is a simultaneous eigenstate of \hat{H}_0 and \hat{A} , then a system that begins in an eigenstate of the un-measured Hamiltonian will be projected deterministically into that same state by the measurement operator. This is not to say that a QND measurement has no effect at all - if the system were to begin in a superposition of several eigenstates, the QND measurement would project it stochastically into one of the eigenstates, thus destroying the superposition. However, once the system is in one of those eigenstates, repeated measurements will not drive the system out of that state.

Thus far we have discussed only non-degenerate measurement operators. However, consider the case of a degenerate measurement operator, in which two or more eigenstates correspond to the same eigenvalue, or measurement outcome. This is particularly interesting in the QND case, as it implies that several eigenstates of \hat{H}_0 may generate the same measurement outcome. In this case, the measurement projects onto a multidimensional eigenspace \mathcal{E}_n , rather than onto a single eigenvector. The projection operator is built of a linear sum of eigenvectors that span \mathcal{E}_n , such that for $\{k | \hat{A} |\psi_k\rangle = a_n |\psi_k\rangle\}$,

$$\Pi_n = \sum_k \frac{|\psi_k\rangle\langle\psi_k|}{\langle\psi_k|\psi_k\rangle}. \quad (2.3)$$

This projection operator can be represented as a matrix whose rank corresponds to the degeneracy of the eigenspace. As we will see in Chapter 5, such a degenerate measurement can be exploited to project onto coherent superposition states, rather than onto a single eigenstate.

2.1.2 The Stern-Gerlach Experiment: Projective Regime

Until this point, we have discussed projection operators in their mathematical sense. But how do we physically implement a quantum measurement? The Stern-Gerlach experiment [68] is an oft-discussed example of a projective quantum measurement (Figure 2.1). In this experiment, a furnace is used to produce a collimated beam of silver (Ag) atoms, which have one unpaired electron that carries spin $S = 1/2$. The beam is unpolarized, and comprises an incoherent mixture of $|\uparrow\rangle$ and $|\downarrow\rangle$. The initial spin state of the beam can be represented

by a density matrix

$$\rho_{\text{spin}} = \begin{pmatrix} 1/2 & 0 \\ 0 & 1/2 \end{pmatrix}, \quad (2.4)$$

in a basis for which the eigenvectors are the $|\uparrow\rangle$ and $|\downarrow\rangle$ eigenstates of the Pauli spin matrix σ^Z . We will also need to account for spatial degrees of freedom, which we will indicate by a state $|\bar{z}\rangle$ where \bar{z} represents the expectation value of the vertical position of the beam. Since the beam is initially collimated, we can write the total density matrix as

$$\rho_i = \rho_{\text{spin}} \otimes \rho_z = \begin{pmatrix} 1/2 & 0 \\ 0 & 1/2 \end{pmatrix} \otimes |0\rangle\langle 0| \quad (2.5)$$

The collimated beam is passed through an inhomogeneous magnetic field \mathbf{B} , which interacts with the spins via the Zeeman effect:

$$U_{\text{int}} = -\boldsymbol{\mu} \cdot \mathbf{B} = -g\mu_b S_z B_z. \quad (2.6)$$

Here, g is the gyromagnetic ratio of the silver atom, μ_b is the Bohr magneton, and S_z is the spin moment of the unpaired electron, which can take values of $\pm 1/2$. The force in the z-direction is given by

$$F_z = \frac{\partial U}{\partial z} = g\mu_b S_z \frac{\partial B_z}{\partial z} = \pm \frac{1}{2} g\mu_b \frac{\partial B_z}{\partial z} \quad (2.7)$$

As the ion beam travels through the inhomogeneous magnetic field, the $|\uparrow\rangle$ and $|\downarrow\rangle$ components are deflected in opposite directions. In effect, the presence of the magnetic field *entangles* the spin degree of freedom with the positional degrees of freedom (we will discuss entanglement more in Chapter 3). The state of the system can now be represented as

$$\rho = \frac{1}{2} \left[\begin{pmatrix} 1 & 0 \\ 0 & 0 \end{pmatrix} \otimes |-\bar{z}\rangle\langle -\bar{z}| + \begin{pmatrix} 0 & 0 \\ 0 & 1 \end{pmatrix} \otimes |+\bar{z}\rangle\langle +\bar{z}| \right], \quad (2.8)$$

where $|\pm\bar{z}\rangle$ corresponds to the position of the upward (+) and downward (-) deflected beams.

After exiting the magnetic field, the Ag atoms impinge on a detector screen, which makes a projective measurement of the position. If the ion beams corresponding to $|\uparrow\rangle$ and $|\downarrow\rangle$ are sufficiently well-separated, the screen simultaneously makes a projective measurement of the spin degrees of freedom. Thus, we see that the positional degree of freedom acts as an *ancilla*: it is a macroscopically-measurable quantity that can be used to infer the state of a quantum degree of freedom. If we were to move the screen such that it blocked the lower beam and allowed the upper beam alone to propagate, a second Stern-Gerlach measurement of the spin moment would show the resultant propagating beam to be fully polarized, having been projected into the $|\downarrow\rangle$ spin state.

Suppose instead we were to start in a pure quantum state polarized along σ^X , such that $|\psi_{\text{spin}}\rangle = \frac{|\uparrow\rangle+|\downarrow\rangle}{\sqrt{2}}$ or

$$\rho_{\text{spin}} = \frac{1}{2} \begin{pmatrix} 1 & 1 \\ 1 & 1 \end{pmatrix} \quad (2.9)$$

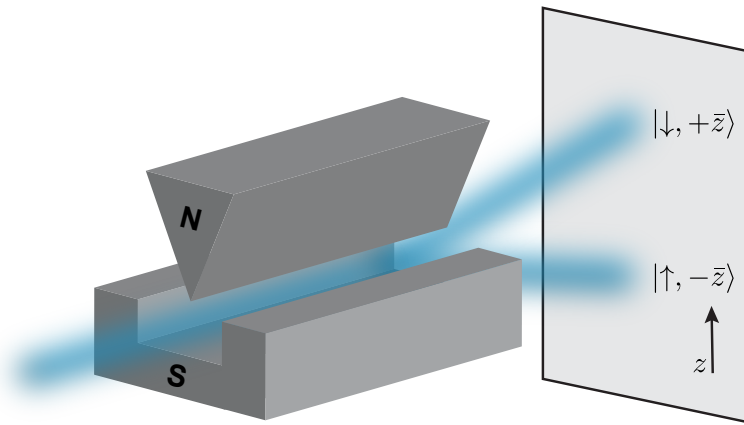


Figure 2.1: The Stern-Gerlach experiment. A beam of unpolarized Ag atoms passes through an inhomogeneous magnetic field, and emerges as two spatially-separated, spin-polarized beams. The position of the atoms is recorded at a detector screen, where the position of the atom is used to infer its spin.

with $\langle \sigma^x \rangle = +1$. At the end of the measurement, the spins will be fully polarized into $\sigma^z = \pm 1$, but the coherent phase relationship between $|\uparrow\rangle$ and $|\downarrow\rangle$ has now been destroyed: $\langle \sigma^x \rangle = 0$. This is what we mean by “measurement destroys coherence”: by measuring a quantum system via a given operator, we scramble information contained in a non-commuting observable.

2.1.3 The Stern-Gerlach Experiment: Weak Measurement Regime

So far, we have neglected the intrinsic uncertainty in the z -component of the individual atoms in the atom beam. In fact, the atoms propagate in a Gaussian beam with standard deviation σ . In the limit where the separation between the centers of the $|\pm\bar{z}\rangle$ beams is much larger than σ , we can safely ignore the uncertainty in z (Figure 2.2b): the wavepackets are very well-separated, and one can draw a line of discrimination that well-separates the two spin-polarized beams. We refer to this regime as the *projective* measurement regime, as the measurement has effectively projected the system into two fully spin-polarized sub-ensembles. However, if the magnetic field gradient is weak or the propagation length short (Figure 2.2a), there is no good discrimination line; any such line of discrimination will inevitably lead to many post-selection errors. We refer to this as a *weak*, or *non-projective* measurement. It is also sometimes described as a partial measurement.

It is important to note that these post-selection errors do not mean that the measurement

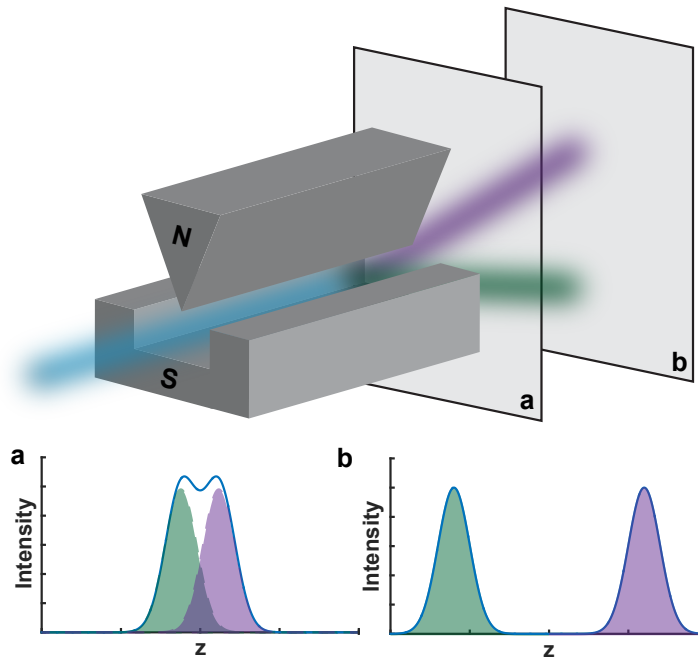


Figure 2.2: The Stern-Gerlach experiment in the weak- (a) and strong- (b) measurement regimes. Here, we show the measurement profile of an un-polarized input beam (blue) as a line, and the expected profile of a polarized $|\uparrow\rangle$ (green) and $|\downarrow\rangle$ (purple) state as a shaded object. By varying the propagation length, the separation between the spin-polarized beams can be varied continuously. In the strong-measurement regime (b), the ensembles are well-separated, and we can effectively post-select a spin-polarized ensemble. In the weak-measurement regime (a), the separation is on the order of the intrinsic beam width; a post-selected ensemble will not be fully projected into either spin polarization.

is *bad*: a bad measurement would be one in which a quantum observer, one with access to all of the fluctuations in the system, would have been able to do an accurate post-selection, but our measurement apparatus is too noisy to accomplish the same feat. In a *weak* measurement, there is no quantum or classical observer that is able to do an accurate post-selection, because there is insufficient quantum information to do so. This means that the system has been perturbed, but not projected, by the measurement. In a bad measurement, the system has been projected by the measurement, but the experimenter is not able to determine into which state it has been projected.

To understand weak measurement in the context of the Stern-Gerlach experiment, suppose we were to cut a small hole in the detector screen at position $z = 0$, such that the fraction of the beam that is undeflected is allowed to propagate. A second Stern-Gerlach

device operating in the projective regime would measure this beam to have $\langle \hat{\sigma}^z \rangle = 0$, just as the original beam was. This is because the Gaussian amplitude for both the $|\pm z\rangle$ beams is equal at this point. Although the beam has passed through a measurement device, it has not projected onto an eigenstate of the measurement. If we instead cut a small hole at $z = +\epsilon$, a second projective Stern-Gerlach device will find that the propagating beam is slightly polarized in the $|\downarrow\rangle$ direction, but still contains significant amplitude in the $|\uparrow\rangle$ state.

Rather than implementing a projection operator, the Stern-Gerlach device in the weak measurement case implements an operation known as a *positive operator-valued measurement* (POVM), which we will label $\Omega(z)$. POVMs are a *non-orthogonal* set of operators that span the Hilbert space of the measurement, but are generally made of linear combinations of the traditional projection operators. In the particular case of the Stern-Gerlach experiment, the POVMs are given by

$$\Omega(z) = f(z, +\bar{z}, \sigma) \Pi_{\downarrow} + f(z, -\bar{z}, \sigma) \Pi_{\uparrow}; \quad (2.10a)$$

$$f(z, \bar{z}, \sigma) = \frac{1}{\sigma \sqrt{2\pi}} e^{\frac{(z-\bar{z})^2}{2\sigma^2}}. \quad (2.10b)$$

In other words, the extent to which the measurement projects onto $|\uparrow\rangle$ or $|\downarrow\rangle$ becomes a continuous function of position, and the measurement in general projects into a combination of both eigenstates of the measurement operator.

The Stern-Gerlach experiment begins with an incoherent (mixed) starting state, so the weak measurement described here will itself only allow postselection mixed states with varying proportions of the two spin polarizations. However, we could just as easily have begun our experiment with an ensemble of atoms all in the coherent superposition state $|\psi_i\rangle = \frac{|\uparrow\rangle + |\downarrow\rangle}{\sqrt{2}}$

or $\rho_{\text{spin}} = \frac{1}{2} \begin{pmatrix} 1 & 1 \\ 1 & 1 \end{pmatrix}$, which has the same net-zero spin polarization but is a pure state. In this case, we can see that the POVM actually preserves the purity of the state, as measured by $\text{Tr}\{\rho^2\}$. This is an surprising result, as we are accustomed to considering measurement a process that decoheres a quantum superposition into a classical mixture of measurement eigenstates. However, here we see that performing a POVM and accurately recording its outcome z allows us to precisely predict the back-action of the measurement “kick” on the quantum system, thus ensuring no information about the quantum state is lost. The POVM formalism, along with the continuous, stochastic state tracking that it implies, suggests the need for an alternative method of conceptualizing the measurement process. Two such useful methods, the quantum Bayesian formalism (QB) and the stochastic master equation (SME), will be reviewed in the next sections.

Note that thus far we have considered an atom beam comprised of many individual atoms, providing to a probability distribution in z as the atoms hit the detection screen. We also will be interested, however, in exploring the effect of the measurement on a single atom within that ensemble. Additionally, the Stern-Gerlach experiment performs a destructive measurement, in that once an atom hits the detector screen, no further measurements of

its state can be made. We will be interested in measurements that are both *weak* and *continuous*, allowing for multiple sequential measurement of the same quantum state that allow us to track an individual quantum trajectory.

2.2 The Quantum Bayesian Formalism

The quantum Bayesian (QB) formalism [69–73] is a straightforward extension of classical Bayesian conditional probabilities to a coherent quantum system. The QB formalism takes a personalist view of the state vector and the density matrix: it posits that the density matrix represents the current state of the observer’s knowledge about the state of the quantum system under study, but makes no claims of objective realism.

The classical Bayes rule describes the conditional probability of event A , given the occurrence of event B :

$$P(A|B) = \frac{P(A)P(B|A)}{P(B)}. \quad (2.11)$$

This rule states that a prior assessment of the probability of event A - that is, $P(A)$ - must be updated by the probability of B given A , normalized by the prior probability of B . Since the diagonal elements of a density matrix similarly represent the probability that the quantum system is in the given state, we can guess a similar rule for a quantum system. Let’s specialize to a single two-level system, whose density matrix is given by

$$\rho = \begin{pmatrix} \rho_{g,g} & \rho_{g,e} \\ \rho_{e,g} & \rho_{e,e} \end{pmatrix}, \quad (2.12)$$

where g and e represent the ground and excited states of the two-level system. Let’s suppose we know the measurement probability distributions $p_{\pm}(V)$, where V is a generalized measurement outcome. In the Stern-Gerlach experiment, for example, we would replace V with z , and $p_{\pm}(V)$ with Eq. (2.10b). We can then write an equivalent *quantum* Bayes rule for the diagonal terms:

$$(\rho_{g,g}|V) = \frac{\rho_{g,g}p_+(V)}{p_+(V) + p_-(V)} \quad ; \quad (\rho_{e,e}|V) = \frac{\rho_{e,e}p_-(V)}{p_+(V) + p_-(V)}. \quad (2.13)$$

Here, we update the diagonal density matrix elements based on the measurement result, and our prior knowledge of the probability of that result assuming that the system was in the respective eigenstates. If the measurement being performed is nondestructive and continuous, one can use the output of one Bayesian update step as the input to the next, resulting in a *trajectory* of updates due to the full measurement record $\mathbf{V} = \{V_1, V_2, \dots, V_N\}$. In the special case that the noise giving rise to the measurement distributions is colorless and memoryless - the Markov approximation - one can equivalently average the measurement record and perform an update based on the integrated measurement.

The diagonal density matrix elements are in some sense trivial to predict via probability rules, since they represent classical probabilities of finding the system in their respective states. The off-diagonal elements, which contain information about the phase coherence and thus the purity of a superposition state, have a less obvious equivalent to the Bayes rule. However, here as well we can be equally observationalist in our approach. The Bayes rule for the off-diagonal elements becomes

$$(\rho_{g,e}|V) = (\rho_{e,g}^*|V) = \rho_{g,e} \sqrt{\frac{(\rho_{g,g}|V)(\rho_{e,e}|V)}{\rho_{g,g}\rho_{e,e}}} e^{-\gamma t} \quad (2.14)$$

where γ is a damping term which goes to zero for a perfectly efficient measurement system and for a quantum system with infinite lifetime [69]. We will see in Section 2.4 how to handle the effects of inefficient measurement. Eq. (2.14) states that, in the absence of additional unitary dynamics, the off-diagonal density matrix elements can be determined simply by updating the diagonal density matrix elements. It is also possible to include deterministic evolution at rate ω into the Bayesian formalism [74], as long as we perform a Bayesian update in timesteps $\tau \ll 1/\omega$. This formalism generalizes naturally to a higher-dimensional Hilbert space according to

$$\begin{aligned} (\rho_{i,i}|V) &= \frac{\rho_{i,i}p_i(V)}{\sum_j p_j(V)} \\ (\rho_{i,j}|V) &= \rho_{i,j} \sqrt{\frac{(\rho_{i,i}|V)(\rho_{j,j}|V)}{\rho_{i,i}\rho_{j,j}}} e^{-\gamma_{ij}t} \end{aligned} \quad (2.15)$$

where i and j are eigenstates of the Hamiltonian and γ_{ij} is a generalized decoherence rate between states i and j . Eq. (2.15) reduces to the general statement, applicable to both on- and off-diagonal elements

$$(\rho_{i,j}|V) = \frac{\rho_{i,j}}{\sum_k p_k(V)} \sqrt{p_i(V)p_j(V)} e^{-i\gamma_{ij}t}. \quad (2.16)$$

We will derive a Bayesian update rule for a half-parity entangling measurement in Chapter 5, where we will see its power in understanding and interpreting a noisy measurement signal.

Everything that we have developed in this section has been perfectly empirical - we have assumed knowledge of an arbitrary measurement distribution (conditioned on the eigenstates), and also have assumed knowledge of the starting state of the system. The physics, of course, comes in predicting these distributions, based on a quantitative understanding of the measurement processes being utilized, and the quantum noise that is associated with them. In Chapter 4, we will present the dispersive measurement of a superconducting quantum bit embedded in a resonator, in order to provide a concrete example of this process.

The chief advantage of the QB approach is its mathematical and conceptual simplicity. One must only know an estimated starting state, and an expected distribution of measurement outcomes given the eigenstates of the system, in order to update the (diagonal)

density matrix elements based on the measurement outcome. From a philosophical standpoint, however, it requires a major concession: we cede any notion that the density matrix represents the true state of the system, or of an ensemble of identically prepared systems, instead stipulating that it is specific to the observer, and that another observer with more or less information might construct a different density matrix to which the quantum Bayesian update can just as reasonably be applied.

2.3 The Stochastic Master Equation

The stochastic master equation is a powerful, minimal, and general formalism for understanding and interpreting the effects of the interaction between a quantum system of interest and a fluctuating degree of freedom (*i.e.* quantum noise). There are many resources [9, 75–78] for deriving and understanding SMEs, but here we will closely follow a wonderful introduction from Jacobs and Steck [79]. Our goal is to gain intuition for the relationship between quantum fluctuations and measurement outcomes; for how to infer a quantum trajectory from a continuous measurement record; and for how to account for an inefficient measurement process. Along the way, we will see that dissipation - broadly, any process that reduces the purity of a quantum system - is intimately related to the measurement process, and we will learn to quantify that relationship. In this section we will derive the SME completely generally; later, we will see its connection to physical measurement processes.

We first consider the unitary evolution of the quantum state, beginning with the Schroedinger equation:

$$i\hbar \frac{\partial}{\partial t} |\psi\rangle = \hat{H} |\psi\rangle \quad (2.17)$$

Written in differential form and considering a short time interval, we have

$$d|\psi\rangle = \left(-\frac{i}{\hbar} \hat{H} dt \right) |\psi\rangle \quad (2.18)$$

If we make the approximation that the system evolves slowly (the Born approximation), the evolution of a pure state vector in the time interval is given by

$$|\psi'\rangle = |\psi\rangle + d|\psi\rangle = \left(1 - \frac{i}{\hbar} \hat{H} dt \right) |\psi\rangle \quad (2.19)$$

A similar transformation will apply to the density matrix:

$$\rho' = \rho + d\rho = \left(1 - \frac{i}{\hbar} \hat{H} dt \right) \rho \left(1 + \frac{i}{\hbar} \hat{H} dt \right) = \rho - \frac{i}{\hbar} [\hat{H}, \rho] dt. \quad (2.20)$$

This defines the instantaneous evolution of the density matrix under a unitary Hamiltonian, and is the Schroedinger equation for density matrices.

2.3.1 Dissipation via Fluctuation: Lindblad Operators

Eq. (2.20) completely describes the instantaneous evolution of a density matrix for which all dynamics are described by a unitary Hamiltonian, and represents a completely positive transformation of the form $\rho \rightarrow \hat{\mathcal{A}}\rho\hat{\mathcal{A}}^\dagger$, where $\hat{\mathcal{A}} = 1 - \frac{i}{\hbar}\hat{H}dt$. However, as noted in Section 2.1, we often must account for the interaction between a system of interest and a fluctuating degree of freedom. Therefore, let us add two terms - completely generally - to our transformation:

$$\hat{\mathcal{A}} = 1 - \frac{i}{\hbar}\hat{H}dt + \hat{b}dt + \hat{c}dW \quad (2.21)$$

Here, we have an additional deterministic evolution operator \hat{b} , which we assume to be Hermitian, and a *stochastic* evolution term \hat{c} that grows with dW , which represents a Wiener process. A Wiener process is equivalent to a classical random walk centered at the origin. Random walks can be represented by a normal distribution whose width scales with \sqrt{t} , such that the probability density is given by

$$P(W, t) = \frac{1}{\sqrt{2\pi t}}e^{-W^2/2t}. \quad (2.22)$$

Thus, we can consider the additional term in our evolution operator

$$d\hat{y} = \hat{b}dt + \hat{c}dW \quad (2.23)$$

to be the equivalent of a *drifting* random walk operator where the increment dW is the “step” taken in time increment dt . In the quantum context, the “walker” can be any fluctuating quantity, such as position and momentum, electromagnetic field quadrature amplitudes, or other zero-point fluctuating modes. Just as $P(W, t)$ represents a Gaussian distribution, dW is itself a normally-distributed random variable with a distribution width of \sqrt{dt} . The Wiener process is a *white-noise* process, such that $dW(t)$ is statistically independent of $dW(t')$ for all $t \neq t'$.

There are a number of useful properties of Wiener processes which we will cite here but will not prove [80]:

$$\langle\langle dW \rangle\rangle = 0 \quad (2.24a)$$

$$dW^2 = dt \quad (2.24b)$$

$$\langle\langle \hat{y} dW \rangle\rangle = \langle\langle dW \rangle\rangle = 0 \quad (2.24c)$$

Here, we define the *ensemble average* $\langle\langle \rangle\rangle$ as the mean over all possible Wiener processes. Eq. (2.24a) simply reflects that the random variable has zero mean; Eq. (2.24b) is a formulation of the Itô Rule that is the foundation of stochastic calculus; and Eq. (2.24c) states that the expectation value of \hat{y} is statistically independent from $\langle\langle dW \rangle\rangle$.

With this context for the Wiener process, we substitute (2.21) into (2.20) and keep terms only up to first-order in dt (that is, we throw out terms proportional to $dW dt$ and dt^2 , and use Eq. (2.24b) to substitute $dW^2 = dt$), and find

$$d\rho = -\frac{i}{\hbar} [\hat{H}, \rho] dt + \left\{ \hat{b}, \rho \right\} dt + \hat{c}\rho\hat{c}^\dagger dt + (\hat{c}\rho + \rho\hat{c}^\dagger) dW, \quad (2.25)$$

where $\{A, B\}$ is the anticommutator $AB + BA$.

We now are interested in the ensemble average of all possible Wiener processes in this system. Using Eq. (2.24c) to set $\langle\langle (\hat{c}\rho + \rho\hat{c}^\dagger) dW \rangle\rangle = 0$, we have

$$d\langle\langle \rho \rangle\rangle = -\frac{i}{\hbar} [\hat{H}, \langle\langle \rho \rangle\rangle] dt + \left\{ \hat{b}, \langle\langle \rho \rangle\rangle \right\} dt + \hat{c}\langle\langle \rho \rangle\rangle \hat{c}^\dagger dt. \quad (2.26)$$

Note that Eq. (2.26) represents an average over all possible realizations of a the density matrix under the stochastic evolution process we are studying, and therefore $\langle\langle \rho \rangle\rangle$ itself is a density matrix. Specifically, it must maintain unit trace over all realizations, such that $d\text{Tr}[\langle\langle \rho \rangle\rangle] = \text{Tr}[d\langle\langle \rho \rangle\rangle] = 0$. We have defined \hat{H} to be a unitary operation, so we know this condition holds for the first term. For the terms containing \hat{b} and \hat{c} , we use the cyclic property of the trace to find

$$\text{Tr}[\hat{b}\langle\langle \rho \rangle\rangle + \langle\langle \rho \rangle\rangle \hat{b} + \hat{c}\langle\langle \rho \rangle\rangle \hat{c}^\dagger] = \text{Tr}[(2\hat{b} + \hat{c}^\dagger\hat{c}) \langle\langle \rho \rangle\rangle] = 0. \quad (2.27)$$

In order for Eq. (2.27) to hold for arbitrary density matrix, this provides a restriction on \hat{b} and \hat{c} :

$$\hat{b} = -\frac{\hat{c}^\dagger\hat{c}}{2}. \quad (2.28)$$

We can use this relationship to define [81] the *Lindblad superoperator* $\mathcal{D}[\hat{c}] \rho$

$$\mathcal{D}[\hat{c}] \rho \equiv \hat{c}\rho\hat{c}^\dagger - \frac{1}{2} (\hat{c}^\dagger\hat{c}\rho + \rho\hat{c}^\dagger\hat{c}), \quad (2.29)$$

which we can use to rewrite Eq. (2.26):

$$d\langle\langle \rho \rangle\rangle = \left(-\frac{i}{\hbar} [\hat{H}, \langle\langle \rho \rangle\rangle] + \mathcal{D}[\hat{c}] \langle\langle \rho \rangle\rangle \right) dt. \quad (2.30)$$

This is in fact the unconditioned master equation for ensemble evolution in the presence of a noisy process. Note that the evolution of the ensemble of fluctuation realizations is purely deterministic (proportional to dt), and that while we have required that $\text{Tr}[\langle\langle \rho \rangle\rangle] = 1$, we have made no such requirement of $\text{Tr}[\langle\langle \rho \rangle\rangle^2]$. In fact, a Lindblad term is almost always associated with a reduction in the square trace of the ensemble density matrix. This represents a reduction in the purity of the density matrix, as it becomes an average over a noisy ensemble. Lindblad superoperators are often referred to as *Lindblad dissipators* for

this reason. Also note that one can trivially multiply \hat{c} by a constant to increase or decrease the rate at which the dissipation occurs; we will examine the effects of the measurement rate in Section 2.4.

For example, suppose we neglect the unitary dynamics (i.e. set $\hat{H} = 0$) and apply a Lindblad operator with $\hat{c} = \hat{\sigma}^Z \sqrt{\gamma_\phi/2}$. Dropping the ensemble average notation, we then see that the density matrix evolution is given by

$$\begin{aligned} d\rho &= \left[\frac{\gamma_\phi}{2} \hat{\sigma}^Z \rho \hat{\sigma}^Z - \frac{\gamma_\phi}{4} ((\hat{\sigma}^Z)^2 \rho + \rho (\hat{\sigma}^Z)^2) \right] dt \\ &= \frac{\gamma_\phi}{2} [\hat{\sigma}^Z \rho \hat{\sigma}^Z - \rho] dt \\ &= \gamma_\phi \begin{pmatrix} 0 & -\rho_{g,e} \\ -\rho_{e,g} & 0 \end{pmatrix} dt \end{aligned} \quad (2.31)$$

Integrating, we find

$$\rho(t) = \begin{pmatrix} \rho_{g,g} & \rho_{g,e} e^{-\gamma_\phi t} \\ \rho_{e,g} e^{-\gamma_\phi t} & \rho_{e,e} \end{pmatrix} \quad (2.32)$$

The diagonal density matrix elements remain constant, but the off-diagonal terms decay to zero. If we were to begin in a pure x-polarized state, it would decay under the back-action of a $\hat{\sigma}^Z$ dissipation into an incoherent mixture of $|g\rangle$ and $|e\rangle$, with $\text{Tr}[\rho^2(t \rightarrow \infty)] = 1/2$. Thus, a Lindblad operator with $\hat{c} \propto \hat{\sigma}^Z$ represents dephasing.

2.3.2 Measurement in the SME formalism

We now return to the un-averaged form of the master equation, which in light of Eq. (2.28) we can write as:

$$d\rho = -\frac{i}{\hbar} [\hat{H}, \rho] dt + \mathcal{D}[c] \rho dt + (\hat{c}\rho + \rho\hat{c}^\dagger) dW. \quad (2.33)$$

The first two terms, as we have determined, are trace-preserving; however, because \hat{c} is still arbitrary, the final term does not in general preserve the trace. In order to allow \hat{c} to remain an arbitrary operator, we will renormalize ρ by the term

$$-\text{Tr}[(\hat{c}\rho + \rho\hat{c}^\dagger) dW] = -\text{Tr}[\rho(\hat{c} + \hat{c}^\dagger)] dW = -\langle \hat{c} + \hat{c}^\dagger \rangle dW. \quad (2.34)$$

We define the measurement superoperator $\mathcal{H}[\hat{c}] \rho$:

$$\mathcal{H}[\hat{c}] \rho \equiv \hat{c}\rho + \rho\hat{c}^\dagger - \langle \hat{c} + \hat{c}^\dagger \rangle \rho \quad (2.35)$$

and rewrite the nonlinear master equation as

$$d\rho = -\frac{i}{\hbar} [\hat{H}, \rho] dt + \mathcal{D}[\hat{c}] \rho dt + \mathcal{H}[\hat{c}] \rho dW \quad (2.36)$$

In the case \hat{c} is a Hermitian operator (as is required for any observable), Eq. (2.36) is the stochastic master equation (SME) describing the evolution of the density matrix under a

single “trajectory” of randomly-sampled steps dW , representing fluctuations in the expectation value of the observable \hat{c} . More intuitively, $\mathcal{H}[\hat{c}]\rho$ represents the stochastic back-action of the measurement on the state of the quantum system. Critically, this back-action is proportional to dW , so if we know the measurement operator that is being applied and have a means to collect information about the quantum fluctuations, we can update our density matrix to follow the state evolution, thus effectively “undoing” the dissipation caused by the $\mathcal{D}[\hat{c}]\rho$ term.

Note that though we are using the language of density matrices here, the SME formalism derived here does *not* represent an ensemble of realizations; rather, it allows us to derive the stochastic evolution of a single instantiation of the quantum system of interest, and a single noise record. In principle, if we have full access to the measurement record, it is possible to continually update the density matrix in a way that preserves not just trace-normalization, but also the *purity* of the quantum state, thus turning a dissipative process into a coherent process.

2.4 Measurement Rate and Inefficient Measurements

In any physically realizable system, we cannot hope to have a perfect collection of the measurement record. Whether due to photon scattering, resistive losses, or external noise sources, the measurement record we collect with macroscopic, room-temperature, classical equipment will inevitably be corrupted to some degree, even using the most state-of-the-art detectors. We therefore must consider the effect of measurement efficiency on our ability to accurately track the evolution of the density matrix.

First, we would like to draw a more physical connection between the distribution of measurement outcomes and the strength of the measurement back-action. To do so, we will return to a more physically-motivated derivation of the SME formalism. Recall that the partial measurement performed by a weak Stern-Gerlach apparatus can be written per Eq. (2.10b) as a sum of Gaussian-weighted POVM partial projectors. For a general two-level system in which we measure $\hat{\sigma}^Z$ by tracking a variable z , we can write

$$\Omega(z) = \frac{1}{\mathcal{N}} \left(|g\rangle\langle g| e^{-\frac{1}{2}(\frac{z-z_g}{\sigma})^2} + |e\rangle\langle e| e^{-\frac{1}{2}(\frac{z-z_e}{\sigma})^2} \right) \quad (2.37)$$

where \mathcal{N} is a normalization and z_i is the centroid of the Gaussian distribution for state $|i\rangle$. Since we have restricted our measurement to the Markovian approximation, we expect the variance of the distributions to decrease as $1/t$. Let us therefore define $\sigma^2 = 1/2\Gamma\Delta t$, for reasons that will soon become apparent. We then have

$$\Omega(z) = \frac{1}{\mathcal{N}} \left(|g\rangle\langle g| e^{-\Gamma\Delta t(z-z_g)^2} + |e\rangle\langle e| e^{-\Gamma\Delta t(z-z_e)^2} \right). \quad (2.38)$$

The probability of measurement outcome z is given by

$$P(z) = \text{Tr}[\Omega(z)\rho\Omega^\dagger(z)] = P(g)e^{-2\Gamma\Delta t(z-z_g)^2} + P(e)e^{-2\Gamma\Delta t(z-z_e)^2} \quad (2.39)$$

In the limit where $\Delta t \ll 1/\Gamma$ such that $\sigma \gg |z_g - z_e|$, we can approximate $P(z)$ as a single Gaussian, centered at $z = \langle \hat{\sigma}^Z \rangle$:

$$P(z) \approx \frac{1}{\mathcal{N}} e^{-2\Gamma\Delta t(z - \langle \hat{\sigma}^Z \rangle)^2} \quad (2.40)$$

Alternatively, we can write z as a stochastic variable given by

$$z = \langle \hat{\sigma}^Z \rangle + \frac{\Delta W}{\sqrt{4\Gamma\Delta t}}, \quad (2.41)$$

where W as usual is a zero-mean Wiener variable. Substitution into Eq. (2.40) gives $P(z)$ as a normally distributed stochastic variable with variance Δt , as desired. Thus we can see that Γ defines a measurement “strength” or measurement rate. Sending $\Delta W, \Delta t \rightarrow dW, dt$ and generalizing back to an arbitrary measurement operator, we can define the measurement record according to a series of increments

$$dz = \langle \hat{c} \rangle dt + \frac{dW}{\sqrt{4\Gamma}}, \quad (2.42)$$

Thus, we see that the measurement output z evolves with a deterministic component, which is proportional to the true expectation value of the measurement operator, and a stochastic component, whose magnitude is scaled by Γ . In the limit where Γ is very small, the measurement record is dominated by noise and the expectation value is washed out by fluctuations, such that the measurement occurs slowly; when Γ is large, the measurement quickly resolves to the true eigenvalue of the measured operator. By following a procedure similar to Section 2.3, we can derive the master equation with a measurement strength built in organically:

$$d\rho = \Gamma \mathcal{D}[\hat{c}] \rho dt + \sqrt{\Gamma} \mathcal{H}[\hat{c}] \rho dW. \quad (2.43)$$

The details of this derivation can be found in Ref. [79]; however, note that in that text one must make the substitution $\Gamma = 2k$. Thus, we see that the measurement rate enters linearly into the dissipation term, and as a square root into the measurement update operator. In general, Γ is set by the signal-to-noise ratio of the ancilla that is used to measure the system: the better separated the histograms become in unit time, the stronger the measurement back-action.

Now that we have understood how to translate from a quantum noise distribution to the SME formalism, we can consider the effects of inefficient collection. This derivation is again adapted from Ref. [79]. Suppose the system now has two observers, Alice and Eve (the latter of whom represents the environment). Alice measures observable \hat{a} at rate Γ_1 , and Eve measures the same observable at rate Γ_2 . Alice’s knowledge of the state of the system is denoted by ρ_1 , and Eve’s by ρ_2 . From the perspective of Alice, the measurement made by Eve is lost information, so Γ_2 enters into her master equation as a pure dissipation term. The opposite is true for Eve. Thus, the SMEs for the two systems are given by

$$d\rho_1 = \Gamma_1 \mathcal{D}[\hat{a}] \rho_1 + \Gamma_2 \mathcal{D}[\hat{a}] \rho_1 + \sqrt{\Gamma_1} \mathcal{H}[\hat{a}] \rho_1 \quad (2.44)$$

$$d\rho_2 = \Gamma_1 \mathcal{D}[\hat{a}] \rho_2 + \Gamma_2 \mathcal{D}[\hat{a}] \rho_2 + \sqrt{\Gamma_2} \mathcal{H}[\hat{a}] \rho_2 \quad (2.45)$$

The measurement signals at the two ports are given by

$$dy_1 = \langle \hat{a} \rangle_1 dt + \frac{dW_1}{\sqrt{4\Gamma_1}} \quad (2.46)$$

$$dy_2 = \langle \hat{a} \rangle_2 dt + \frac{dW_2}{\sqrt{4\Gamma_2}} \quad (2.47)$$

where the notation $\langle \hat{a} \rangle_i$ denotes the expectation value from the standpoint of ρ_i , and because the measurement/dissipation rates are different on the two channels we do not in general expect $\langle \hat{a} \rangle_1 = \langle \hat{a} \rangle_2$. Notice also that dW_1 and dW_2 are independent noise sources - we expect the fluctuations observed by Alice and Eve to be uncorrelated.

Now let $\Gamma = \Gamma_1 + \Gamma_2$ and $\eta = \Gamma_1/\Gamma$. We can then rewrite Alice's SME according to

$$\begin{aligned} d\rho_1 &= \Gamma \mathcal{D}[\hat{a}] \rho_1 + \sqrt{\Gamma\eta} \mathcal{H}[\hat{a}] \rho_1 \\ dy_1 &= \langle \hat{a} \rangle_1 dt + \frac{dW}{\sqrt{4\Gamma\eta}} \end{aligned} \quad (2.48)$$

The dissipation rate is governed, as we expect, by the total leakage rate of information from the system; however, the back-action and the effective measurement rate are scaled by a factor of η . Since $\eta < 1$ by definition, this means that if the system begins in an initial superposition state, the purity of ρ_1 will in general decrease under the influence of the measurement. For example, if we measure $\hat{\sigma}^Z$ at rate Γ with efficiency η , the off-diagonal elements $\rho_{e,g}, \rho_{g,e}$ will decay at an additional rate $\Gamma(1 - \eta)$, leading to an overall dephasing effect that is mitigated, but not completely undone, by the state update protocol. Only when the quantum efficiency is unity and all fluctuations captured by the observer can the square-trace purity of the density matrix after measurement match the purity before measurement.

2.5 Summary of Measurement and Dissipation

In this chapter, we have developed a sophisticated understanding of quantum measurements, dissipation, and the connections between the two. In Section 2.1, we saw the difference between strong (fully projective) and weak (partially projective) measurement, and introduced the POVM formalism that describes a partial measurement. In Section 2.2, the quantum Bayesian formalism was developed, and we saw its strength as a mathematically-straightforward, fully empirical approach to continuous measurement. In Section 2.3, we derived a more mathematically rigorous approach to continuous measurement via the stochastic master equation, which captures both the dissipative effects of measurement and the ability to “undo” that dissipation by performing a state update conditioned on the measurement outcome. Finally, in Section 2.4 we explored the connection between the physical measurement distributions and the measurement rate, which allowed us to understand the effects of inefficient measurement on the quantum state update. These concepts will be critical for understanding the experiments and developments presented throughout this dissertation.

Chapter 3

Entanglement: A Primer

If two separated bodies, about which, individually, we have maximal knowledge, come into a situation in which they influence one another and then again separate themselves, then there regularly arises that which I just called *entanglement [Verschränkung]* of our knowledge of the two bodies. At the outset, the joint catalogue of expectations consists of a logical sum of the individual catalogues; during the process the joint catalogue develops necessarily according to the known law.... Our knowledge remains maximal, but at the end, if the bodies have again separated themselves, that knowledge does not again decompose into a logical sum of knowledge of the individual bodies.

Erwin Schrödinger, *Die gegenwärtige Situation in der Quantenmechanik*, 1935

Entanglement, a special class of quantum superposition, is perhaps the strangest and most defining aspect of quantum mechanics. Strange, because the idea of an action on one quantum system instantaneously affecting a second, isolated system runs counter to all classical intuition; most defining, because the ability to generate entanglement allows us to directly test predictions of quantum mechanics that are in conflict with concepts of locality. Since generating and characterizing entanglement will be at the heart of this dissertation, we present here a brief summary of entanglement, specifically: what it is and is not; how it is generated; and how it is quantified. We will pay special attention to measures of *bipartite* entanglement, or entanglement between two quantum objects. Our goal here is not to make a comprehensive review of the history of entanglement, but rather to provide context and background for the remainder of the dissertation.

3.1 Introduction to Entanglement

Suppose a linearly-polarized photon of frequency 2ω is spontaneously converted into two photons of frequency ω . Conservation of angular momentum require that the photons are comprised of one horizontally (H-) polarized and one vertically (V-) polarized photon. However, because they are indistinguishable photons, the photons (labeled A and B) are in fact converted into a superposition state given by

$$|\psi\rangle = \frac{|H\rangle_A|V\rangle_B + |V\rangle_A|H\rangle_B}{\sqrt{2}} \quad (3.1)$$

This process, known as parametric down-conversion, is precisely the process used to produce some of the first experimental entangled pairs to convincingly violate Bell's inequality [82–84].

Let us recall the basic physics of such entangled Bell pairs. If we create many such entangled pairs, but only interrogate the state of photon A , we will find that it has a 50% chance of being in state $|H\rangle$ and 50% chance of being in state $|V\rangle$, but we cannot predict into which state it is projected for each photon. This is the equivalent of reaching into a bag of blue and red balls and choosing one at random – a perfectly classical probability problem. If we were to measure the system along a perpendicular axis — say, along the linear combination $\hat{\epsilon} = (\hat{x} + \hat{y})/\sqrt{2}$ — we would similarly find the expectation value to be zero. No coherent information is contained along any single-qubit measurement axis. The same holds for photon B . It is only by examining the two photon states *together* that we see that the state of the system is in fact highly correlated: each time system A is found to be in state $|V\rangle$, system B will be found in state $|H\rangle$ (and vice versa). In addition, there are also perfect correlations for simultaneous measurements along $\hat{\epsilon}$: this state contains higher correlations than a pair of blue and red balls that are arbitrarily given to A and B .

These correlations in theory exist even if the photons are space-like separated and measured in an interval brief enough that the event cones do not intersect, such that there is insufficient time for one system to “signal” to the other, at sub-light speeds, what the outcome of its measurement was. Entanglement is thus considered to violate local realism and classical notions of causality [85–87]. Although there are a number of challenging experimental loopholes that must be closed in order definitively demonstrate nonlocal correlations in excess of what is classically possible, several recent experiments report to have done just that [88–90].

The high levels of correlation inherent in entangled states make them attractive for a number of purposes. Entanglement has inspired the concept of a universal quantum information processor that could efficiently factor large numbers [91] and perform efficient searches [92]. Such a processor must generate entanglement across an array of hundreds, or perhaps thousands, of individually addressable quantum systems. In addition, quantum cryptography protocols rely on the distribution and correlated measurement of entangled pairs across a secure network [93–95]. Recently, there has been growing interest in developing specialty quantum processors that, although not capable of universal computation, are

nevertheless able to surpass classical devices in the simulation of high-dimensional problems in chemistry and physics [96–99]; these processors again harness the power of entanglement to handle matrices that stretch the capabilities of supercomputers. More fundamentally, entanglement itself is a subject of intrinsic interest - putting aside any technological applications of entanglement, physicists are interested in generating, manipulating, and studying entangled states of matter.

3.2 Defining Entanglement

Given its importance to the enterprise of quantum mechanics, entanglement is surprisingly difficult to define. The clearest definition comes as a negative - that is, we define entanglement by defining what it is *not*. For pure states, the definition is fairly straightforward. For N quantum systems, each spanning a Hilbert space $\mathcal{H}_i \in \{\mathcal{H}_1, \mathcal{H}_2, \dots, \mathcal{H}_N\}$, a pure entangled state is any state which *cannot* be written as a separable product state

$$|\psi\rangle = |\psi_1\rangle \otimes |\psi_2\rangle \otimes \dots \otimes |\psi_N\rangle. \quad (3.2)$$

In other words, an entangled state is one in which quantum information exists within inter-qubit correlations, rather than in single-qubit states. An entangled state is therefore a superposition of multi-qubit, correlated states.

To specialize to a bipartite (subspaces \mathcal{H}_A and \mathcal{H}_B), two-level system with eigenstates $|gg\rangle, |ge\rangle, |eg\rangle$, and $|ee\rangle$, we can examine two exemplar states for an illustration. Suppose we prepare both systems in an X -polarized state, $|\psi\rangle = \frac{|g\rangle + |e\rangle}{\sqrt{2}}$. Then the full quantum state is given by

$$|\psi\rangle = \frac{|gg\rangle + |ge\rangle + |eg\rangle + |ee\rangle}{2} = \frac{|g\rangle + |e\rangle}{\sqrt{2}} \otimes \frac{|g\rangle + |e\rangle}{\sqrt{2}} \quad (3.3)$$

While this is a highly *coherent* quantum state with a high degree of quantum superposition, it is not an *entangled* state: the fact that we can perform the direct product decomposition on the right indicates that the systems are in a separable state. If we instead consider the singlet state

$$|\psi\rangle = \frac{|ge\rangle - |eg\rangle}{\sqrt{2}}, \quad (3.4)$$

we can immediately see that there is no decomposition in which we can write Eq. (3.4) as a product of states $|\psi_A\rangle \otimes |\psi_B\rangle$. Indeed, the singlet state is a maximally-entangled Bell state. Other often-referenced entangled states in three-particle systems include variants of the Greenberger-Horne-Zeilinger (GHZ) state,

$$|\psi_{\text{GHZ}}\rangle = \frac{|ggg\rangle + |eee\rangle}{\sqrt{2}}, \quad (3.5)$$

and the W-states,

$$|W\rangle = \frac{|gge\rangle + |geg\rangle + |egg\rangle}{\sqrt{3}}. \quad (3.6)$$

These states generalize in the obvious way to many-qubit systems.

What about quantum systems that are not in a pure state, but rather must be represented as a statistical mixture of pure states? For these, we can write a similar rule: the density matrix represents an entangled state if there is *no* density matrix decomposition such that

$$\rho = \sum_i g_i \rho_1^i \otimes \rho_2^i \otimes \dots \otimes \rho_N^i \quad (3.7)$$

where g_i are real-valued degeneracy indices. The density matrix definition allows us to define entanglement even for partially mixed states, which will be critical for studying entanglement in experimental systems, where we often generate an ensemble of identically-prepared states and reconstruct the density matrix representing their average.

3.3 Useful Measures of Entanglement

We now have a definition for entanglement; however, verifying that a particular state meets the definition can be a complicated task. When studying entanglement, however, it is critical to be able to quantify the degree of entanglement. There are a number of useful entanglement measures that one can use for this purpose. Here we present several such measures, and briefly discuss the advantages, disadvantages, and implications of each. Again, this list is representative of measures we will use or reference in this dissertation; Refs. [87, 100, 101] contain a more comprehensive list.

3.3.1 Von Neumann entanglement entropy

In some senses the entanglement entropy is the essential measurement of the “amount” of entanglement in a bipartite system. It measures how much information is lost if the system is divided into two subspaces \mathcal{H}_A and \mathcal{H}_B , and subspace B is traced over (averaged out, from the perspective of subspace A). For an unentangled system made up of product states, tracing over the degrees of freedom in B has no effect on A , and no information is lost from the perspective of \mathcal{H}_A . For maximal entanglement between the two subspaces, tracing over B takes A into a fully mixed state, and all phase coherence is lost.

Quantitatively, the entanglement entropy of subspace A is given by

$$\begin{aligned} S(\rho_A) &= -\text{Tr}\{\rho_A \log_2 \rho_A\} \\ \rho_A &= \text{Tr}_B\{\rho\} \end{aligned} \quad (3.8)$$

where $S(\rho)$ is the von Neumann entanglement entropy and Tr_B is the partial trace over subspace \mathcal{H}_B . $S(\rho)$ is zero for a density matrix representing a pure state, because there is only one configuration in which the system can exist. Nonzero entanglement entropy indicates that the partial trace has caused mixing - an indication that information was contained in multi-qubit correlations, and therefore that entanglement exists. Of course, nonzero von

Neumann entanglement entropy indicates nonseparability only if acting on a pure initial state in $\mathcal{H}_A \oplus \mathcal{H}_B$, because a mixed state intrinsically has nonzero entanglement entropy regardless of whether or not the state is in fact separable. In addition, we've arbitrarily chosen the subdivision of spaces, while a general multi-qubit system will have many possible subdivisions. Nonzero entanglement entropy therefore does not confirm or reject the hypothesis that the system as a whole is in a non-separable state.

3.3.2 Entanglement of formation

The entanglement of formation is designed to extend the entanglement entropy to better capture the entanglement in a mixed state. It represents the minimum total entanglement entropy according to the following:

$$E(\rho) = \inf_{g_k, |\phi_k\rangle} \sum_k p_k S[(\rho_A)_k] \quad (3.9)$$

$$\rho = \sum_k g_k |\phi_k\rangle\langle\phi_k| \quad (3.10)$$

Here, the summed term in Eq. (3.9) represents the weighted entanglement entropy of pure states in the non-unique decomposition (Eq. (3.10)) of the density matrix ρ . The infimum represents the greatest lower bound of that entropy across all possible decompositions of ρ into a weighted sum of pure states [101, 102]. If there is no possible decomposition of the density matrix such that the entropy of entanglement is zero, then subspace \mathcal{H}_A is entangled with subspace \mathcal{H}_B .

In order to see the difference between entanglement entropy and the entanglement of formation, consider the density matrix spanning two two-level systems, given by

$$\rho = \frac{1}{4} \begin{pmatrix} 1 & 0 & 0 & 0 \\ 0 & 1 & 0 & 0 \\ 0 & 0 & 1 & 0 \\ 0 & 0 & 0 & 1 \end{pmatrix} \quad (3.11)$$

This is obviously a highly mixed, completely separable state. The von Neumann entanglement entropy of this density matrix, however, is $S = 2 \ln 2$, which is manifestly nonzero. However, we can make the decomposition

$$\rho = \frac{1}{4} |gg\rangle\langle gg| + \frac{1}{4} |ge\rangle\langle ge| + \frac{1}{4} |eg\rangle\langle eg| + \frac{1}{4} |gg\rangle\langle gg| \quad (3.12)$$

such that ρ represents an equally weighted sum of pure separable states. We immediately see that $E(\rho) = 0$ in this case, and therefore there is no entanglement according to this measure. This demonstrates why $E(\rho)$ may be a more informative measure of entanglement in mixed density matrices.

The advantage of the entanglement of formation is that it can be applied to a system of arbitrary size. However, evaluating it generally requires doing a full tomographic reconstruction of the density matrix, which can be experimentally prohibitive. Therefore, it is not often practical to calculate the entanglement of formation for a multiqubit experiment.

3.3.3 Entanglement witnesses

Entanglement witnesses are a class of useful measurements \hat{W} which take on a negative value ($\text{Tr}\{\rho\hat{W}\} < 0$) if and only if ρ is an entangled state. Entanglement witnesses are generally linear combinations of correlation measurements between \mathcal{H}_A and \mathcal{H}_B , such that the witness is evaluated using joint probability distributions within the quantum state. Witnesses are extremely useful in that they are observables, and can therefore be constructed without prior knowledge of the quantum state; however, they are not in general universal measures - for a given witness, there may be an entangled state for which $\text{Tr}\{\rho\hat{W}\} \geq 0$. Entanglement witnesses can therefore be used to confirm entanglement, but not to rule it out [101]. A useful method to optimize entanglement witnesses is provided in Ref. [103].

3.3.4 CHSH measurement

The CHSH inequality, originally derived by Clauser, Horne, Shimony and Holt [104, 105] as a generalization of the Bell inequality experiment [106] is perhaps the most famous of all bipartite entanglement witnesses. The Bell inequality showed for the first time that one could design an experiment to directly test the hotly debated question of whether the presence of a local hidden variable, shared between two distant quantum systems, could suffice to restore determinism to quantum mechanics. The violation of a Bell-type inequality is a direct indication of stronger correlations than are possible in a classically deterministic system; if the violation were to occur in a *loophole-free* manner, this would provide confirmation of quantum non-locality. Several recent landmark experiments [88–90] claim to have done just that, although the completeness of these experiments is still the subject of some scrutiny.

A Bell witness is constructed by preparing many copies of a test state spanning two-level Hilbert spaces \mathcal{H}_A and \mathcal{H}_B that are separately addressable and measurable. For each copy, a random decision is made to measure the two systems on one of two axes $\hat{\mathbf{n}}_A \in \{\hat{\mathbf{n}}_{A,1}, \hat{\mathbf{n}}_{A,2}\}$, $\hat{\mathbf{n}}_B \in \{\hat{\mathbf{n}}_{B,1}, \hat{\mathbf{n}}_{B,2}\}$. Here, the unit-length measurement axis defines a measurement operator $\hat{\mathcal{M}}_{i,j} = \hat{\mathbf{n}}_{i,j} \cdot \hat{\sigma}_i$, where $\hat{\sigma}_i \equiv \hat{\sigma}_i^X \hat{\mathbf{x}} + \hat{\sigma}_i^Y \hat{\mathbf{y}} + \hat{\sigma}_i^Z \hat{\mathbf{z}}$. One then constructs the Bell witness,

$$\mathcal{B} = \left\langle \hat{\mathcal{M}}_{A,1} \hat{\mathcal{M}}_{B,1} \right\rangle + \left\langle \hat{\mathcal{M}}_{A,1} \hat{\mathcal{M}}_{B,2} \right\rangle + \left\langle \hat{\mathcal{M}}_{A,2} \hat{\mathcal{M}}_{B,2} \right\rangle - \left\langle \hat{\mathcal{M}}_{A,2} \hat{\mathcal{M}}_{B,1} \right\rangle \quad (3.13)$$

It can be shown that no system which is classical or respects local realism can produce measures $|\mathcal{B}| \leq 2$; however, an entangled state can produce up to $|\mathcal{B}| \leq 2\sqrt{2}$ due to quantum correlations. The equality holds when the system is in a pure entangled state, the local measurement axes are perpendicular ($\hat{\mathbf{n}}_{i,1} \cdot \hat{\mathbf{n}}_{i,2} = 0$), and the measurement axes are rotated

between the two systems by $\theta = \pi/4$. Thus, a CHSH outcome with $\mathcal{B} > 2$ indicates that the system under study is indeed entangled.

A chief advantage of the CHSH approach is that it involves a set of direct measurements of the quantum system. Unlike other measures we will see later in this section, one need not infer the full density matrix of the quantum system in order to show CHSH inequality violation using a Bell witness. However, a CHSH inequality violation is a more stringent requirement than other entanglement measures. Entanglement is a necessary but insufficient condition for violating the CHSH inequality; or, violating local realism is more difficult than proving entanglement.

3.3.5 Tomographic methods

There are a number of useful measures of entanglement that require the reconstruction of the full density matrix. At first glance, these methods might seem to be redundant - after all, once one knows the full quantum state of a system, it would seem trivial to declare whether or not that state is entangled. However, when we consider a partially mixed density matrix that perhaps resembles, but is not perfectly identical to, a known entangled state, it is useful to be able to quantitatively analyze the degree of entanglement within that system and compare it to the entanglement in other mixed states.

The concurrence \mathcal{C} , first derived by Wootters [107], is a oft-cited measure of entanglement in two-qubit systems. Concurrence is a monotone of two-qubit entanglement: it ranges from zero, for a state that cannot be distinguished from a classical mixture, to unity, for a pure entangled state. As with the entanglement of formation, any nonzero concurrence is evidence of a nonseparable density matrix. Concurrence is generated by first reconstructing the full density matrix via tomographic methods (which will be discussed in greater detail in the experimental chapters to follow). We then take the ranked eigenvalues $\lambda_1, \dots, \lambda_4$, in increasing order, of the matrix $\rho\tilde{\rho}$, where $\tilde{\rho}$ is the time-reversed density matrix¹ generated by

$$\tilde{\rho} = \hat{\sigma}^{YY} \rho^* \hat{\sigma}^{YY} \quad (3.14)$$

and σ^{ij} represents the joint Pauli operator $\hat{\sigma}_A^i \otimes \hat{\sigma}_B^j$. The concurrence is then given by

$$\mathcal{C} = \max \left[0, \sqrt{\lambda_4} - \sqrt{\lambda_3} - \sqrt{\lambda_2} - \sqrt{\lambda_1} \right] \quad (3.15)$$

This formula, while exact, is rather opaque. To provide a more intuitive understanding of concurrence, we note that there are two entangled subspaces of a two-qubit system: the odd-parity subspace, spanned by $|ge\rangle$ and $|eg\rangle$, and the even-parity subspace, spanned by

¹ As Sakurai shows on pp. 277-280 of Ref. [108], “time-reversed” equivalently means spin-flipped. As noted by Wootters in [109], the spin-flip operation takes a density matrix representing a product state into an orthogonal state, such that $\rho\tilde{\rho}$ goes to zero. A pure entangled state, however, is invariant under this operation (up to a global phase). This gives some intuition for the utility of the product $\rho\tilde{\rho}$ in quantifying entanglement.

$|gg\rangle$ and $|ee\rangle$. In the special case that we know into which subspace we expect the system to fall, we can use a more transparent approximation for the concurrence [110]. Writing the density matrix as

$$\rho = \sum_{ij,kl=g,e} \rho_{ij,kl} |ij\rangle\langle kl|, \quad (3.16)$$

we approximate the concurrence as:

$$\mathcal{C} = 2 \max [0, |\rho_{ge,eg}| - \sqrt{\rho_{gg,gg}\rho_{ee,ee}}] \quad (\text{Odd parity}) \quad (3.17)$$

$$\mathcal{C} = 2 \max [0, |\rho_{gg,ee}| - \sqrt{\rho_{ge,ge}\rho_{eg,eg}}] \quad (\text{Even parity}) \quad (3.18)$$

These formulae are most valid when the off-diagonal elements outside the target subspace are all negligible: that is, when $\rho_{ge,eg}$ is the only significant off-diagonal [Eq. (3.17)] or when $\rho_{gg,ee}$ is the only significant off-diagonal [Eq. (3.18)].

Now the meaning of the concurrence becomes clear: it is in essence the balance between the amplitude of the coherent off-diagonal element within the desired subspace on the one hand, and the residual population in the subspace of opposite parity on the other. These formulae are valid when the system under study is well-projected into either the even- or the odd-parity subspace, such that the off-diagonal elements not included in the concurrence calculation become negligible.

Concurrence is extremely useful as a quantitative measure of entanglement in a bipartite system, and we will use it extensively in this dissertation (Chapters 5 and 6 in particular). The drawback of concurrence, however, is that it does not provide information about *which* entangled state is generated, given that Eq. (3.17)-(3.18) rely only on the magnitude of the off-diagonal element and not on its phase. For applications in which we are interested not in generating entanglement *per se* but in generating a specific entangled state, concurrence may not be a useful measure.

For experiments in which we require the generation of a specific entangled state, the fidelity \mathcal{F} becomes the most natural measure. Here, we simply take the projection of the density matrix onto the pure entangled state of choice [111]:

$$\mathcal{F}_{|\psi\rangle}(\rho) = \langle\psi|\rho|\psi\rangle. \quad (3.19)$$

In the case that the density matrix represents a pure state $|\psi\rangle\langle\psi|$, state vector normalization gives $\mathcal{F}_{\max} = 1$. One can also show that a fully mixed state in the subspace of interest will give $\mathcal{F}_{\text{mixed}} = 0.5$. Thus if $0.5 < \mathcal{F} \leq 1$, we have both confirmed the existence of entanglement and further shown that we have produced, with varying quality, the entangled state of our choice. We will use fidelity in Chapter 7, where we will be interested in preparing specific entangled states.

Fidelity can also be a useful measure if we are comparing our density matrix not to a pure state, but to another mixed or pure density matrix. In this case, letting ρ_t represent the target density matrix, the generalized fidelity is given by [111]

$$\mathcal{F}(\rho_t, \rho) = \left[\text{Tr} \left\{ (\sqrt{\rho_t} \rho \sqrt{\rho_t})^{1/2} \right\} \right]^2. \quad (3.20)$$

One can show that this reduces to Eq. (3.19) in the special case that ρ_t represents a pure state. We should also note that some papers use $\mathcal{F}' = \sqrt{\mathcal{F}}$ to represent fidelity, so one should be careful to note which convention is in use when assessing and comparing claims.

Chapter 4

The Superconducting cQED Architecture

The theory of quantum electrodynamics describes Nature as absurd from the point of view of common sense. And it agrees fully with experiment. So I hope you accept Nature as She is —absurd.

Richard Feynman, *QED: The Strange Theory of Light and Matter*,
1985

In this chapter, we review the experimental building blocks of the superconducting qubit architecture. Specifically, we discuss the quantum circuits used to generate an approximate two-level system with lifetimes sufficient to do coherent quantum operations [20, 35, 36, 39, 113–117]; the light-matter interactions used to control, couple, and read out the state of the qubits [23, 75, 118, 119]; and the amplifiers used to transport the quantum-limited signals used to make measurements from their 30 mK base temperature through to room temperature electronics while adding minimal noise.

Superconducting quantum information is a rapidly developing experimental field, and it is beyond the scope of this dissertation to provide a comprehensive review of the field. Instead, we will focus here on the techniques and circuits used to implement the experiments in this dissertation: the transmon qubit, coupled dispersively to a linear resonator, and read out using a Josephson parametric amplifier. There are a number of extremely useful texts which provide a more in-depth accounting of the scope of techniques in superconducting circuit and cavity quantum electrodynamics (cQED) [22, 119–123]. In this review chapter, we will not present detailed derivations, but rather will outline the mathematics required to derive and understand the system and provide references to original and pedagogical resources, such that the reader will have sufficient context for understanding the remainder of this dissertation.

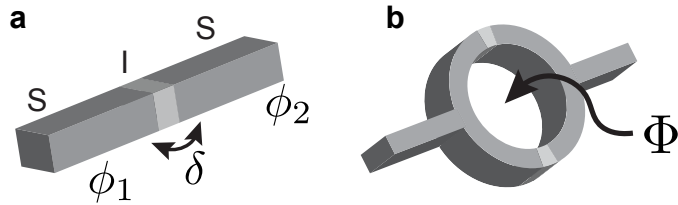


Figure 4.1: Josephson junctions, defined by (a) a superconducting phase difference across the junction, which is equivalently a nodal flux. (b) If two junctions are joined in parallel by a closed loop, the flux can be tuned by the introduction of an external magnetic field.

4.1 Superconducting Qubits

The field of superconducting quantum information has exploded since the observation of the first coherent quantum oscillation in a Cooper pair box (CPB) circuit [36]. There are a multitude of superconducting qubit implementations with relative strengths and weaknesses, but all rely on the Josephson junction [124], a weak link that creates a tunneling barrier for Cooper pairs between two (or more) superconducting islands. The Josephson current and voltage relations for a superconducting tunnel junction give

$$I = I_0 \sin \delta = \frac{2\pi}{\Phi_0} E_J \sin \delta; \quad (4.1a)$$

$$V = \frac{\hbar}{2e} \frac{d\delta}{dt} = \frac{\Phi_0}{2\pi} \frac{d\delta}{dt} \quad (4.1b)$$

where Φ_0 is the flux quantum $h/2e$, E_J is the Josephson energy, and δ is the difference in superconducting phase between the two islands (Figure 4.1a). I_0 sets the current above which the tunneling gap is crossed and normal (resistive) current can propagate. The phase δ can be written alternatively as

$$\delta = 2\pi \frac{\Phi}{\Phi_0}, \quad (4.2)$$

where Φ is the nodal flux at a fixed point in the circuit. This definition becomes particularly useful if we join two Josephson junctions in parallel by a closed loop; then, Φ represents the flux through the loop, which is typically an externally controllable parameter (Figure 4.1b).

We can re-arrange these equations to find the nonlinear Josephson inductance

$$L_J = \frac{\hbar}{2e} \frac{1}{I_0 \cos \delta} = \left(\frac{\Phi_0}{2\pi} \right)^2 \frac{1}{E_J \cos \delta} \equiv \frac{L_{J0}}{\cos \delta}. \quad (4.3)$$

The Hamiltonian describing the Cooper pairs moving through junction is given by

$$\hat{H} = 4E_C(\hat{n} - n_g)^2 - E_J \cos \hat{\delta} \quad (4.4)$$

where $E_C = e^2/2C$ is the charging energy required to move a single electron from one island to the next, C is the total capacitance of the junction (including that intrinsic to the junction and any additional geometric capacitance), \hat{n} is the number of Cooper pairs on one of the islands, and n_g represents an offset charge due to external electrical field or native charge impurities. The $E_J \cos \delta$ term emerges from a tight binding model of Cooper pair tunneling. If we take δ to be small and consider only the linear inductance, this Hamiltonian can be rewritten as a simple Harmonic oscillator,

$$\hat{H} = \frac{1}{2C} \hat{Q}^2 + \frac{1}{2L_{J0}} \hat{\Phi}^2, \quad (4.5)$$

where \hat{Q} and $\hat{\Phi}$, representing charge and flux, are conjugate variables [125]. This represents a linear resonator with transition energy

$$\omega^q = \sqrt{\frac{1}{L_{J0}C}} = \frac{1}{\hbar} \sqrt{8E_J E_C}. \quad (4.6)$$

Of course, a linear resonator, whose quadratic potential produces a harmonic oscillator with evenly spaced excitations, will not serve our purposes as a quantum bit. We require a nonlinearity in the energy required to excite nearest-neighbor level transitions in order to have any hope of isolating the lowest two levels $|g\rangle$ and $|e\rangle$ and treating them as an approximate two-level system. In order to see the effects of the nonlinearity we must consider higher order terms by evaluating the full Hamiltonian Eq. (4.4), whose eigenfunctions are given by the Mathieu functions. As shown in Figure 4.2, these functions are periodic in n_g , and so we expect a qubit based on this Hamiltonian to be sensitive to charge noise, particularly at bias points detuned from the charge degeneracy points at $n_g = \pm m/2$ (where m is an integer). Indeed, the first coherent oscillations seen in a superconducting circuit were performed in a CPB, and had a phase coherence time of only 2 ns [36]. The wide range of qubit designs developed over the last nearly twenty years aim to overcome this charge noise without introducing other sources of noise sensitivity.

4.1.1 The transmon qubit

The transmon qubit, which we will use exclusively in this dissertation, uses a large external capacitance to ameliorate the charge noise sensitivity in the CPB. Koch *et al.* showed that the charge dispersion for the k -th level is exponentially suppressed in the ratio E_J/E_C according to [114]

$$E_k(n_g) = E_k + \frac{\epsilon_k}{2} \cos(2\pi n_g); \quad (4.7a)$$

$$E_k \approx -E_J + \sqrt{8E_J E_C} \left(k + \frac{1}{2} \right) - \frac{E_C}{12} (6k^2 + 6k + 3); \quad (4.7b)$$

$$\epsilon_k \approx (-1)^k \frac{2^{4k+5}}{k!} \sqrt{\frac{2}{\pi}} E_C \left(\frac{E_J}{2E_C} \right)^{\frac{k}{2} + \frac{3}{4}} e^{-\sqrt{8E_J/E_C}}. \quad (4.7c)$$

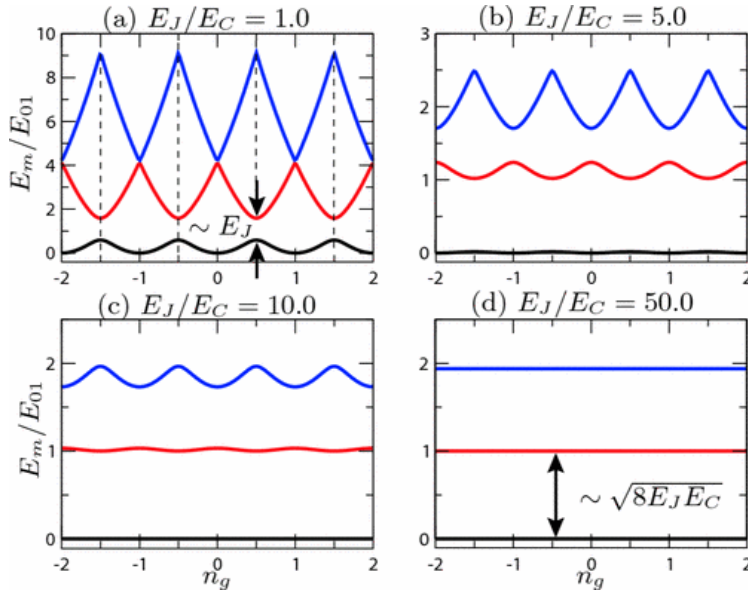


Figure 4.2: The CPB spectrum, as a function of n_g , for a range of E_J/E_C . We see that as this ratio increase (from panels a - d), the undulations of the bands as a function of n_g decrease, indicating an amelioration of charge-noise sensitivity. Reproduced with permission from Ref. [114].

The modulation of the energy spectrum as a function of offset charge is now approximated as a sinusoidal term whose amplitude is given by ϵ_k . Eq. (4.7c) indicates that this amplitude is exponentially damped by the ratio E_J/E_C ; reducing E_C therefore ought to be a straightforward route to damping the charge dependence of the energy level splittings. Figure 4.2 shows this damping for a range of E_J/E_C ; we see that when this ratio is greater than 50, the oscillations are effectively flat and the circuit has been made charge-insensitive. This is referred to as the transmon regime of the CPB architecture.

the transmon qubit is implemented by shunting the CPB by a large parallel capacitance, such that $E_C/h \approx 200$ MHz. The addition of a shunt capacitance leads to a renormalization of the resonant frequency of the circuit; the bare energy levels in Eq. (4.7b) indicate that the resonant qubit frequency becomes $\hbar\omega^q = E_1 - E_0 \approx \sqrt{8E_JE_C} - E_C$. In Figure 4.3, we show a circuit and schematic design for a transmon qubit, and a SEM micrograph of Josephson junctions similar to those used in this dissertation to implement the transmon circuit.

With a typical Josephson energy given by $E_J/h \approx 20$ GHz, the transmon $E_J/E_C \approx 100$ is sufficient to dramatically reduce the charge sensitivity, and thus to ameliorate a critical source of dephasing. Because typical $\omega^q/2\pi \approx 6$ GHz has a characteristic transition temperature $T_Q = \hbar\omega^q/k_B \approx 300$ mK, we perform experiments in a dilution refrigerator with base temperature $T_B \approx 10 - 30$ mK in order to limit spurious thermal excitations of

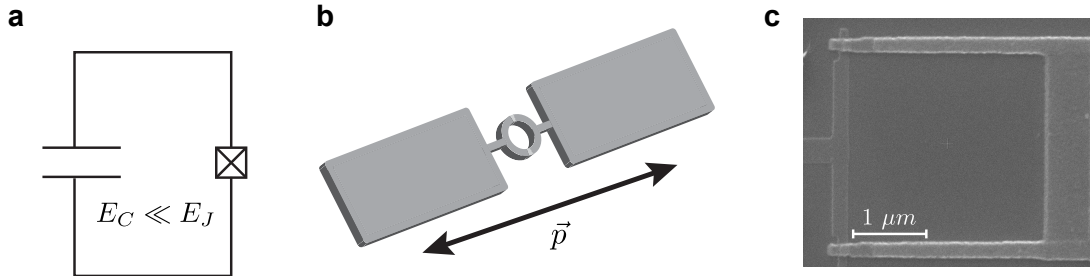


Figure 4.3: Transmon qubit. a) The circuit design for a transmon qubit, with $E_C \ll E_J$ in order to suppress charge noise. b) The schematic design of a typical transmon qubit implementation (not to scale), with a large dipole moment \vec{p} aligned with the axis of the antenna pads as shown. c) A SEM micrograph at 50,000x of the central SQUID junction, which provides the nonlinear inductance required for a well-isolated two level system. SEM image courtesy of Vinay Ramasesh.

the qubit.

The price that we pay for the reduction in charge sensitivity in the transmon qubit is the anharmonicity. While the un-shunted CPB can have anharmonicity on the order of several GHz at the charge-insensitivity bias point, the transmon anharmonicity is reduced to $\alpha \equiv \omega_{ef} - \omega_{ge} = -E_C/\hbar$, where $\hbar\omega_{ij} = E_j - E_i$ and $\{g, e, f\}$ represent the first three energy levels of the transmon. An anharmonicity of several hundred MHz is sufficient to allow us to drive transitions between $|g\rangle$ and $|e\rangle$ without exciting off-resonant transitions to the second excited state $|f\rangle$, provided that the pulses used to drive the transitions are sufficiently long, on the order of $\tau > 20$ ns such that $1/\tau \ll |\alpha|$. However, additional pulse shaping [126–129] can be used to relax this limit, so the reduced anharmonicity is not a critical barrier.

The transmon qubit and its variants, because of their simplicity and straightforward design, have become one of the workhorses of the superconducting qubit community. (Other qubit geometries - most notably the flux qubit [116, 130–132] - are also in use and have some comparative advantages, most notably an increased anharmonicity.) Transmon qubits can be designed and fabricated using now-standard techniques and are easily integrated into complex circuits for readout and coupling. They also are readily tunable via the application of external flux. In this dissertation, we implement the 3D transmon architecture [115]: we fabricate transmon qubits on undoped silicon, and load them in a resonant microwave cavity. Placing the qubit in a cavity is useful both for providing shielding from the electromagnetic environment (enhancing qubit lifetime via the Purcell effect), and as we will see in the upcoming sections, for enabling us to perform a QND measurement of the qubit state.

4.2 The Jaynes Cummings Hamiltonian

The elongated design of the capacitor pads that we use to shunt the Josephson junction(s) in our qubits, shown in Figure 4.3b, allows them to serve a dual purpose. They reduce E_C , providing a qubit well into the transmon regime of $E_J \gg E_C$, while also providing an electric dipole moment that enhances the qubit's coupling to its local electromagnetic environment. Effective qubit control and readout relies on understanding and control of this coupling. The minimal description of atom-light interactions is provided by the Jaynes-Cummings Hamiltonian, which we will derive and describe in this section.

4.2.1 Derivation

The interaction between a dipole and an electric field is given classically by¹

$$\hat{H}_{\text{int}} = -\vec{\mathbf{E}}(t) \cdot \vec{\mathbf{p}} = -\hat{\boldsymbol{\epsilon}} E(t) \cdot \vec{\mathbf{p}} \quad (4.8)$$

Quantum mechanically, a microwave cavity's field modes can be described as quantum harmonic oscillators [9] with creation and annihilation operators \hat{a}^\dagger and \hat{a} and resonant frequency ω^c . The vacuum fluctuations of the field are given by [125]

$$\vec{\mathbf{E}} = \hat{\boldsymbol{\epsilon}} E_{ZPF} (\hat{a} + \hat{a}^\dagger) \quad (4.9)$$

where $E_{ZPF} = (\hbar\omega^c / 2\epsilon_0 V)$ is the RMS amplitude of the field fluctuations, and V is the effective mode volume. The Hamiltonian describing the interaction between the field mode and a dipole with two states $\{|g\rangle, |e\rangle\}$ is thus given by

$$\hat{H}_{\text{int}} = \sum_{i,j=g,e} -E_{ZPF} \langle i | \vec{\mathbf{p}} \cdot \hat{\boldsymbol{\epsilon}} | j \rangle (\hat{a} + \hat{a}^\dagger) |i\rangle\langle j| \quad (4.10)$$

By parity arguments, we know that the dipole-field coupling cannot have diagonal density matrix elements; if we (without loss of generality) assume the off-diagonal matrix element to be real, we can then write the interaction Hamiltonian as²

$$\hat{H}_{\text{int}} = \hbar g_{qc} (\hat{a} + \hat{a}^\dagger) \hat{\sigma}^X \quad (4.11a)$$

$$g_{qc} = -\frac{1}{\hbar} \langle \psi_g | \vec{\mathbf{p}} \cdot \hat{\boldsymbol{\epsilon}} | \psi_e \rangle E_{ZPF} \quad (4.11b)$$

¹ There is an ambiguity in the notation here that we inherit from physics conventions. Both geometric unit vectors and Hamiltonian operators are indicated with a “x” circumflex diacritic. The two rarely appear together in this dissertation, but for the sake of clarity we distinguish them by showing unit vectors additionally in bold.

² We use the notation g_{qc} here to denote the qubit-cavity coupling rate. The standard notation for this coupling is g ; however, since we use $\{g, e, f\}$ to index qubit states, we add a subscript to the coupling term to avoid ambiguity.

It is convenient to rewrite the qubit terms using raising and lowering operators $\hat{\sigma}^\pm \equiv (\hat{\sigma}^X \pm i\hat{\sigma}^Y)/2$. The Hamiltonian then becomes $\hat{H}_{\text{int}} = \hbar g_{qc}(\hat{a} + \hat{a}^\dagger)(\hat{\sigma}^+ + \hat{\sigma}^-)$. The full (nondissipative) system Hamiltonian is given by the sum of the bare resonator terms (\hat{H}_a), the bare qubit terms (\hat{H}_q), and the interaction (\hat{H}_{int}):

$$\begin{aligned}\hat{H}_{\text{tot}} &= \hat{H}_a + \hat{H}_q + \hat{H}_{\text{int}} \\ &= \hbar\omega^c\hat{a}^\dagger\hat{a} + \frac{\hbar\omega^q}{2}\hat{\sigma}^Z + \hbar g_{qc}(\hat{a}\hat{\sigma}^+ + \hat{a}^\dagger\hat{\sigma}^-) + \hbar g_{qc}(\hat{a}\hat{\sigma}^- + \hat{a}^\dagger\hat{\sigma}^+)\end{aligned}\quad (4.12)$$

where $|g\rangle$ has been chosen to represent the $\langle\hat{\sigma}^Z\rangle = -1$ state and $|e\rangle$ the $\langle\hat{\sigma}^Z\rangle = +1$ state. In Eq. (4.12) we have grouped the terms according to excitation-conserving and excitation non-conserving terms. If ω^c and ω^q are reasonably close to one another, then going into a rotating frame with respect to either will lead to rapid oscillations in the $\hat{a}\hat{\sigma}^-$ and $\hat{a}^\dagger\hat{\sigma}^+$ terms; it is thus customary to drop these terms (the rotating wave approximation, RWA). While the RWA is not always appropriate [133], it is usually a good approximation at the single-photon levels we will typically use in this work. We will refer to the Hamiltonian under the RWA as \hat{H}_{JC} , the Jaynes-Cummings (JC) Hamiltonian:

$$\hat{H}_{JC} = \hbar\omega^c\hat{a}^\dagger\hat{a} + \frac{\hbar\omega^q}{2}\hat{\sigma}^Z + \hbar g_{qc}(\hat{a}\hat{\sigma}^+ + \hat{a}^\dagger\hat{\sigma}^-)\quad (4.13)$$

Defining $\Delta \equiv \omega^q - \omega^c$, there are two useful limits to the JC Hamiltonian: near-resonant ($|\Delta| \ll g_{qc}$) and dispersive ($|\Delta| \gg g_{qc}$). We will generally work within the dispersive limit in this dissertation, but we can gain useful intuition by first examining the opposite limit, $|\Delta| \ll g_{qc}$.

4.2.2 Near-resonant case

The JC Hamiltonian is well-parametrized by states $|n, g/e\rangle$, where n represents the Fock state of the resonator. Under the RWA, the Hamiltonian is block-diagonal, coupling terms of the form $|n, e\rangle \leftrightarrow |n+1, g\rangle$. In a two-dimensional subspace indexed by the n -th Fock state, the Hamiltonian is

$$\hat{H}_{JC}(n) = \hbar\omega^c \left(n + \frac{1}{2} \right) \hat{\sigma}^I + \frac{\hbar(\omega^q - \omega^c)}{2} \hat{\sigma}^Z + \hbar g_{qc} \sqrt{n+1} \hat{\sigma}^X\quad (4.14)$$

where $\hat{\sigma}^Z = +1$ now corresponds to $|n, e\rangle$ and $\hat{\sigma}^Z = -1$ corresponds to $|n+1, g\rangle$. If $g_{qc} \rightarrow 0$, the eigenvalues become $\hbar\omega^c \pm \frac{\hbar\omega^q}{2}$ as expected. If the qubit and cavity are near resonance such that $|\Delta| \equiv |\omega^q - \omega^c| \ll g_{qc}$, nearly-degenerate perturbation theory shows that there is

an avoided crossing between the qubit and cavity modes according to [134]

$$E_{\pm}(n) = \hbar\omega^c \left(n + \frac{1}{2} \right) \pm \frac{\hbar}{2} \sqrt{\Delta^2 + 4g_{qc}^2(n+1)} \quad (4.15a)$$

$$|n,+\rangle = \sin\left(\frac{\Theta_n}{2}\right) |n+1,g\rangle + \cos\left(\frac{\Theta_n}{2}\right) |n,e\rangle \quad (4.15b)$$

$$|n,-\rangle = \cos\left(\frac{\Theta_n}{2}\right) |n+1,g\rangle - \sin\left(\frac{\Theta_n}{2}\right) |n,e\rangle \quad (4.15c)$$

$$\tan(\Theta_n) = \frac{2g_{qc}\sqrt{n+1}}{\Delta} \quad (4.15d)$$

When $\Delta = 0$ and the qubit and resonator modes are degenerate, the dressed eigenstates become symmetric and antisymmetric combinations of the bare eigenstates $|n, \pm\rangle = (|n+1,g\rangle \pm |n,e\rangle)/\sqrt{2}$ with energies $E_{\pm}(n) = \hbar(n\omega^c \pm g_{qc})$. An excitation that is initialized in the qubit (or in the cavity) will coherently oscillate between the two systems at a rate $2g_{qc}\sqrt{n+1}$. For transmon qubits with g_{qc} on the order of tens to hundreds of MHz and qubit lifetimes in excess of 10 μ s, the upper and lower polaritons defined by E_{\pm} can be well-resolved in frequency-domain spectroscopy, leading to a vacuum Rabi splitting well into the strongly-coupled regime ($g_{qc} \gg \kappa, 1/T_1, 1/T_\phi$).

4.2.3 Dispersive (far-detuning) limit

When we go to the limit of $\Delta \gg g_{qc}$, we intuitively no longer expect coherent swapping of excitations between the cavity and the qubit, but the effect of the finite coupling must still manifest in some way. To determine the effect of the coupling, we will transform to a rotating frame in which the off-diagonal terms in the $|n,e\rangle, |n+1,g\rangle$ subspace go to zero, such that there are no undriven transitions between the two states. For this purpose, we will treat the coupling as a perturbation:

$$\hat{H} = \hat{H}_0 + \hat{H}_1; \quad (4.16a)$$

$$\hat{H}_0 = \hbar\omega^c \hat{a}^\dagger \hat{a} + \frac{\hbar\omega^q}{2} \hat{\sigma}^Z; \quad (4.16b)$$

$$\hat{H}_1 = \hbar g_{qc} (\hat{a}^\dagger \hat{\sigma}^- + \hat{a} \hat{\sigma}^+) \quad (4.16c)$$

We would like to find a unitary rotation that cancels the perturbation to lowest order. In the rotated frame, the Hamiltonian will be given by $\hat{H}' = \hat{U} \hat{H} \hat{U}^\dagger$, where \hat{U} is a unitary transformation $\hat{U} = e^{\hat{c}}$. The Baker-Hausdorff relation

$$e^{\hat{c}} \hat{H} e^{-\hat{c}} = \hat{H} + [\hat{c}, \hat{H}] + \frac{1}{2!} [\hat{c}, [\hat{c}, \hat{H}]] + \dots \quad (4.17)$$

suggests that a good unitary transformation will be one in which the perturbation is cancelled at lowest order: in other words, we need an operator \hat{c} such that the first commutator satisfies

$[\hat{c}, \hat{H}_0] = -\hat{H}_1$. This condition is met when we use

$$\hat{c} = \frac{\hbar g_{qc}}{\Delta} (\hat{a}\hat{\sigma}^+ - \hat{a}^\dagger\hat{\sigma}^-). \quad (4.18)$$

Since we are treating g_{qc} as a perturbative term, we keep only terms in Eq. (4.17) that are up to quadratic in g_{qc} . Defining the dispersive cross-Kerr term $\chi = g_{qc}^2/\Delta$, we are thus left with the JC Hamiltonian in the dispersive limit:

$$\hat{H}'_{JC}/\hbar = \omega^c \hat{a}^\dagger \hat{a} + \frac{\omega^q}{2} \hat{\sigma}^Z + \chi \left(\hat{a}^\dagger \hat{a} + \frac{1}{2} \right) \hat{\sigma}^Z. \quad (4.19)$$

The factor of $(\chi/2)\hat{\sigma}^Z$ represents the Lamb shift of the qubit frequency due to the interaction with the cavity mode; the interaction in the rotated frame is given by $\hat{H}'_{int} = \hbar\chi\hat{a}^\dagger\hat{a}\hat{\sigma}^Z$.

The dressed eigenstates in this approximation are identical to the bare eigenstates, although there is in general some weak mixing of the eigenstates given by Eq. (4.15). For a transmon qubit, whose weak nonlinearity makes the two-level system approximation less valid, the dispersive shift is slightly renormalized [114] by

$$\chi = \frac{g_{qc}^2}{\Delta} \frac{\alpha}{\alpha + \Delta}. \quad (4.20)$$

We can interpret \hat{H}'_{int} in two useful ways. The coupling between the qubit and the resonator manifests equivalently as a qubit-state dependent shift in the resonator frequency ($\omega^c \rightarrow \omega^c + \chi\hat{\sigma}^Z$); or as a resonator-occupation dependent shift in the qubit frequency ($\omega^q \rightarrow \omega^q + \chi\hat{a}^\dagger\hat{a}$). Critically, \hat{H}'_{int} commutes with the qubit state such that, as long as the dispersive approximation holds, we can use the Jaynes-Cummings interaction to non-destructively read out the state of the qubit by probing the resonant frequency of the cavity. In the next section, we will explore how this is achieved.

4.3 Dispersive Readout

Performing a measurement of the resonant frequency of the cavity in the dispersive regime is the chief method we use in this dissertation to infer the state of the qubit. In this section, we will first provide a semiclassical introduction to dispersive readout in order to gain intuition for the measurement process, and then will discuss a fully quantum treatment of the measurement using both the Bayesian and the SME formalisms developed in Chapter 2.

Our dispersive measurements are carried out by fabricating a 3D copper resonator in which we place a transmon qubit (shown schematically in Figure 4.4). The cavities generally have two ports: one weakly coupled (input) port for transmission measurements, and one strongly coupled (output) port such that virtually all photons, and thus all qubit state information, leaks from the cavity via the latter. We will monitor the output port to read

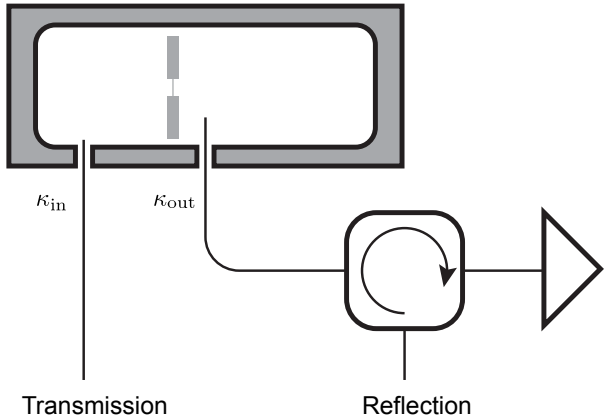


Figure 4.4: Schematic of a 3D cavity containing a transmon qubit, with weakly- and strongly-coupled ports (κ^{in} and κ^{out} , respectively) for transmission and reflection measurements.

out the state of the qubit. The two ports are labeled by their bandwidths ($\kappa^{\text{in}} \ll \kappa^{\text{out}}$); we neglect internal losses. The bandwidths of the ports are set by their position in the cavity (closer to a modal field maximum for stronger coupling), and by the extension of an antenna coupler into the cavity (the longer the coupling pin, the stronger the coupling of the port).

4.3.1 Semiclassical treatment

To understand the mechanism of the dispersive readout, we will first treat the resonator as a classical harmonic oscillator with a precisely defined amplitude and phase. We denote the complex field amplitude inside the resonator as A_{\pm} , where $+(-)$ indicates the intra-cavity field associated with the qubit in state $|e\rangle$ ($|g\rangle$). We can write the equations of motion for a cavity with frequency ω^c , probed at frequency ω^d with an input drive amplitude A_{in} as

$$\dot{A}_{\pm} = -\frac{\kappa}{2}A_{\pm} - i(\omega^c \pm \chi - \omega^d)A_{\pm} + \sqrt{\kappa^d}A_{\text{in}}. \quad (4.21)$$

Here, $\kappa \equiv \kappa^{\text{in}} + \kappa^{\text{out}}$ and κ^d is the decay rate of the driving port, which can be chosen from the weakly coupled port for transmission measurements or the strongly coupled port for reflection measurements (Figure 4.4). The steady state internal field solution is given by

$$A_{\pm} = \frac{\sqrt{\kappa^d}A_d}{\frac{\kappa}{2} + i(\omega^c \pm \chi - \omega^d)}. \quad (4.22)$$

When driven on resonance ($\omega^d = \omega^c$), the amplitude of the internal field is not qubit-state dependent ($A_+ = A_-$), but there is a state-dependent phase shift given by

$$\phi \equiv \text{Arg} \{A_{\pm}\} = \arctan(\mp 2\chi/\kappa). \quad (4.23)$$

For a transmission measurement, the field propagating from the cavity is given by $A_{\pm,\text{out}} = \sqrt{\kappa^{\text{out}}} A_{\pm}$ and therefore contains the same conditional phase shift as the intracavity field; the output field in reflection interferes with the input drive according to $A_{\pm,\text{out}} = \sqrt{\kappa^{\text{out}}} A_{\pm} - A_{\text{in}}$, yielding a net doubling of the phase shift in the propagating reflected field in comparison to the intracavity field. By measuring the phase shift of the propagating field using standard homodyne or heterodyne detection methods, we can thus infer the state of the qubit.

A measurement of the phase shift is typically the most effective means of inferring the qubit state in the weak-measurement limit, where $\chi/\kappa \ll 1$ such that the resonance profile of the cavity conditioned on the qubit in state $|g\rangle$ is very close to the resonance profile conditioned on $|e\rangle$. In the opposite limit, $\chi/\kappa \gg 1$ (often referred to as the number-resolved regime, as the qubit will have well-resolved spectral peaks conditioned on the Fock state in the cavity), qubit state information can be inferred from transmission amplitude measurements. The transmission amplitude at $\omega^d = \omega^c - \chi$ will be large if the qubit is in $|g\rangle$, but vanishing if the qubit is in $|e\rangle$. In Chapters 5 and 6 we will work in the small χ/κ limit and will use homodyne detection to infer the phase shift. In Chapter 7 we will work in the number-resolved regime but will use high-power readout [135] rather than dispersive readout of the field amplitude.

To this point, we have considered the field to have a well-defined amplitude and phase with no uncertainty, and have further neglected to consider the implications of the qubit existing in a superposition state of $|g\rangle$ and $|e\rangle$. However, to understand the dispersive measurement properly we must consider the intracavity field as a quantum object, one with conjugate variables that enforce a Heisenberg uncertainty relationship, and we further must allow the qubit to exist in a coherent superposition. In fact, we will see that it is precisely the quantum uncertainty in the intracavity field mode that causes the qubit to stochastically collapse into one of the measurement eigenstates $\langle \hat{\sigma}^Z \rangle = \pm 1$.

4.3.2 Coherent states and measurement uncertainty

As we have seen, a quantized electromagnetic field can be represented as a harmonic oscillator. The “in-phase” [$\hat{I} = (\hat{a} + \hat{a}^\dagger)/2$] and “quadrature” [$\hat{Q} = (i\hat{a} - i\hat{a}^\dagger)/2$] components of the field, corresponding to the real and imaginary components of the complex amplitude, are incompatible observables with $\Delta\hat{I}\Delta\hat{Q} \geq 1/4$. \hat{I} and \hat{Q} are the field equivalents of \hat{x} and \hat{p} in a physical quantum oscillator.

If the uncertainty in \hat{I} and \hat{Q} is equally distributed between the two quadratures such that $\Delta\hat{I} = \Delta\hat{Q}$ and the variance is isotropic in the IQ plane, the field is represented by a coherent state. A coherent state [136] is a minimum-uncertainty state represented by a

superposition of photonic Fock states,

$$|\beta\rangle = e^{-|\beta|^2/2} \sum_n \frac{\beta^n}{(n!)^{1/2}} |n\rangle, \quad (4.24)$$

where β is a complex displacement coefficient. The average photon number in the cavity is given by $\bar{n} = |\beta|^2$, and the photon number fluctuations are Poissonian: $\Delta(\hat{a}^\dagger \hat{a}) = \sqrt{\bar{n}}$. These photon-number fluctuations are the source of the uncertainty in the field quadrature amplitudes. Coherent states are generated mathematically by applying a displacement operator

$$D(\beta) = \exp(\beta \hat{a}^\dagger - \beta^* \hat{a}) \quad (4.25)$$

to the vacuum state $|0\rangle$, and they are eigenstates of the lowering operator according to

$$\hat{a} |\beta\rangle = \beta |\beta\rangle. \quad (4.26)$$

4.3.3 Unconditioned master equation

With this background on coherent states, we can now consider the effect of a cavity drive on the qubit density matrix, both in the unconditioned (dissipated) and conditioned (measured) case. Here, we follow Gambetta *et al.* [118] and sketch the important pieces of the derivation; for a full development, see the original paper. Our goal here is not to perform an exhaustive derivation, but rather to elucidate the connection between the experiments performed in this dissertation and the stochastic measurement formalism described in Chapter 2.

The cavity drive Hamiltonian is described by

$$\hat{H}_d = \hbar \epsilon^d [\hat{a}^\dagger e^{-i\omega^d t} + \hat{a} e^{i\omega^d t}], \quad (4.27)$$

where for simplicity we have treated the drive amplitude as real. The drive rate ϵ^d is connected to the classical drive amplitude A_{in} in Section 4.3.1 by $\epsilon^d = \sqrt{\kappa^d} A_{\text{in}}$. The non-dissipative Hamiltonian, in the dispersive limit and in a frame rotating at ω^d , is given by

$$\hat{H}_{\text{eff}}/\hbar = \frac{\omega^q}{2} \hat{\sigma}^Z + \Delta^{\text{cd}} \hat{a}^\dagger \hat{a} + \chi \hat{a}^\dagger \hat{a} \hat{\sigma}^Z + \epsilon^d (\hat{a}^\dagger + \hat{a}), \quad (4.28)$$

where $\Delta^{\text{cd}} \equiv \omega^c - \omega^d$ is the cavity-drive detuning.

To study the full dynamics of the system, we must now include several loss mechanisms. Photons leak from the cavity at a rate $\kappa \approx \kappa^{\text{out}}$; the qubit decays from the excited state to the ground state at a rate Γ_1 ; and phase coherence in the off-diagonal elements in the qubit subspace occurs at a rate Γ_ϕ . In the absence of a measurement, the Lindblad form of the master equation including each of these decay channels is given by [136]

$$\begin{aligned} \frac{d\rho}{dt} &= -\frac{i}{\hbar} [\hat{H}_{\text{eff}}, \rho] + \kappa \mathcal{D}[\hat{a}] \rho + \Gamma_1 \mathcal{D}[\hat{\sigma}^-] \rho + \frac{\Gamma_\phi}{2} \mathcal{D}[\hat{\sigma}^Z] \rho \\ &= \mathcal{L}_{\text{tot}} \rho \end{aligned} \quad (4.29)$$

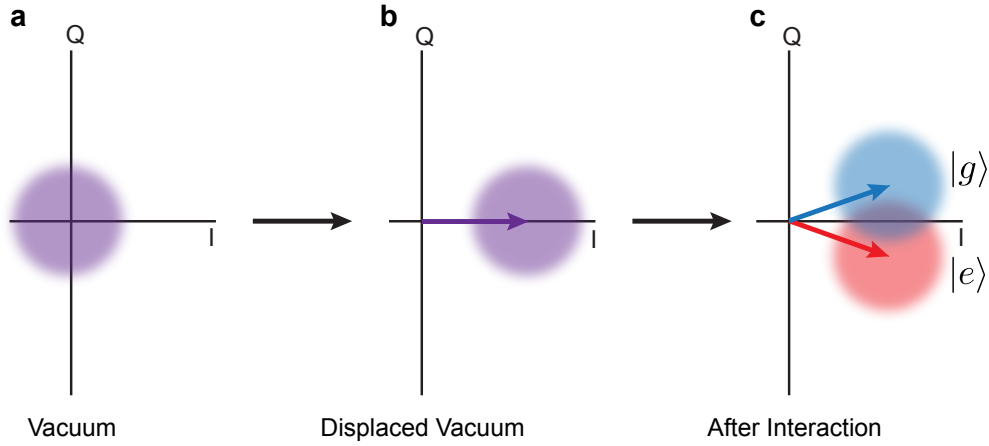


Figure 4.5: Schematic representation of the dispersive measurement. The cavity is initialized in a minimum-uncertainty coherent vacuum state (Panel a); a drive is applied to displace the vacuum along the in-phase quadrature (Panel b); and the dispersive interaction leads to a conditional phase accumulation that entangles the phase of the intra-cavity field with the state of the qubit (Panel c). The blurred “lollipops” represent the intrinsic quantum uncertainty of the intracavity field.

Here, $\mathcal{D}[\hat{c}] \rho$ is the Lindblad superoperator introduced in Section 2.3, and the density matrix spans both the two-dimensional qubit space and the infinite-dimensional Fock space of the cavity mode. We will shortly examine the dynamics in just the qubit sector (which is our primary system of interest).

If we neglect qubit decay and make a fast-cavity approximation (i.e. assume the cavity reaches steady state quasi-instantaneously and neglect transient dynamics), the density matrix evolution is described by [118, 137]

$$\rho(t) = \sum_{i,j=g,e} \rho_{ij}(t) |i\rangle\langle j| \otimes |\beta_i\rangle\langle\beta_j|. \quad (4.30)$$

Here $|\beta_i\rangle$ are coherent states whose mean displacement amplitudes and phases are identical to those derived semiclassically in Eq. (4.22). Evidently, the qubit state is entangled with the coherent state amplitude and phase within the cavity. We expect the measurement rate to be related to the overall phase shift (governed by χ and κ), and to the total displacement (governed by ϵ^d).

The diagonal density matrix elements are given by their initial values $\rho_{i,i}(t) = \rho_{i,i}(0)$,

consistent with a QND measurement, and the off-diagonal terms evolve as

$$\begin{aligned}\rho_{g,e}(t) &= \rho_{g,e}(0) \exp[i\omega^q t - \Gamma_\phi t] \frac{e^{-i2\chi\beta_e\beta_g^*}}{\langle\beta_g|\beta_e\rangle} \\ \rho_{e,g}(t) &= \rho_{g,e}^*(t)\end{aligned}\quad (4.31)$$

The quantum description of the unconditioned effect of the measurement drive is now clear. The intracavity coherent state serves as a pointer state for the qubit degree of freedom, precisely as we expect given our semiclassical intuition. We begin in a vacuum state (Figure 4.5a), apply a drive amplitude ϵ^d to generate a displaced coherent state (Figure 4.5b), and allow the qubit and field to interact such that the qubit state information becomes encoded on the average phase of the coherent state (Figure 4.5c). In the small χ/κ limit, the phase can be well-approximated by the projection onto the \hat{Q} quadrature, and the amplitude of the field (and thus the mean and fluctuating photon number) is given by projection onto the \hat{I} quadrature. If we measure the fluctuations in Q -quadrature of the field propagating from the cavity, we expect to be able to make a continuous measurement of the qubit state.

Let us now consider the unconditioned effects of the cavity drive on the qubit. To isolate the evolution in the qubit sector, we make a unitary transformation $\hat{U}\rho\hat{U}^\dagger$, where \hat{U} is given by

$$\hat{U} = |e\rangle\langle e| D(\beta_e) + |g\rangle\langle g| D(\beta_g). \quad (4.32)$$

This transformation is the equivalent of an unconditioned displacement of the coherent state back to the vacuum, and is often referred to as the *polaron transformation*. Under the polaron transformation, one can straightforwardly trace over the cavity degrees of freedom, yielding a reduced qubit master equation

$$\begin{aligned}\frac{d\rho_q}{dt} &= -i\frac{\tilde{\omega}^q}{2} [\hat{\sigma}^Z, \rho_q(t)] + \Gamma_1 \mathcal{D} [\hat{\sigma}^-] \rho_q(t) + \frac{\Gamma_\phi + \Gamma_d}{2} \mathcal{D} [\hat{\sigma}^Z] \rho_q(t) \\ &= \mathcal{L}_q \rho_q(t)\end{aligned}\quad (4.33)$$

Here, $\rho_q(t) = \text{Tr}_c\{\rho(t)\}$ is the reduced qubit density matrix traced over the cavity degrees of freedom, $\tilde{\omega}^q$ is the ac Stark-shifted qubit frequency, and Γ_d is a measurement-induced dephasing rate. These are given by

$$\tilde{\omega}^q = \omega^q + 2\chi \text{Re}\{\beta_g\beta_e^*\} \quad (4.34)$$

$$\Gamma_d = 2\chi \text{Im}\{\beta_g\beta_e^*\} = \frac{\kappa}{2} |\beta_g - \beta_e|^2 \quad (4.35)$$

Thus, we have derived the unconditioned effects of the measurement drive on the qubit: the qubit frequency shifts, and an initial coherent superposition of $|g\rangle$ and $|e\rangle$ dephases at an additional rate Γ_d . The additional dephasing is caused by the fundamental uncertainty in the coherent pointer state, which provides the fluctuations that generate a stochastic back-action on the qubit. In the unconditioned case, we average over these fluctuations, leading to an overall dephasing.

4.3.4 Dispersive measurement: Bayesian approach

Now that we understand the unconditioned interaction between the qubit and the cavity drive, we can consider a measurement process that monitors the output of the cavity mode. As in Chapter 2, we can apply either a phenomenological Bayesian approach, or a more fundamental stochastic master equation. We will begin here with the Bayesian approach, outlined by Korotkov [138].

Suppose we monitor the \hat{Q} quadrature of the light, which in Figure 4.5 contains the qubit state information. We expect the instantaneous homodyne measurement voltage $V_Q(t)$ to be proportional to

$$V_Q(t) = \frac{\bar{V}_e - \bar{V}_g}{2} \langle \hat{\sigma}^Z \rangle_t + \xi(t) \quad (4.36)$$

where the spectral density of the fluctuating $\xi(t)$ is related to the photon shot noise and \bar{V}_i is the mean value of \hat{V} if the qubit is prepared in state i . Here we have introduced the conditional expectation value $\langle \hat{\sigma}^Z \rangle_t$, which denotes the updated expectation value of $\hat{\sigma}^Z$ given the measurement record up until time t . The Markovian approximation and the QND nature of the measurement allow us to assess this expectation value using the mean integrated signal,

$$\bar{V}_Q(t) = \frac{1}{t} \int_0^t V_Q(t') dt'. \quad (4.37)$$

In other words, we can update our estimate of the density matrix without regard to the specific path of the instantaneous $V_Q(t)$, but rather by considering only the accumulated signal as of time t . The conditional probability for the outcome \bar{V}_Q given the qubit eigenstate $|i\rangle$ is given by the Gaussian function

$$p_i(\bar{V}_Q) = \frac{1}{\sqrt{2\pi}\sigma} e^{(\bar{V}_Q - \bar{V}_i)^2/2\sigma^2}. \quad (4.38)$$

If we choose $\omega^d = \omega^c$ and operate in the small-angle limit appropriate for weak measurements, we can approximate $\bar{V}_g = (2\chi/\kappa)\sqrt{n}$ and $\bar{V}_e = -\bar{V}_g \equiv -\bar{V}$; we now need only determine the variance σ^2 . Recalling that $\Delta\hat{I}\Delta\hat{Q} \geq 1/4$, and that in a coherent state the fluctuations are symmetric in the two quadratures, we can denote the single-quadrature variance as $\sigma_0^2 = 1/4$. As we integrate the signal, the variance decreases as $\sigma^2(t) = \sigma_0^2/(\eta\kappa t)$: information leaks from the cavity at rate κ , with a total efficiency η , which is related to the collection efficiency η_{coll} by $\eta = \frac{\kappa^{\text{out}}}{\kappa}\eta_{\text{coll}}$. The SNR of the measurement is thus given by

$$\begin{aligned} \text{SNR}^2 \equiv \mathcal{S}(t) &= \left(\frac{|\bar{Q}_g - \bar{Q}_e|}{\sigma(t)} \right)^2 \\ &= \frac{64\chi^2 n \eta t}{\kappa} \end{aligned} \quad (4.39)$$

Given the nondimensional measurement strength $\mathcal{S}(t)$, we can now calculate the conditional probabilities in Equation (4.38), and can perform the Bayesian update as outlined in Section

2.2. Because the measurement is QND, we can integrate the signal continuously and perform a Bayesian update at each timestep in order to reconstruct the full quantum trajectory. The measurement-induced evolution in the qubit state is given by

$$\langle \hat{\sigma}^Z \rangle(t, \bar{V}_Q) = \tanh \left[\bar{V}_Q \left(\frac{S^2(t)}{4\bar{V}} \right) \right] \quad (4.40)$$

$$\langle \hat{\sigma}^X \rangle(t, \bar{V}_Q) = \sqrt{1 - [\langle \hat{\sigma}^Z \rangle(t, \bar{V}_Q)]^2} e^{-\Gamma t} \quad (4.41)$$

$$\Gamma = \frac{1}{T_2^*} + \frac{8\chi^2 \bar{n}}{\kappa} (1 - \eta) \quad (4.42)$$

In the case where the collection efficiency is unity, there is no measurement-induced dephasing and the purity of the density matrix is degraded only by intrinsic dephasing in the qubit. This was the approach used by Murch *et al.* [61] in the first continuous trajectory reconstruction in superconducting qubits.

Notice that we have only considered here the fluctuations in the \hat{Q} quadrature - but as we know, there are additional fluctuations in the \hat{I} quadrature that should contribute to the dynamics. In the small-angle limit, fluctuations in \hat{I} correspond to fluctuations in the amplitude $|\beta|$, which Eq. (4.34) tells us causes a Stark-shift of the qubit frequency and therefore causes a stochastic accumulation of phase between $|g\rangle$ and $|e\rangle$. However, if we use a nearly quantum-limited parametric amplifier that is sensitive to only one quadrature (Section 4.4), the fluctuations in the \hat{I} quadrature are effectively “erased”, and therefore do not contribute to the dynamics of the system. We will see in Section 4.4 how such an erasure is accomplished. If instead we use a phase-preserving amplifier, which amplifies both quadratures of the light, we will need to record both V_Q and V_I , using V_Q to update the projection onto $\hat{\sigma}^Z$ and V_I to update the azimuthal phase on the Bloch sphere. For a detailed description of quantum noise and amplification, see Ref. [75].

4.3.5 Dispersive measurement: Master equation approach

While the Bayesian approach is powerful in its simplicity, it is also useful to understand quantum trajectories in cQED using the master equation approach. Let us therefore return to the master equation formalism of Section 4.3.3, and now add the conditional dynamics that arise from monitoring the cavity decay channel. Again, we will use homodyne detection to measure the \hat{Q} quadrature of the propagating field. The measurement signal in this case can be represented by [136, 139]

$$V_Q(t) = \sqrt{\kappa\eta} \langle i\hat{a} - i\hat{a}^\dagger \rangle_t + \xi(t) = 2\sqrt{\kappa\eta} \langle \hat{Q} \rangle_t + \xi(t), \quad (4.43)$$

where $\xi(t)$ again represents a Gaussian approximation for the photon shot noise and $\langle \hat{Q} \rangle_t$ represents the expectation value of \hat{Q} given the continuously updated estimate of the density matrix. Note the difference between this equation and Eq. 4.36: here, the deterministic

component of the signal is related directly to the observed field quadrature, where in Eq. 4.36 the deterministic component is scaled phenomenologically to the expected voltages given the two qubit states. The Bayesian approach in effect skips the intermediate step of deriving the transformation between the field quadrature signal and the qubit state; in the SME formalism we must explicitly derive that scaling.

Given the stochastic quadrature signal, we can update the unconditioned master equation Eq. (4.29) to include a measurement back-action term:

$$\begin{aligned}\frac{d\rho}{dt} &= \mathcal{L}_{\text{tot}}\rho + \xi(t)\sqrt{\kappa\eta}\mathcal{H}\left[\hat{Q}\right]\rho \\ &= \mathcal{L}_{\text{tot}}\rho + \xi(t)\sqrt{\kappa\eta}\mathcal{H}\left[i\hat{a}\right]\rho\end{aligned}\quad (4.44)$$

Since $\frac{d\rho}{dt}$ now depends on a stochastic term, we consider ρ to now be a *conditioned* density matrix. The stochastic master equation contains a measurement superoperator defined in Chapter 2 corresponding to monitoring photon leakage from the cavity. Just as in Section 4.3.3, we can apply the unitary transformation in Eq. (4.32) which, if all the qubit state information is contained in the Q -quadrature, yields³

$$\frac{d\rho}{dt} = \mathcal{L}_q\rho_q(t) + \xi(t)\sqrt{\eta\Gamma_m}\mathcal{H}\left[\hat{\sigma}^Z\right]\rho_q \quad (4.45a)$$

$$\Gamma_m = \frac{\kappa}{4}|\beta_g - \beta_e|^2 = \Gamma_d/2 \quad (4.45b)$$

Ignoring intrinsic qubit decay, the full conditioned qubit state evolution is thus given by

$$\frac{d\rho_q}{dt} = -i\frac{\tilde{\omega}^q}{2}\left[\hat{\sigma}^Z, \rho_q(t)\right] + \frac{\Gamma_d}{2}\mathcal{D}\left[\hat{\sigma}^Z\right]\rho_q(t) + \sqrt{\eta\Gamma_m}\mathcal{H}\left[\hat{\sigma}^Z\right]\rho_q\xi(t). \quad (4.46)$$

Thus, we can correlate the instantaneous homodyne measurement current $V_Q(t)$ with a stochastic evolution of the qubit state. However, notice that the measurement rate saturates to half the dephasing rate as defined in Eq. (4.35), leading to a maximum effective quantum efficiency $\eta_{\text{eff}} = \eta\Gamma_m/\Gamma_d$ of 1/2. This is because half of the fluctuations to which the qubit is exposed are in the unmeasured \hat{I} quadrature. The formalism developed in Ref. [118] implicitly assumes the use of a phase-preserving amplifier, after which only one quadrature is recorded; half of the fluctuations are therefore lost, and half of the qubit state evolution is untraceable and manifests as dissipation.

4.4 Parametric Amplification

In both the Bayesian approach and the SME formalism, continuous state tracking depends critically on near-unity quantum efficiency. If $\eta \ll 1$, the conditioned dynamics are essentially indistinguishable from the pure measurement-induced dephasing seen in Section 4.3.3;

³ Observant readers will note a difference between Eq. (4.45b) and the equivalent in Ref. [118]. This is due to a difference in the definition of the measurement operator. The translation is given by $\mathcal{H}[\hat{c}]\rho = 2\mathcal{M}[\hat{c}]\rho$, where $\mathcal{M}[\hat{c}]\rho$ is the measurement operator used in the original source.

only when the quantum efficiency is high can we hope to perform continuous state tracking. Efficient measurement requires amplifying the signal, whose quantum fluctuations give it an effective temperature $T_Q = \hbar\omega^d/2k_b \approx 170$ mK, enough to overcome room-temperature thermal fluctuations that are five orders of magnitude larger. This amplification must be accomplished without adding significant uncorrelated noise in order to reconstruct the quantum state with high fidelity. Needless to say this task is technically challenging - but it can be accomplished using an amplifier circuit that is quite similar to the transmon circuit itself.

4.4.1 The lumped Josephson parametric amplifier

The amplifier we use in this dissertation is the lumped Josephson parametric amplifier (LJPA) [120, 140, 141]. It consists of a pair of Josephson junctions with relatively large critical current (several μ A) fabricated in a parallel loop, shunted by a correspondingly large capacitance (several pF) such that the zero-flux resonant frequency is near the measurement frequency (near 8 GHz) and can be tuned down to resonance if desired. The large shunt capacitance means that the anharmonicity is relatively small such that when the intra-resonator photon number is low, the LJPA acts as a linear resonator. However, when the amplifier is biased with a large pump tone, its resonance bends to lower frequencies due to the negative anharmonicity of the circuit, as in Figure 4.6a. When the bias exceeds a critical power, the resonance bifurcates. The parametric amplification regime requires a bias pump power just below the bifurcation point, such that the resonant frequency of the resonator is maximally dependent on the power. We combine the pump tone with our small experimental signal and reflect the total field off of the LJPA. The phase response of the reflected field (Figure 4.6b) provides the amplification we desire.

When the amplifier is biased with a large pump, its weak nonlinearity generates a $\chi^{(3)}$ dispersive medium that is able to do four-wave mixing. Specifically, a coherent pump drive at ω^p modulates the effective Josephson inductance, and thus the resonant frequency, of the circuit. This modulation, which occurs at $2\omega^p$, can be accomplished either by the combination of two degenerate pump photons, or of two detuned photons at $\omega^p \pm \omega_{IF}$. Conservation of energy requires that the two photons generated by the four-wave mixing process, labelled the signal and idler photons, satisfy $2\omega^p = \omega^s + \omega^i$. In the case where $\omega^s = \omega^i = \omega^p$, the amplifier performs doubly-degenerate four-wave mixing. This is the regime in which we will operate. Typical LJPA's operate with > 20 dB of gain over a bandwidth of 10-50 MHz; recent advances in impedance matching and microwave engineering [142, 143] enable similar gain over 500-700 MHz of bandwidth. There are other useful Josephson junction-based amplifier designs, notably including the Josephson parametric converter (JPC) [144–147] which is another resonant superconducting amplifier that performs three-wave mixing. Recently, a nearly quantum-limited Josephson traveling-wave parametric amplifier (TWPA) was demonstrated [148], which exhibits 20 dB of gain over several GHz of bandwidth. For a full derivation of the JPA amplification and performance properties, see Refs. [120] and [140].

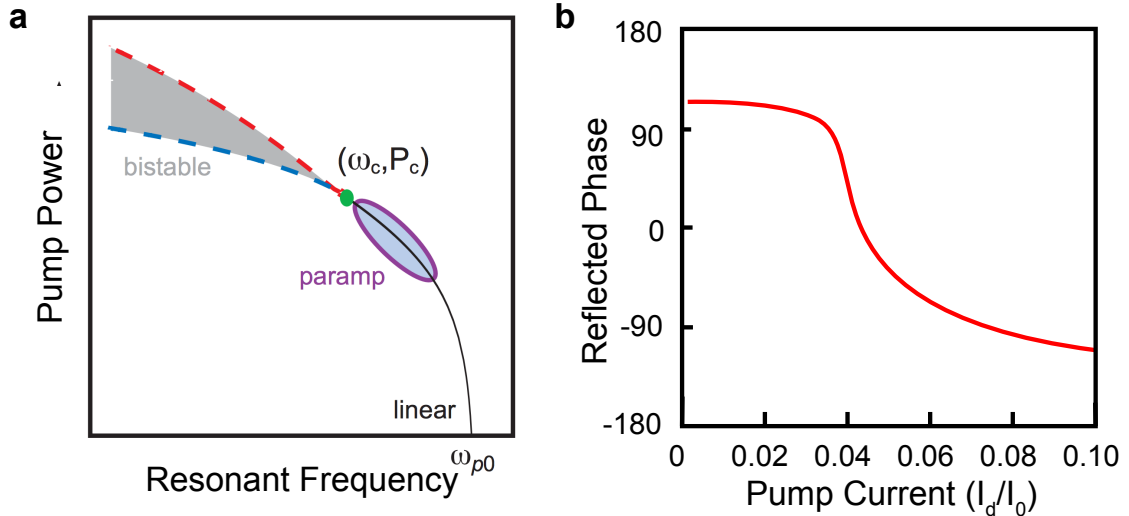


Figure 4.6: LJPA characteristics. (a) Resonant frequency: as pump power increases, the resonant frequency of the amplifier (ω_{p0}) bends downward, eventually bifurcating after a critical point (ω_c, P_c) . (b) Phase response: as injected power increases, the reflected phase changes accordingly. Adapted from Ref. [120].

We briefly note that 20 dB of gain is not yet sufficient to overcome room-temperature fluctuations. In order to provide the necessary additional amplification, we follow the LJPA with a low-noise HEMT ($\eta \approx 1/10$) at the 4 K stage of the dilution refrigerator, which provides 30 dB of amplification, and utilize additional room-temperature amplifiers. However, the noise temperature of the full amplification chain is dominated by the quantum efficiency of the lowest stage, provided that its amplification is large enough [120]. Therefore, the quantum efficiency of the overall measurement chain depends critically on the quality of the first cryogenic amplifier.

4.4.2 Phase-sensitive amplification

One of the features that makes the LJPA an attractive choice in comparison to the JPC and the TWPA is its ability to perform phase-sensitive amplification, amplifying a single quadrature of light while de-amplifying, or squeezing, the other. Phase sensitive amplification occurs when ω^i and ω^s are degenerate with ω^p , such that the input signal adds coherently with the pump tone. Figure 4.7 illustrates the phase sensitivity of the amplifier at degeneracy. The component of the measurement signal that is in-phase (or 180° out of phase) with the pump increases (or decreases) the intra-cavity power directly by vector addition, causing an amplified phase shift in the reflected field. The components of the signal that are $\pm 90^\circ$ out

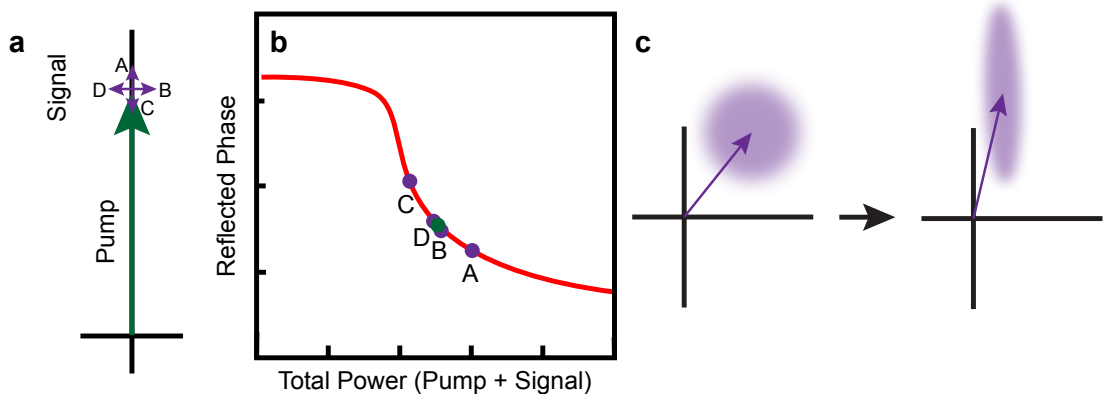


Figure 4.7: Schematic demonstration of phase-sensitive amplification. a) A strong pump tone combines with a much weaker readout signal via vector addition. b) If the signal is directly parallel or antiparallel to the pump tone (A, C), the total power in the nonlinear resonator changes maximally, and the phase response is maximized. Weak signals that are out of phase with the pump (B, D) do not affect the total power to first order; therefore, the out-of-phase signal is reduced. c) After passing through an LJPA operating in phase-sensitive mode, a coherent state is reflected as a squeezed state.

of phase with the drive, however, only cause a change in the intra-cavity power at second order, since the pump tone is much larger than the signal. In this case, the out-of-quadrature components of the signal are actually de-amplified, or squeezed. If the amplification and squeezing are sufficiently large, the LJPA essentially “erases” the fluctuations in the out-of-phase quadrature, such that they no longer cause a back-action on the qubit state. This is precisely the situation we described in Section 4.3.4, which allows us to effectively perform a single-quadrature measurement while ignoring the back-action caused by fluctuations in the complementary quadrature.

The squeezing performed in phase-sensitive amplification additionally enables noiseless amplification. If the gain of the amplifier is given by G and the input signal represented by the bosonic modes \hat{a} , then we can represent the output of the amplifier as \hat{b} , where

$$\begin{aligned}\hat{b} &= \sqrt{G}\hat{a}; \\ \hat{b}^\dagger &= \frac{1}{\sqrt{G}}\hat{a}^\dagger.\end{aligned}\tag{4.47}$$

It is straightforward to show that $[\hat{b}, \hat{b}^\dagger] = 1$, such that the outgoing amplified field need contain no additional fluctuations. This noiseless amplification is useful for efficient readout, and is critical for the reconstruction of quantum trajectories. In contrast, phase-preserving

amplification (in which both quadratures are equally amplified, for example by an LJPA operating off of degeneracy or by a TWPA) requires the addition of, at minimum, one photon of uncorrelated noise in order to preserve the unitary commutation of \hat{b} and \hat{b}^\dagger . This additional noise reduces the rate at which a projective measurement can be performed, and limits the ability to reliably reconstruct a quantum trajectory (since at minimum half of the fluctuations observed by the experimenter are uncorrelated with the back-action on the qubit). For an intensive treatment of quantum noise and parametric amplification, see Ref. [75].

4.5 Summary: The Superconducting Qubit Toolbox

We now have a basic understanding of all the elements required to perform quantum experiments using superconducting circuits. The superconducting Josephson junction creates a nonlinear inductance that, when embedded in an LC circuit, generates a nonlinear resonator with unequal spacing between neighboring energy levels (Section 4.1). The capacitive element in the qubit LC circuit can be designed with a significant electric dipole moment, allowing the qubit to couple strongly to the electromagnetic field modes inside a resonator via the Jaynes-Cummings Hamiltonian (Section 4.2). When the qubit and cavity are far-detuned from one another, this interaction enables us to use a displaced coherent state inside the cavity as a pointer state for the qubit; by monitoring the reflected or transmitted phase of a measurement signal passing through the cavity, we can continuously infer the qubit state (Section 4.3). The qubit state inference can be done continuously and with high fidelity by employing a nearly-quantum limited amplifier, in this case an LJPA, which squeezes fluctuations in the undesired quadrature and amplifies the quadrature containing qubit information (Section 4.4). Thus, we have all the tools we need to create, manipulate, and measure coherent quantum circuits.

Chapter 5

Remote Measurement-Induced Entanglement

I cannot seriously believe in [quantum mechanics] because the theory cannot be reconciled with the idea that physics should represent a reality in time and space, free from spooky actions at a distance.

Albert Einstein, *Letter to Max Born, 1947*

We now proceed to investigate a first practical use of dissipation in our superconducting cQED architecture: we use a carefully-tailored measurement to generate entanglement between qubits that are separated from one another by many wavelengths, have no local coupling, and are therefore functionally remote. Entanglement schemes for superconducting qubits have traditionally relied on direct qubit-qubit coupling [26, 27, 39, 149–151], cavity-mediated interactions [28–30, 152–154], or local photon-mediated interactions [155]. However, the creation of a quantum network requires the distribution of coherent information across macroscopic distances. Measurement-induced entanglement (MIE) [156–161] is a particularly important resource in these spatially-separated quantum systems, for which no local interactions and therefore no direct methods of creating entanglement exist. Such remote entanglement has been demonstrated using optical photons in several atomic systems [162–164] and nitrogen vacancy centers [88, 165], but has remained elusive for superconducting qubits, which operate in the microwave regime.

In this chapter, we demonstrate measurement-induced entanglement between two superconducting qubits, each dispersively coupled to a separate cavity for readout and separated by 1.3 meters of ordinary coaxial cable, by engineering a continuous measurement for which one of the three outcomes is a Bell state [166]. This measurement constitutes a *half-parity measurement*, in which the odd-parity states ($|ge\rangle$ and $|eg\rangle$) are indistinguishable from one another, but the even-parity states ($|gg\rangle$ and $|ee\rangle$) are distinguishable both from the odd-parity manifold *and* from each other. The use of continuous measurements allows us to access the ensemble-averaged *dynamics* of entanglement generation, which are well-described by a

statistical model and by a full master-equation treatment. As we will see in Chapter 6, our measurement efficiency is sufficiently high to resolve the individual quantum trajectories in the ensemble, thus enabling the observation of the stochastic evolution of a joint two-qubit state under measurement. This functionality sheds new light on the fundamental interplay between entanglement, measurement, and decoherence in a quantum network. This work was originally published as Ref. [167].

5.1 Historical Perspective

Using a continuous measurement to generate entanglement remotely represents one of the chief innovations in our approach to remote measurement-induced entanglement. To understand why this development is important, we first must understand previous MIE schemes, which rely on photon-counting and post-selection, necessarily reducing the success rate of the protocol. For quantum architectures building upon transitions at optical frequencies [88, 162, 164, 165], MIE has typically been achieved by relying on the correlated detection of photons at the output of a beam-splitter [168] to herald an entangled state. While powerful, this measurement protocol is binary and practically instantaneous, and allows no insight into the dynamical processes underlying the generation of the entangled state. In solid state systems with transitions in the microwave, there has been tremendous interest in *continuously* generating bipartite [156, 158, 169–171] and multi-partite [160, 161, 172] entangled states, using weak measurements that slowly interact with the qubits, in such a way that enables the resolution of the dynamical aspects of the entangling backaction. Such a measurement was demonstrated in a local system (two qubits housed within the same cavity) concurrent with this work [154]; our work represents the first use of continuous measurement to generate entanglement between quantum objects separated by many wavelengths of their characteristic frequencies. The use of weak measurements additionally opens the door to feedback stabilization [139, 173–176], bringing the protocol from a probabilistic to a deterministic method of generating entanglement [171, 177, 178].

A second critical difference between photon detection and continuous measurement for the purpose of generating entanglement is the effect of losses. Photon detection-based experiments typically exploit the Hong-Ou-Mandel Effect [168], which states that identical photons simultaneously incident on two input arms of a 50/50 beam splitter will emerge on the same output arm. One can understand this trivially by considering the time-reversed case: two photons simultaneously arriving on one arm of such a beam splitter must emerge with equal amplitude on both arms. Equivalently, one can coherently add the four transmission and reflection possibilities as shown in Figure 5.1; the negative signs come from reflection from the bottom of the beam splitter. If the incoming photons are indistinguishable, the second and third amplitudes cancel, leading to photon bunching.

In a photon detection MIE experiment, the two qubits are each prepared in an x-polarized state $|\psi\rangle = \frac{|g\rangle + |e\rangle}{\sqrt{2}}$, after which a Raman scattering mechanism is used to stimulate emission of a photon into a traveling mode conditioned on the qubit in state $|e\rangle$ such that the total system

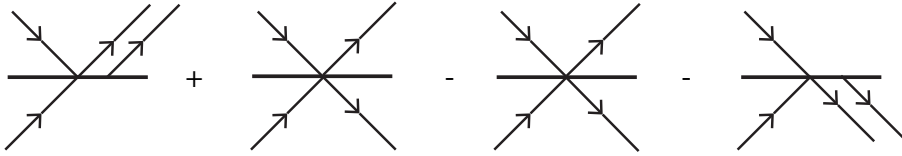


Figure 5.1: An illustration of the Hong-Ou-Mandel effect which is typically used for measurement-induced entanglement in photon-counting experiments. Two photons incident on opposite arms of the beam splitter can emerge in four possible arrangements. Due to an overall phase shift of π caused by reflection from the bottom of the beam splitter, the second and third possibilities interfere destructively, leading to photon bunching.

state becomes $\frac{1}{2} [|g, 0\rangle + |e, 1\rangle]_A \otimes [|g, 0\rangle + |e, 1\rangle]_B$. The photons act as “flying qubits”: they interfere with one another at the beam splitter, and are then counted at photon detectors coupled to both output modes of the beam splitter.

If the transmission and detection efficiencies are both unity such that all photons arrive at the beam splitter and are accurately counted at the detectors, there are three possible outcomes. A measurement of zero photons at either node projects the qubits into the state $|gg\rangle$; two photons detected at either node projects into $|ee\rangle$. However, a single photon detected at either node does not provide which-path information: the photon could have been emitted from either sample, and therefore from the standpoint of the measurement has come simultaneously from *both*. This projects the system into the degenerate odd-parity subspace, leading to an entangled state $\frac{|ge\rangle \pm e^{i\phi}|eg\rangle}{\sqrt{2}}$, where ϕ is determined by the path length and the \pm phase is heralded by the arm of the detector on which the photon emerged. Thus, a single photon detection event can be said to “herald” an entangled state.

The chief effect of transmission loss in such a system is clearly to reduce the success rate of the experiment. For experimental iterations in which a single photon is emitted, but is absorbed by fiberoptic cable before reaching the photodetector, from the standpoint of the experimentalist there was never a photon emitted at all. This iteration is excluded from the heralded ensemble, although it would have otherwise generated an entangled state (and if the photon dissipated after the beam-splitter, in fact *did* generate entanglement). Thus, the entanglement generation rate is diminished. If the qubits are in $|ee\rangle$ and two photons are generated, but one is absorbed and one detected, there is the possibility of an error: the experimentalist may include this experiment in the heralded ensemble, leading to an excess of $|ee\rangle$ population and degrading the quality of the ensemble. To protect against this decoherence mode, however, one can perform bit flips on the two qubits and then repeat the experiment. If the qubits were in $|ee\rangle$, the bit flip takes the system to $|gg\rangle$ and no photons will be detected; if a single photon is detected again, the entanglement is confirmed. If the fiberoptic cable and the detectors are reasonably high in transmission and detection efficiency, the odds of a double absorption error are vanishingly small. Thus, the chief effect

of inefficiency in a photon counting experiment is to diminish the heralding rate; the ensemble of measurements that pass the herald will be reasonably pure.

For a continuous dispersive measurement using a coherent state, however, the effects of losses are different. Recall that coherent states are eigenstates of the annihilation operator \hat{a} : even in the case of a photon scattering event, a measurement signal will reach the homodyne detector, and the experimentalist will be able to make an estimate of whether or not the outcome is consistent with an entangled state. The advantage here is that the entanglement generation rate is preserved, and can be orders of magnitude larger than the rate in photon counting case. However, any photons absorbed before the detector will carry away with it information about the qubits, and unlike in the photon counting case we cannot post-select away the effects of spurious photon absorption. As we will see, photon scattering on the path between the two cavities leads to an unavoidable measurement-induced dephasing of the entangled ensemble. This effect provides us an opportunity to study in detail the interplay between measurement and dissipation in a quantum system.

5.2 Design of an Entangling Continuous Measurement

Our experimental apparatus consists of two superconducting transmon qubits placed in spatially separated copper waveguide cavities (3D transmon architecture) [115]. Each cavity is wound with a superconducting bias coil to enable tuning of the qubit frequency. A weakly coupled port is used for transmission measurements and single qubit control, and a strongly coupled port enables qubit state readout. The strongly coupled ports of the two cavities are connected via two microwave circulators and 1.3 meters of coaxial cable to enable directional transfer of information from Cavity 1 to Cavity 2 (Figure 5.2).

5.2.1 Joint dispersive measurement

A joint qubit state measurement can be performed by sequentially driving the cavities in reflection with a near-resonant microwave tone at frequency ω^m that can be described semi-classically as a complex coherent drive A_d , as in Section 4.3.1. For clarity, we use $A(t)$ and $B(t)$ to represent the intracavity fields in Cavity 1 and Cavity 2, respectively, and A_{out} , B_{out} to represent the propagating fields traveling *from* the respective cavities. For a single qubit in an eigenstate, measured in reflection, the output state is given by $A_{\text{out}} = r^\pm A_d$, where

$$r^\pm = \frac{\kappa - 2i(\omega^c - \omega^m \mp \chi)}{\kappa + 2i(\omega^c - \omega^m \mp \chi)}, \quad (5.1)$$

and the signifier (+/-) represents the single qubit state $|g\rangle$ ($|e\rangle$). Here, ω^c is the bare cavity frequency; κ is the total cavity decay rate; and χ is the dispersive shift due to the interaction between the qubit and the cavity. The measurement tone acquires a qubit state-dependent phase shift $\phi^\pm = \text{Arg}\{A_{\text{out}}^\pm\}$. For the following analysis it is convenient to define the average and relative phase shifts, $\delta = \frac{1}{2}(\phi^+ + \phi^-)$ and $\Delta\phi = \phi^+ - \phi^-$, respectively (See Figure 5.2.1a).

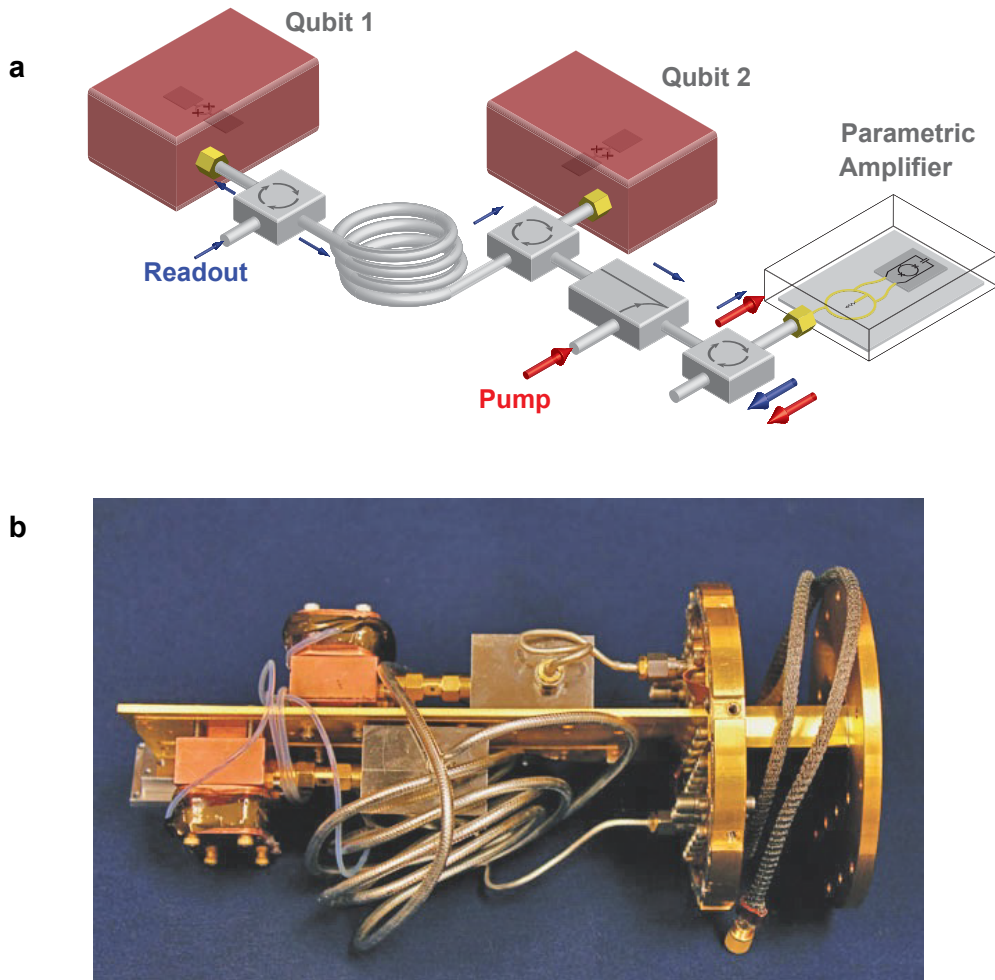


Figure 5.2: Simplified representation of the experimental setup. Panel (a) displays a schematic representation of the measurement path as an input signal is reflected off of a first cavity; transmitted through a 1.3 m delay cable; reflected off of a second cavity; and then routed to a parametric amplifier. Panel (b) is a picture of the base-temperature setup, showing the two copper cavities, two circulators, and the coiled delay cable.

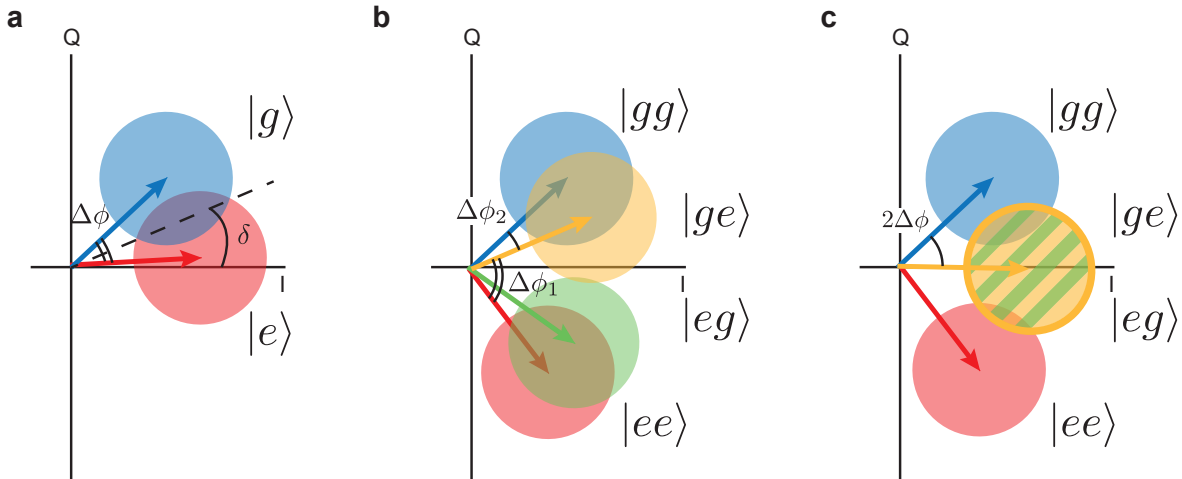


Figure 5.3: Schematic representation of the joint qubit measurement. Panel (a) displays the output of a dispersive measurement at a single cavity, defining the angles $\Delta\phi$ and δ . Panel (b) shows the joint dispersive measurement in the general case $\Delta\phi_1 \neq \Delta\phi_2$: all four states are distinguishable. In Panel (c), we see that a half-parity measurement is accomplished when $\Delta\phi_1 = \Delta\phi_2$.

For a sequential reflective measurement of two qubits, the output coherent state becomes $B_{\text{out}} = \sqrt{\eta_{\text{loss}}} r_1^\pm r_2^\pm A_d$, where η_{loss} represents the efficiency of power transfer between the two cavities. In the general case, $\Delta\phi_1 \neq \Delta\phi_2$ and the phase shifts corresponding to the four basis states $|gg\rangle$, $|ge\rangle$, $|eg\rangle$ and $|ee\rangle$ are all distinct (Figure 5.2.1b); the associated measurement decoheres any quantum superposition of states and projects the system into one of the four basis states. However, if we carefully engineer the cavities and the dispersive coupling, there exists ω^m such that $\Delta\phi_1 = \Delta\phi_2$. In this situation, the phase shifts associated with states $|ge\rangle$ and $|eg\rangle$ are identical and equal to $\delta_1 + \delta_2$; the measurement therefore cannot decohere a quantum superposition of $|01\rangle$ and $|10\rangle$ (Figure 5.2.1c). Because the states $|ge\rangle$ and $|eg\rangle$ are odd eigenvalues of the parity operator $\hat{\sigma}^{ZZ} = \hat{\sigma}_1^Z \otimes \hat{\sigma}_2^Z$, this measurement is referred to as a half-parity measurement. Equivalently, the odd-parity states span one of the three eigenspaces of the half-parity operator $\hat{\sigma}_1^Z + \hat{\sigma}_2^Z$.

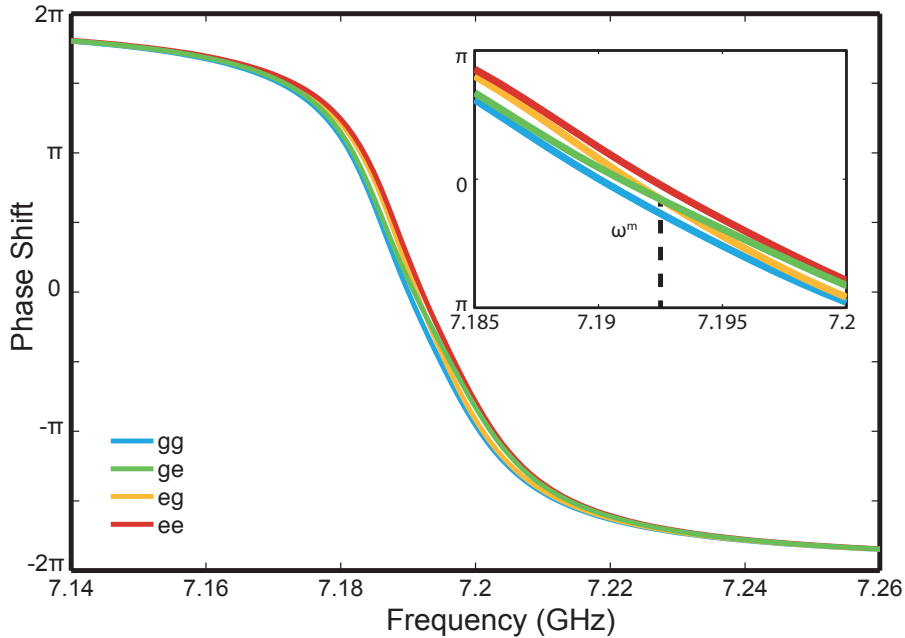


Figure 5.4: Double-reflection phase shift calculated for the four prepared states $|gg\rangle$, $|ge\rangle$, $|eg\rangle$, and $|ee\rangle$. The reflection curves pass through a 4π , indicating reflection from two sequential cavities. The inset shows the crossing between the reflected phases for $|ge\rangle$ and $|eg\rangle$ at $\omega^m = 7.19326$ GHz.

5.2.2 Tuning the entangling measurement

How, then, do we make such a half-parity measurement? If we were able to engineer the qubit and cavity parameters ω^c , χ , and κ to be identical, the condition $\Delta\phi_1 = \Delta\phi_2$ would be met automatically. However, even careful design and machining only allows us to match these parameters within a 5-10% margin of error; we require an *in-situ* tuning mechanism to allow us to finely tune the cavity phase shifts. Allowing for qubit and cavity parameters to vary between the cavity, we find

$$B_{\text{out}} = \frac{\frac{\kappa_1}{2} - i(\omega_1^c - \omega^m \mp \chi_1)}{\frac{\kappa_1}{2} + i(\omega_1^c - \omega^m \mp \chi_1)} \times \frac{\frac{\kappa_2}{2} - i(\omega_2^c - \omega^m \mp \chi_2)}{\frac{\kappa_2}{2} + i(\omega_2^c - \omega^m \mp \chi_2)} \times \sqrt{\eta_{\text{loss}}} A_d \quad (5.2)$$

We have assumed that $Q_{\text{int}} \gg Q_{\text{ext}}$, such that we can neglect internal losses. This leads to four distinct cavity resonance curves conditioned on the qubits in states $|gg\rangle$, $|ge\rangle$, $|eg\rangle$, and $|ee\rangle$ (Figure 5.4). Solving for the frequency at which $B_{\text{out}}^{(ge)} = B_{\text{out}}^{(eg)}$ results in a quadratic equation in ω^m that has real solutions if the following inequality is satisfied:

$$(\omega_1^c - \omega_2^c)^2 \geq \left(\frac{1}{4} \frac{\kappa_1 \kappa_2}{\chi_1 \chi_2} + 1 \right) \left[(\chi_1 - \chi_2)^2 - \frac{\chi_1 \chi_2}{\kappa_1 \kappa_2} (\kappa_1 - \kappa_2)^2 \right]. \quad (5.3)$$

Careful manufacture of qubits and cavities enables us to match κ_1 and κ_2 within 2-3 MHz, and χ_1 and χ_2 within several hundred kHz. As a result, this condition is fairly straightforward to meet by adjusting the cavity frequencies such that $|\omega_1^c - \omega_2^c| \sim \kappa$. It is possible to theoretically calculate the correct ω^m ; in practice, we sequentially prepare the computational states $|gg\rangle, |ge\rangle, |eg\rangle$, and $|ee\rangle$, and adjust ω^m until the single-shot Gaussian measurement histograms for the $|ge\rangle$ and $|eg\rangle$ states completely overlap.

5.2.3 Verification of the half-parity measurement

Before studying the dynamics of the measurement-induced entanglement process, we first would like to verify that the measurement does not distinguish between $|ge\rangle$ and $|eg\rangle$. To do so, we sequentially prepare the states $|gg\rangle, |ge\rangle, |eg\rangle$, and $|ee\rangle$, and integrate the measurement signal for a variable time t . Repeating this process several thousand time yields measurement histograms for each of the four states (Figure 5.5). For short integration time, the weak, continuous nature of the measurement is evident: the four histograms are all indistinguishable from one another. As t increases, the measurement Gaussians begin to separate and we see that the measurements corresponding to $|gg\rangle$ and $|ee\rangle$ become distinguishable, but the $|ge\rangle$ and $|eg\rangle$ histograms are identical. At longer t , the histograms further separate, and we begin to see the effects of qubit decay (manifesting as the shoulder on the $|ee\rangle$ histogram). The near-perfect overlap between the $|ge\rangle$ and $|eg\rangle$ histograms provides a preliminary confirmation that the measurement should be able to perform an entangling projection.

5.3 Bayesian Theory of the Entangling Measurement

Here, we briefly describe a simplified phenomenological method of understanding and predicting the back-action of this half-parity measurement using a Bayesian approach. For a more rigorous demonstration using equivalent stochastic master equation method, see Ref. [179] and the supplement to Ref. [167]. As we will see in Section 5.5, despite its phenomenological nature this theory reproduces the experimental data quantitatively, with some potential deviations at short timescales that are accounted for by the full stochastic master equation approach.

Writing the two qubit density matrix as

$$\rho = \sum_{ijkl} \rho_{ij,kl} |ij\rangle \langle kl|, \quad (5.4)$$

we can estimate concurrence [107] as described in Section 3.3 using the simplified formula [110]

$$\mathcal{C} \approx \max(0, |\rho_{ge,eg}| - \sqrt{\rho_{gg,gg}\rho_{ee,ee}}) \quad (5.5)$$

This formulation implies that for simplicity we can neglect the off-diagonal elements $\rho_{gg,ge}$, $\rho_{gg,eg}$, $\rho_{ee,ge}$, $\rho_{ee,eg}$, and $\rho_{ee,gg}$ (which should be small in the interesting regime).

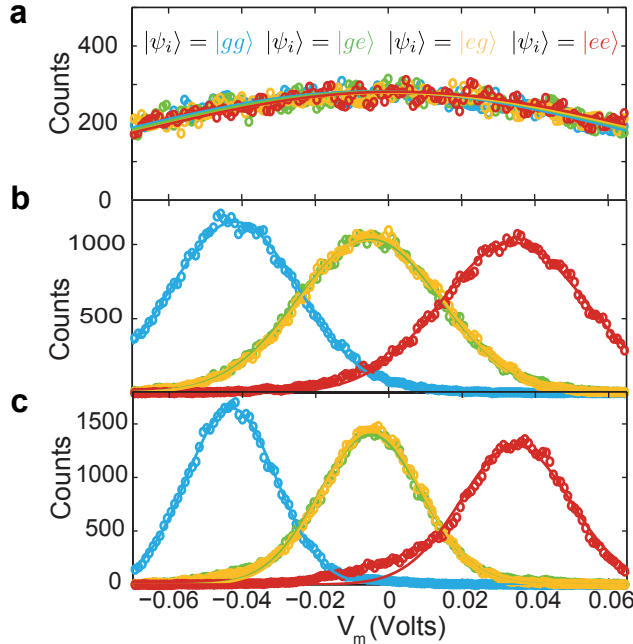


Figure 5.5: Measurement histograms for the four fiducial states, at increasing integration times of (a) $0.010 \mu\text{s}$, (b) $0.650 \mu\text{s}$, and (c) $1.61 \mu\text{s}$. Solid lines represent a Gaussian fit.

To find $\rho_{gg,gg}$, $\rho_{ee,ee}$, and $\rho_{ge,eg}$ after the measurement, we first consider the case without energy relaxation or intrinsic dephasing of the qubits; then the dynamics of the two-qubit state are only due to measurement. For each of four initial fiducial states of the qubits ($|gg\rangle$, $|ge\rangle$, $|eg\rangle$, $|ee\rangle$) it is easy to calculate the evolution of the classical field amplitudes $A(t)$ and $B(t)$ in the first and second resonators,

$$\dot{A} = -\frac{\kappa_1}{2}A - i(\omega_1^c \mp \chi_1 - \omega^m)A + \sqrt{\kappa_{s,1}} A_d(t), \quad (5.6)$$

$$\dot{B} = -\frac{\kappa_2}{2}B - i(\omega_2^c \mp \chi_2 - \omega^m)B + \sqrt{\kappa_{s,2}} \sqrt{\eta_{\text{loss}}} A_{\text{out}}(t), \quad (5.7)$$

Here the rotating frame ($e^{-i\omega^m t}$) is based on the measurement drive, the time for $B(t)$ is shifted by the "flying time" between resonators, and $\kappa_i = \kappa_{s,i} + \kappa_{w,i} + \kappa_{l,i}$ is the total bandwidth of the resonators including the bandwidth due to strongly (κ_s) and weakly (κ_w) coupled ports - see Fig. 5.6 - and to dissipative loss in the cavity (κ_l). The energy decay for the microwave propagation *between* the resonators is described by the efficiency η_{loss} . Notice that in Eqs. (5.6) and (5.7) the resonator field amplitudes A and B are normalized such that $|A|^2$ and $|B|^2$ are equal to the average number of photons in the corresponding coherent

states, while for the propagating field A_d the squared amplitude $|A_d|^2$ is equal to the average number of photons per unit time.

Similar normalization is used for the propagating field

$$A_{\text{out}}(t) = -A_d(t) + \sqrt{\kappa_{s,1}} A(t), \quad (5.8)$$

and the field

$$B_{\text{out}}(t) = -\sqrt{\eta_{\text{loss}}} A_{\text{out}}(t) + \sqrt{\kappa_{s,2}} B(t), \quad (5.9)$$

which goes from the second resonator through the circulator to the amplifier. In the steady-state limit ($\dot{A} = 0$) and for $\kappa_s \gg \kappa_w + \kappa_l$, we recover the expression in Equation 5.1 for the amplification coefficient, and additionally find the photon number population inside Cavity 1:

$$\bar{n}_1^{\pm} = \frac{\kappa_{s,1}}{(\kappa_{s,1}/2)^2 + (\omega_1^c - \omega^m \mp \chi_1)^2} |A_d|^2. \quad (5.10)$$

To produce the entangled state in our experiment, the steady-state fields $B_{\text{out}}^{(ge)}$ and $B_{\text{out}}^{(eg)}$ for the states $|ge\rangle$ and $|eg\rangle$ should be indistinguishable, $B_{\text{out}}^{(ge)} = B_{\text{out}}^{(eg)}$, while they should be sufficiently well distinguishable from the fields $B_{\text{out}}^{(gg)}$ and $B_{\text{out}}^{(ee)}$. For amplification and homodyne measurement of the field quadrature $e^{i\phi}$, the average time-integrated measurement result for the state $|ij\rangle$ is

$$S_{ij} = \frac{1}{t} \int \text{Re} \left\{ B_{\text{out}}^{(ij)}(t') e^{-i\phi} \right\} f_w(t') dt', \quad (5.11)$$

where $f_w(t)$ is the weight function, which we take to be a constant-weight integration with an offset to account for cavity ring-up. The amplifier noise is also accumulated during this time-integration, so that for the two-qubit state $|ij\rangle$ the random measurement result is characterized by the Gaussian distribution with the mean value of S_{ij} and the standard deviation

$$\sigma = \frac{1}{2\sqrt{\eta_{\text{meas}}}} \sqrt{\frac{1}{t} \int f_w^2(t) dt}, \quad (5.12)$$

where η_{meas} is the quantum efficiency of the measurement setup, which includes quantum efficiency of the phase-sensitive amplifier and losses in the circulators and cables. Notice that the noise σ does not depend on the two-qubit state. In our experiment, the homodyne detection phase ϕ is chosen to be perpendicular to the output states for $|ge\rangle$ and $|eg\rangle$, $\phi = \text{Arg} \left\{ B_{\text{out}}^{(ge)} \right\} = \text{Arg} \left\{ B_{\text{out}}^{(eg)} \right\}$.

Because our entangling process is probabilistic and not deterministic, we must post-select only realizations for which the integrated signal falls within a certain range, centered near $(S_{ge} + S_{eg})/2$. The total probability of selection in our model (assuming no energy relaxation of qubits) is then

$$p_{\text{ent}} = \sum_{i,j} \rho_{ij,ij}(0) p_{\text{sel}}(i, j), \quad (5.13)$$

where $\rho(0)$ is the two-qubit density matrix before the measurement and $p_{\text{sel}}(i, j)$ is the selection probability for the initial state $|ij\rangle$. The probability $p_{\text{sel}}(i, j)$ is equal to the integral, within the selection range, of a Gaussian with mean value S_{ij} and standard deviation σ , such as those in Figure 5.5.

Since the two-qubit state evolution is only due to measurement, the diagonal matrix elements of the final density matrix $\rho(t)$ should obey [69] the classical Bayes rule

$$\rho_{ij,ij}(t) = \frac{\rho_{ij,ij}(0) p_{\text{sel}}(i, j)}{p_{\text{ent}}}. \quad (5.14)$$

For the main off-diagonal matrix element $\rho_{ge,eg}(t)$ needed to calculate concurrence, the quantum Bayesian approach [69] cannot be applied rigorously; however, we can modify it phenomenologically by using the following approximation:

$$\begin{aligned} |\rho_{ge,eg}(t)| &= |\rho_{ge,eg}(0)| \frac{\sqrt{\rho_{ge,ge}(t)\rho_{eg,eg}(t)}}{\sqrt{\rho_{ge,ge}(0)\rho_{eg,eg}(0)}} \\ &\times \exp \left[-\frac{1}{2} \int (1 - \eta_{\text{meas}}) \left| B_{\text{out}}^{(ge)}(t) - B_{\text{out}}^{(eg)}(t) \right|^2 dt \right] \\ &\times \exp \left[-\frac{1}{2} \int [(1 - \eta_{\text{loss}}) \kappa_{s,1} + \kappa_{w,1} + \kappa_{l,1}] \left| A^{(ge)}(t) - A^{(eg)}(t) \right|^2 dt \right] \\ &\times \exp \left[-\frac{1}{2} \int (\kappa_{w,2} + \kappa_{l,2}) \left| B^{(ge)} - B^{(eg)} \right|^2 dt \right], \end{aligned} \quad (5.15)$$

where the last three factors describe the dephasing due to potential distinguishability of states $|ge\rangle$ and $|eg\rangle$ in the field B_{out} and "lost" fractions of the fields A and B from the first and second resonators. The form of these dephasing factors directly follows from the overlap between two coherent states $|A_1\rangle$ and $|A_2\rangle$ in a resonator [136]: $|\langle A_1 | A_2 \rangle| = \exp(-|A_1 - A_2|^2/2)$.

The remaining off-diagonal elements can also be calculated by substituting the respective states for (ge) and (eg) . In the analysis to follow, we will neglect these elements for two reasons. First, the diagonal elements $\rho_{gg,gg}$ and $\rho_{ee,ee}$ go to zero as we successfully post-select the entangled subspace, such that the first term in Eq. (5.15) goes to zero. Additionally, the term in which the exponent is proportional to $\left| B_{\text{out}}^{(ge)} - B_{\text{out}}^{(eg)} \right|^2$ is negligible in the odd-parity subspace, but represents significant distinguishability between all other states. Thus, the off-diagonal matrix terms outside the odd-parity subspace are doubly suppressed. For the terms $\rho_{gg,ge}$, $\rho_{gg,eg}$, $\rho_{eg,ee}$, $\rho_{ge,ee}$, and their conjugates, these terms follow straightforwardly from the single-qubit Bayesian formalism developed in Section 4.3.4. The application of this formula to the even-parity coherence factor $\rho_{gg,ee}$ is a phenomenological extension of this theory, just as $\rho_{ge,eg}$ is.

Only the absolute value of $\rho_{ge,eg}(t)$ is needed to calculate the concurrence (5.5). For completeness, the phase change of $\rho_{ge,eg}$ due to measurement can be approximately calculated

Table 5.1: Calibrated system parameters

System Parameters		
	Qubit 1	Qubit 2
$\omega^q/2\pi$	4.31143 GHz	4.46143 GHz
$\omega^c/2\pi$	7.1864 GHz	7.1984 GHz
$\kappa/2\pi$	18.5 MHz	21 MHz
$\chi/2\pi$	-1.275 ± 0.025 MHz	-1.085 ± 0.035 MHz
T_1	27 ± 5 μ s	20 ± 3 μ s
T_2^*	16 ± 3 μ s	12 ± 2 μ s
η_{loss}	0.81 ± 0.05	
η_{meas}	0.4 ± 0.10	
G_{chain}	19.8 ± 1.6	

using the master equation result [118]

$$\begin{aligned} \text{Arg}\{\rho_{\text{ge,eg}}(t)\} - \text{Arg}\{\rho_{\text{ge,eg}}(0)\} = \\ 2\chi_1 \int \text{Re}\{A^{(ge)}(t)A^{(eg)}(t)^*\} dt - 2\chi_2 \int \text{Re}\{B^{(ge)}(t)B^{(eg)}(t)^*\} dt. \end{aligned} \quad (5.16)$$

(Here we use a rotating frame with respect to bare frequencies of the qubits.)

So far we have assumed absence of intrinsic decoherence of the qubits. Pure dephasing of the qubits with the corresponding dephasing time $T_{\varphi,1}$ and $T_{\varphi,2}$ can be easily included into the calculation of concurrence by multiplying the main off-diagonal element $\rho_{\text{ge,eg}}(t)$ by the factor $\exp(-t/T_{\varphi,1} - t/T_{\varphi,2})$, where t is the total duration of the measurement procedure. Including the energy relaxation is not so easy, but since its contribution is quite small in the experiment, this can be done in a very crude way. For example, instead of the energy relaxation occurring during the measurement, we can phenomenologically introduce the energy relaxation for time t_{before} before the measurement and then for time t_{after} after the measurement. A better way can be realized by assuming energy decay at a specific random time, and then adding two corresponding parts of the signal integration (5.11); however, we do not apply this protocol to our data. We account for intrinsic dephasing, but not for intrinsic qubit decay.

5.4 Full Calibration of the Experimental Apparatus

Armed with a Bayesian theory for the back-action of the measurement on a cascaded pair of qubits, we turn to a full characterization of the experimental apparatus. Section 5.3 has provided a comprehensive list of experimental parameters that we will need to calibrate in order to quantitatively understand the experiment. These parameters are tabulated in Table 5.1, and a full calibration methodology is provided in this section.

5.4.1 Detailed experimental setup

In Figure 5.6, we show a detailed schematic of the room- and base-temperature experimental setup. The joint measurement requires the use of two GHz microwave generators (to act as local oscillators for qubit and readout pulses); one MHz generator (for double-pumping a cryogenic amplifier); three DC current sources (for biasing the qubits and the amplifier); and an arbitrary waveform generator (AWG, for shaping qubit and readout pulses). The qubits are housed at the base stage of a Vericold cryogen-free dilution refrigerator. Input lines contain 50-60 dB of attenuation and additional homemade lossy Eccosorb low-pass filters at base stage to filter stray infrared radiation. The qubits and cavities are placed inside a blackened copper can, and the cavities are themselves indium-sealed to provide additional infrared shielding. Magnetic shielding is provided by wrapping the cavities individually with aluminum foil and by a μ -metal outer shield that encompasses the copper can.

To implement qubit pulses, the qubits are first tuned to an operating frequency of $\omega_1^q/2\pi = 4.31143$ GHz and $\omega_2^q/2\pi = 4.46143$ GHz. Qubit pulses are implemented using single-sideband modulators (SSBs) with the output of a first generator operating at the midpoint of the two qubit frequencies $\omega_{\text{LO}}^q/2\pi = 4.38643$ GHz serving as the local oscillator (LO). The AWG provides intermediate frequency (IF) pulses at 75 MHz to a lower-sideband SSB (Qubit 1) and an upper-sideband SSB (Qubit 2); these pulses are routed to base and perform single qubit gates via the weakly-coupled ports of the respective cavities.

A second generator operating at the measurement frequency $\omega^m/2\pi = 7.19326$ GHz is split three ways. The joint measurement readout pulses are implemented via a mixer using ω^m as the LO and DC pulses from the AWG as the IF. The output of the mixer passes through a variable phase shift and attenuation and into the dilution refrigerator. At base, the readout passes through a circulator to measure cavity 1 in reflection; is routed back through the circulator and through 1.3 meters of copper cable; measures cavity 2 in reflection via a second circulator; and is routed via an additional isolator to a lumped Josephson parametric amplifier (LJPA) [141] for phase-sensitive amplification. We double-pump the LJPA symmetrically at $\omega^m \pm \omega_{dp}$ to reduce pump leakage at ω^m that could propagate toward the cavities and cause additional unwanted dephasing. The double pump for the LJPA is generated via an IQ mixer with a third generator operating at $\omega_{dp}/2\pi = 369$ MHz on the I port and ω^m as the LO. After the LJPA, the amplified readout passes through two isolators and a low-pass filter en route to a 4K HEMT; at room temperature, the signal is further amplified before demodulation (using the third branch of ω^m as the LO) and digitization for processing.

5.4.2 Cavity parameters

The bare cavity frequencies ω^c and linewidths κ are measured using a standard transmission measurement performed with a vector network analyzer. A probe tone is injected via the weakly-coupled port and collected at the output of the total measurement chain; the transmission spectrum has a characteristic Lorentzian shape, which we fit to extract the

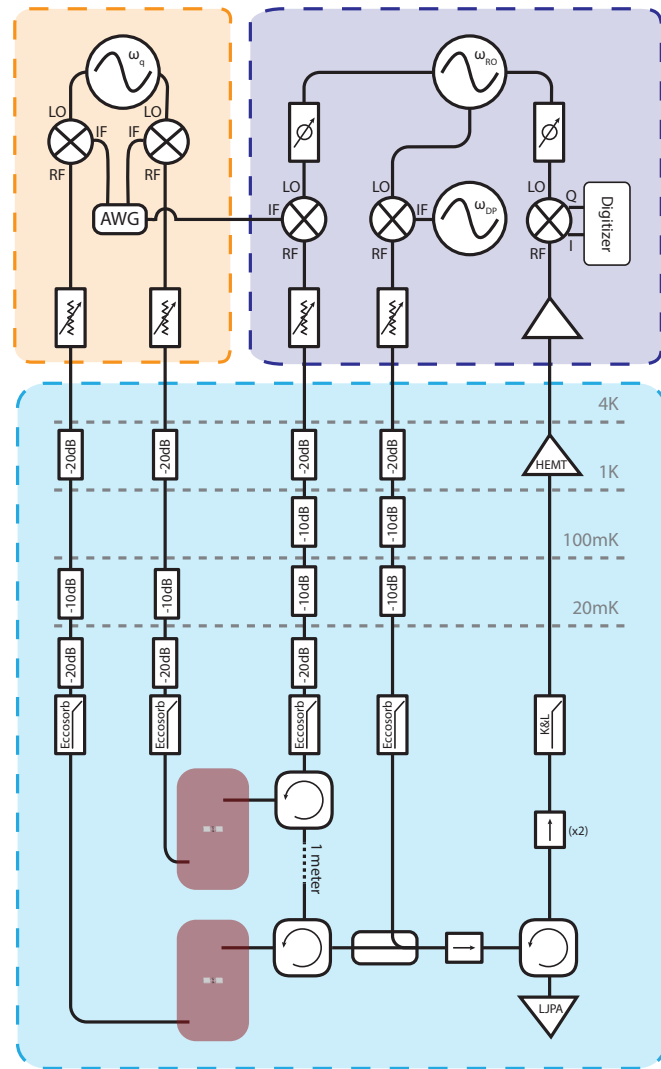


Figure 5.6: Full experimental setup.

cavity parameters. Note that, since there is no qubit drives and the qubits are quite cold, we are actually measuring ω_-^c , the dressed cavity frequency conditioned on the qubit in state $|g\rangle$. Upon an accurate measurement of χ , we can adjust our estimate of the bare resonant frequency.

5.4.3 Qubit lifetimes and coherences

We calibrate T_1 , the qubit relaxation time, and T_2^* , the Ramsey decay time, using standard time-resolved measurements. Specifically, T_1 is calibrated by performing a R_X^π rotation into the $|e\rangle$ state, waiting a variable delay time, performing a strong readout measurement, and fitting the resulting data to a decaying exponential. T_2^* is calibrated using a Ramsey sequence that measures the total loss rate of azimuthal phase coherence. We extract T_φ , the pure dephasing rate, from T_2^* using $\frac{1}{T_2^*} = \frac{1}{T_\varphi} + \frac{1}{2T_1}$.

5.4.4 Calibration of photon number, dispersive shifts, and inter-cavity transmission efficiency

We would like to be able to translate from a calibrated room-temperature measurement power P_m into an equivalent photon number present in the cavities. For this, the qubits themselves provide a highly sensitive meter, allowing us to simultaneously calibrate the photon number (\bar{n}_1), the dispersive shifts at each cavity (χ), and the inter-cavity transmission efficiency (η_{meas}). To calibrate these system parameters, we use a technique similar to Vijay *et al.* [175]. The additional P_m (calibrated at room-temperature with a spectrum analyzer) corresponds to a coherent state in the first cavity given by

$$A_\pm = \frac{\sqrt{\lambda P_m \kappa_1}}{\kappa_1/2 + i(\omega_1^c - \omega^m \mp \chi_1)}, \quad (5.17)$$

where λ represents an unknown (but constant at fixed frequency) attenuation from room-temperature to the cavity. All variables but χ_1 and λ have been independently calibrated. Similarly, because Qubit 1 stays in its ground state when undriven, if we do not drive Qubit 1 we can write the intracavity field at Cavity 2 as

$$B_\pm = \frac{\sqrt{\eta_{\text{loss}} \lambda P_m \kappa_2}}{\kappa_2/2 + i(\omega_2^c - \omega^m \mp \chi_2)} e^{-i\Delta\phi_1}. \quad (5.18)$$

This is the equivalent of Equation 5.17, with the addition of an attenuation $\sqrt{\eta_{\text{loss}}}$ and an overall phase shift due to the presence first cavity.

The intracavity coherent state A creates a measurement-induced dephasing rate given by $\Gamma_{d,1} = \frac{\kappa_1}{2}|A_+ - A_-|^2$ and an ac-Stark shift of $\Delta_\omega = -2\chi \text{Re}\{A_- A_+^*\}$ [118]. An equivalent effect occurs at Qubit 2 due to B . We can measure both Γ_d and Δ_ω by performing Ramsey measurements in the presence of the offset power P_m . The frequency of the Ramsey fringes gives Δ_ω , and their exponential decay envelope gives $\Gamma_{\text{tot}} = \Gamma_d + 1/T_2^*$.

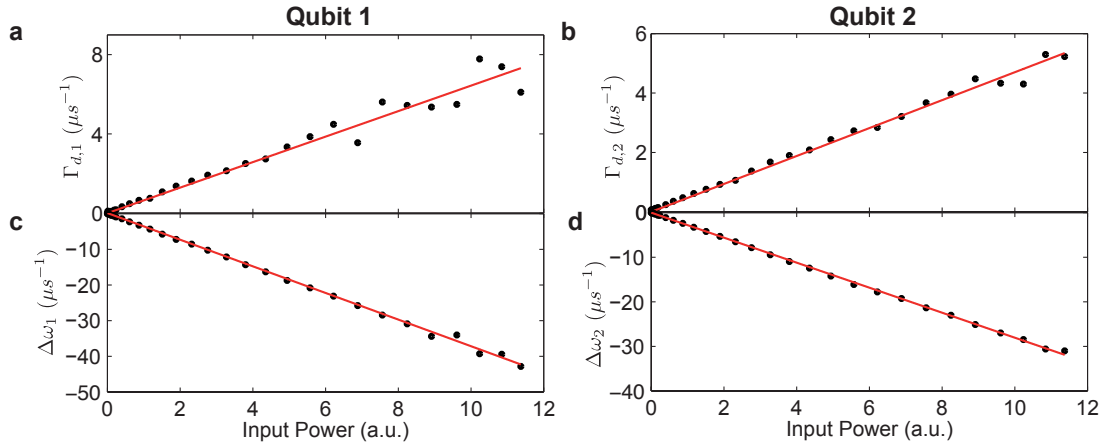


Figure 5.7: \bar{n} , η_{loss} , and χ calibration. We display the measurement-induced dephasing (a-b) and ac-Stark shift (c-d) for Qubit 1 (left) and Qubit 2 (right) as a function of measurement power P_m in arbitrary units. We fit these data in order to determine χ_1 , χ_2 , η_{loss} , and \bar{n}_1 .

We sweep the applied power P_m and perform Ramsey measurements first on Qubit 1 and then on Qubit 2, in order to generate a linear fit of both Γ_d vs. P_m and $\Delta\omega$ vs. P_m for both qubits independently. Removing the $P_m = 0$ offset and taking the ratio $\Delta\omega/\Gamma_d$ removes dependency on λP_m (Qubit 1) and $\eta_{\text{loss}}\lambda P_m$ (Qubit 2); we fit these ratios to a constant from which we extract χ_1 and χ_2 . We then use these values of χ in linear fits of $\Delta\omega(P_m)$ and $\Gamma_d(P_m)$; this provides two independent fits for λ (when we measure Ramsey on Qubit 1) and for η_{loss} (when we subsequently measure Ramsey on Qubit 2). In Figure 5.7, we show these fits for both qubits. The calibration of λ also provides a sensitive photon-number calibration as a function of P_m : once χ_1 and λ have been determined, $\bar{n}_1^\pm = |A^\pm|^2$ is fully determined, as is the drive amplitude $A_d = \sqrt{\lambda P_m}$.

5.4.5 Calibration of η_{meas}

The final remaining parameter is the measurement efficiency η_{meas} . In addition, there is an implicit parameter to calibrate, which we will call G_{chain} . G_{chain} links the amplified, digitized measurement voltage $V_m(t)$ as measured in our physical system, and B_{out} as defined in Section 5.3. G_{chain} is thus the slope of the line $V_m^{(ee)} - V_m^{(gg)}$ vs. $S_{ee} - S_{gg}$, where $V_m^{(ij)}$ is the center of the histogram actually measured with the digitizer (as in Figure 5.5), and S_{ij} is defined in Equation 5.11. Once G_{chain} is determined, we fit the histograms corresponding to the prepared state $|gg\rangle$, $|ge\rangle$, $|eg\rangle$, and $|ee\rangle$ to Gaussian distributions for every measurement time t . The amplification efficiency η_{meas} is linked to the standard deviation of these Gaussians via $1/\sigma = 2\sqrt{\eta_{\text{meas}}t}$ (Equation 5.12). We extract η_{meas} by fitting σ vs $1/\sqrt{t}$ to a line (Figure 5.8).

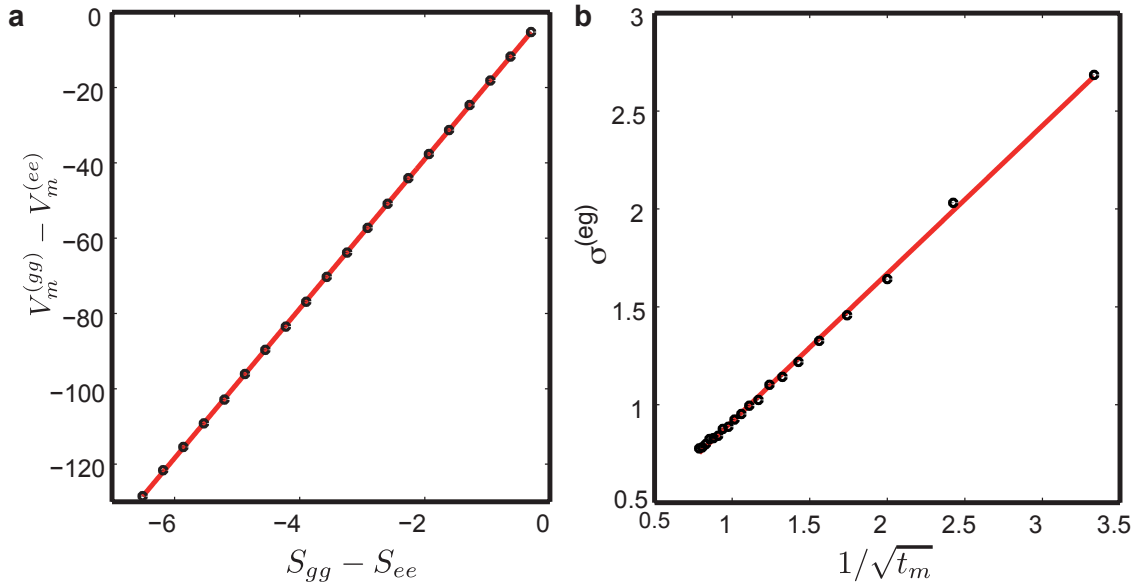


Figure 5.8: Calibration of η_{meas} and G_{chain} . a. Center of the measured histograms as a function of prediction given by the Bayesian theory. We plot the difference between $|gg\rangle$ and $|ee\rangle$ to remove possible offsets. b. Evolution of the standard deviation of the histogram corresponding to prepared state $|eg\rangle$ versus measurement time t .

We define η_{meas} as the mean of the extracted values from the four fiducial states.

5.5 Tomographic Reconstruction of Entanglement Dynamics

With a preliminary confirmation of a half-parity measurement and a fully-calibrated experimental apparatus, we would now like to be quantitative about the quality and dynamics of the entangling process. We control the rate of entanglement generation

$$\Gamma_{\text{meas}} = \frac{1}{2} \eta_{\text{meas}} \eta_{\text{loss}} |A_d|^2 \sin(2\Delta\phi)^2, \quad (5.19)$$

by adjusting the measurement strength via the average intracavity photon number in the first cavity (Equation 5.10). A photon number $\bar{n}_1 = 1.2$ results in $\Gamma_{\text{meas}}/2\pi \approx 210$ kHz, which sets the characteristic timescale of entanglement generation $\tau_{\text{meas}} \equiv 1/\Gamma_{\text{meas}} \approx 750$ ns. Thus, the dynamics of the measurement process, which are significantly faster than qubit decay rates, can be readily resolved using conventional digital electronics. We therefore

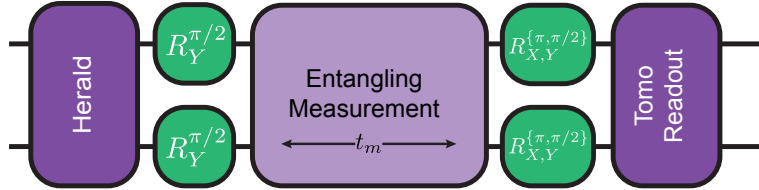


Figure 5.9: Sequence of measurement and rotation pulses required for entanglement and tomographic state reconstruction. Pulses at the qubit frequency are shown in green; pulses at the cavity frequency are in purple (with pulse strength indicated schematically via color intensity).

use $\bar{n}_1 = 1.2$ for our weak measurements. In contrast, our projective readout is performed with $\bar{n}_1 = 6.2$ photons, corresponding to $\Gamma_{\text{meas}}/2\pi \approx 5.6$ MHz, or $\tau_{\text{meas}} = 28$ ns. τ_{meas} is significantly faster than intrinsic qubit decay timescales in this regime, which fulfills our need for a fast, high-fidelity readout.

A reader might well inquire as to the difference between “strong” and “weak” measurement. Indeed, the strong and weak measurements used here lie on the same continuum and can be tuned at will. The terms, therefore, are a descriptive and relative shorthand (and a relatively sloppy one) for comparison of measurement rates within an experiment such as this one. We might interchange “strong” with “projective”, but again, the ability of a measurement to fully project a system is also relative. The “strong” measurements used here are measurement for which we are not interested in reconstructing the underlying dynamics or for which the dynamics are too fast to be captured by our electronics; the “weak” measurements are those for which we wish to and are able to study the dynamical processes.

To generate and verify entanglement, we implement a sequence of three readout protocols and two qubit rotations (Figure 5.9). We first perform a projective readout and post-select the $|gg\rangle$ ground state [180]. We then perform $R_Y^{\pi/2}$ rotations on both qubits to create the equal superposition state $\frac{1}{2}(|gg\rangle + |ge\rangle + |eg\rangle + |ee\rangle)$. The second readout, which is done in the weak regime with varying t , stochastically steers the system toward $|gg\rangle$, $|ee\rangle$, or the Bell state $\frac{1}{\sqrt{2}}(|ge\rangle + |eg\rangle)$, as documented in the measurement output V_m . We then apply one of a set of tomographic rotations [181] immediately followed by a final projective readout into $|gg\rangle$, $|ee\rangle$, or $\{|ge\rangle, |eg\rangle\}$. The tomography is described in greater detail in the next section.

The tomographic and state preparatory rotations are tuned to 40 ns, and we provide a 10 ns window between the end of a qubit pulse and the beginning of a readout protocol in order to ensure that the rotations are not distorted by photon-induced qubit frequency shifts. Similarly, after a readout is performed, we wait a minimum of $t = 6/2\pi\kappa$ before applying a qubit pulse in order to ensure the cavity is fully depopulated.

We repeat the entangling process 8,000 times for each tomographic rotation and for each t to form a single well-averaged data set; we generate an error margin by taking the average and standard deviation of 17 data sets. To produce the density matrix of the entangled state for each time t , we choose an entanglement probability p_{ent} to constitute the entangled state, select an integration window to contain the p_{ent} most-likely-entangled experimental iterations, and tomographically reconstruct the density matrix from the data set contained in this window using a maximum-likelihood estimator [167, 182]. For perfectly separated histograms, 50% of the counts will lie in the odd-parity subspace, but we utilize $p_{\text{ent}} = 10\%$ to compensate for imperfect measurement efficiency.

5.5.1 Characterizing the tomographic reconstruction

The joint dispersive measurement that we have designed randomly projects the system into $|gg\rangle$, $|ee\rangle$, or $\{|ge\rangle, |eg\rangle\}$. Repetitively performing the measurement on an identically prepared ensemble therefore yields the probabilities $p_{|gg\rangle}$, $p_{|ee\rangle}$, and $p_{|ge\rangle} + p_{|eg\rangle}$. These probabilities, in turn, represent the diagonal density matrix elements $\rho_{gg,gg}$, $\rho_{ee,ee}$, and $\rho_{ge,ge} + \rho_{eg,eg}$. The tomographic process utilizes our ability to measure a subset of these density matrix elements and to rotate other matrix elements into these “readable” slots in order to reconstruct the full density matrix.

To reconstruct the density matrix, we need at least fifteen linearly independent measurements in order to span the degrees of freedom of the two-qubit density matrix (a 4x4 Hermitian matrix, with a trace-normalization constraint). These degrees of freedom can alternatively be considered as projections of the density matrix onto the two-qubit Pauli operators $\hat{\sigma}^{ij}$. However, one can easily see that the only Pauli operators with nonzero diagonal density matrix elements are $\{\hat{\sigma}^{II}, \hat{\sigma}^{IZ}, \hat{\sigma}^{ZI}, \hat{\sigma}^{ZZ}\}$. Measuring $p_{|gg\rangle}$ is the equivalent of measuring $\text{Tr}\{\hat{\mathcal{M}}_{gg}\rho\}$, where $\hat{\mathcal{M}}_{gg} = \hat{\sigma}^{II} + \hat{\sigma}^{IZ} + \hat{\sigma}^{ZI} + \hat{\sigma}^{ZZ}$. We can write a similar measurement operator for a measurement of $|ee\rangle$: $\hat{\mathcal{M}}_{ee} = \hat{\sigma}^{II} - \hat{\sigma}^{IZ} - \hat{\sigma}^{ZI} + \hat{\sigma}^{ZZ}$. Similar decompositions can be written for $p_{|ge\rangle}$ and $p_{|eg\rangle}$. However, because we cannot use our measurement to distinguish between $|ge\rangle$ and $|eg\rangle$ in this experiment, we will use only the $|gg\rangle$ and $|ee\rangle$ probabilities for tomographic purposes.

In order for our measurements to span the full Hilbert space, we must design a set of rotations that take the remainder of the Pauli matrix projections ($\hat{\sigma}^{IY}, \hat{\sigma}^{XZ}$, etc.) into one of these four measurable positions. Thus we can build up a set of measurement operators that, taken together, can determine the full Pauli matrix decomposition of the system and thus reconstruct the density matrix. Of course, since we are discussing probabilities, we must prepare the system and perform each rotation and measurement many times in order to build an accurate estimate of the probabilities, and thus a true picture of the ensemble density matrix.

Our tomography procedure utilizes a set of 30 qubit rotations (15 positive and negative rotations) in order to reduce systematic bias from qubit rotations and power drifts. The rotations are identical to those in Ref. [181] and are given explicitly in Table 5.2. For

each rotation, we independently measure $p_{|gg\rangle}$ and $p_{|ee\rangle}$ in order to double the amount of information we extract from each experiment. These probabilities represent measurements of the form

$$\begin{aligned} p_{|ij\rangle} &= \text{Tr}\{\hat{\mathcal{M}}_{|ij\rangle}\rho\}; \\ \hat{\mathcal{M}}_{|ij\rangle} &= \beta_{II}\hat{\sigma}^{II} \pm \beta_{IZ}\hat{\sigma}^{Im} \pm \beta_{ZI}\hat{\sigma}^{nI} \mp \beta_{ZZ}\hat{\sigma}^{nm}. \end{aligned} \quad (5.20)$$

Here $+(-)$ corresponds to $p_{|gg\rangle}$ ($p_{|ee\rangle}$), and $m, n \in \{X, Y, Z\}$. The choice of m, n depends on the prerotation performed before the measurement. The β -coefficients are calibrated using a double-Rabi measurement as described in Chow *et al.* [181] and allow us to account for measurement inefficiency and qubit decay during readout.

Our measurement set results in an overspecified measurement set: 60 effective measurements for 15 degrees of freedom. We convert this data into a density matrix using a least-squares maximum likelihood estimation method [182] to enforce trace normalization and Hermiticity of the reconstructed density matrix. Specifically, we define a sixteen element real vector \vec{t} and use its elements to construct a lower-triangular matrix of the form

$$T = \begin{pmatrix} t_1 & 0 & 0 & 0 \\ t_5 + it_6 & t_2 & 0 & 0 \\ t_7 + it_8 & t_9 + t_{10} & t_3 & 0 \\ t_{11} + it_{12} & t_{13} + it_{14} & t_{15} + it_{16} & t_4 \end{pmatrix} \quad (5.21)$$

and write

$$\rho_t = \frac{T^\dagger T}{\text{Tr}\{T^\dagger T\}} \quad (5.22)$$

As long as T is invertible, ρ_t is semipositive definite, and is therefore a Hermitian, trace-normalized density matrix. This is the constraint we seek. We then construct a minimization vector \vec{L} where each element is given by

$$\mathcal{L}_{|ij\rangle,k} = \text{Tr}\{\hat{\mathcal{M}}_{|ij\rangle,k}\rho_t\} - p_{|ij\rangle,k}. \quad (5.23)$$

Here, k indexes the prerotations that are performed to complete the tomographic set. The vector \vec{L} represents a comparison of the expected measurement outcome for the test matrix ρ_t under measurement $\hat{\mathcal{M}}_k$, to the experimentally measured outcomes (with a separate vector element for the $|gg\rangle$ and $|ee\rangle$ measurements, which we consider independent). Using a nonlinear least-squares minimization protocol (in our case, the lsqnonlin function native to the MATLAB environment), we vary \vec{t} until \vec{L} is minimized, and consider the corresponding ρ_t to represent the true density matrix ρ .

One could also consider using standard matrix methods to construct a matrix of measurement operators and a corresponding vector of outcomes, then taking the pseudoinverse in order to reconstruct the density matrix. These methods produce qualitatively similar results. The data shown in this dissertation are based on the maximum likelihood method.

We verify the accuracy of the tomography by preparing the state $\frac{|g\rangle+|e\rangle}{\sqrt{2}} \otimes \frac{|g\rangle+e^{i\phi}|e\rangle}{\sqrt{2}}$ and calculating the fidelity of the resulting density matrix to the target state (Figure 5.10). The average fidelity across the prepared states is 98.8%, indicating highly effective state initialization and tomographic reconstruction.

Table 5.2: Tomographic rotations and measurement operators

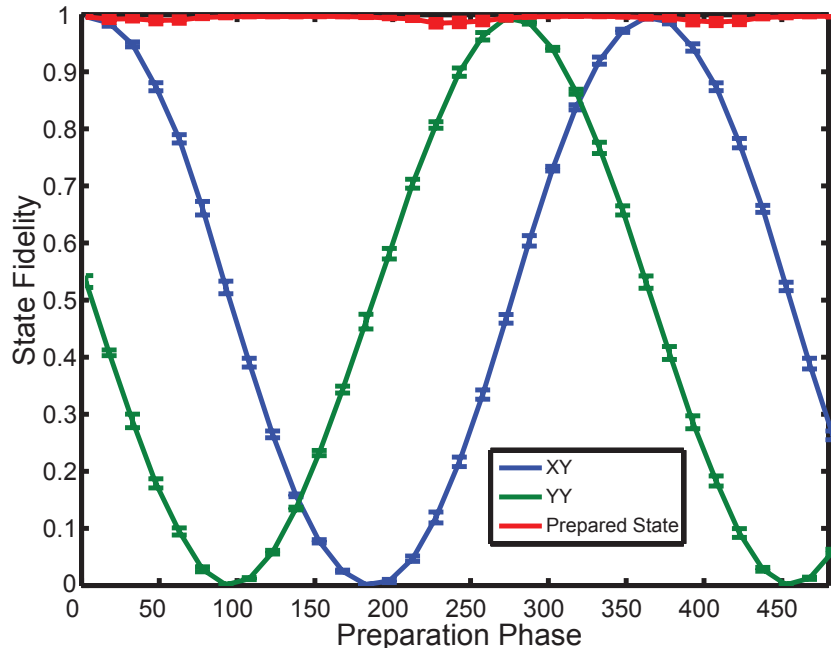


Figure 5.10: Fidelity to the states $\frac{|g\rangle+|e\rangle}{\sqrt{2}} \otimes \frac{|g\rangle+|e\rangle}{\sqrt{2}}$ (XX), $\frac{|g\rangle+|e\rangle}{\sqrt{2}} \otimes \frac{|g\rangle+i|e\rangle}{\sqrt{2}}$ (XY) and $\frac{|g\rangle+|e\rangle}{\sqrt{2}} \otimes \frac{|g\rangle+e^{i\phi}|e\rangle}{\sqrt{2}}$ (Target State) as a function of Qubit 2 preparation phase ϕ . Fidelities to XX and XY oscillate 90 degrees out of phase with one another, as expected; the fidelity to the prepared state is an average of 98.8% across all preparation angles.

5.5.2 Entanglement dynamics

The ability to perform time-continuous measurements enables us to directly observe the ensemble dynamics of the emergence of entanglement. As noted in Section 5.3, we can estimate concurrence [107] using the simplified formula [110] (Equation 5.5) to characterize the quality of the entanglement during this process. This simplified formula holds when the only non-negligible off-diagonal elements are $\rho_{ge,eg}$ and its conjugate, which is applicable to our setup since the high distinguishability between $|gg\rangle, |ee\rangle$ and the $\{|ge\rangle, |eg\rangle\}$ manifold results in rapid decay of all other off-diagonal elements. Recall that concurrence ranges from zero (for a separable or mixed state) to one (for a maximally entangled two qubit state), and is greater than zero for all non-separable two qubit states [107]. Maximizing \mathcal{C} requires limiting decoherence within the odd-parity manifold, and minimizing stray counts of $|gg\rangle$ and $|ee\rangle$ by maximizing the signal-to noise ratio (SNR), defined by the ratio of the separation of the Gaussian measurement histograms (in Figure 5.5) to their width, or

$$\text{SNR} \sim 2|A_d| \sin(2\Delta\phi) \sqrt{\eta_{\text{loss}}\eta_{\text{meas}}t}. \quad (5.24)$$

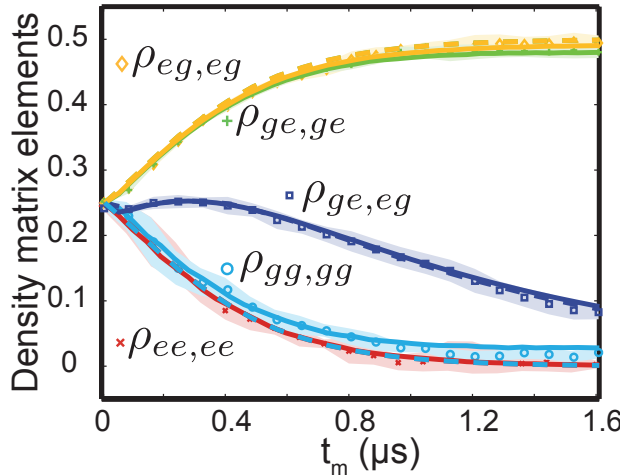


Figure 5.11: Generation and verification of entanglement between two spatially-separated superconducting qubits. The figure displays the evolution of the basis state populations ($\rho_{gg,gg}$, etc.) and odd-parity coherence ($\rho_{ge,eg}$). The shaded region represents the standard deviation centered about the average (geometric shapes). Dashed lines are theoretical simulations based on a Bayesian approach and solid lines are calculated using a master equation approach; in both cases no fitting parameters are used.

Figures 5.11 and 5.12 show the evolution of the density matrix as a function of t . Figure 5.11 details the evolution of the relevant density matrix elements (the diagonal elements, representing population probabilities, and the off-diagonal element $\rho_{ge,eg}$, representing the coherence of the odd-parity subspace), as the entangled ensemble is better and better post-selected. Figure 5.12 shows the full density matrix for five selected values of t . As expected, the off-diagonal elements not associated with the odd-parity subspace rapidly decay to zero. Note that we plot here the amplitude of the density matrix elements, when in fact the off-diagonal elements are in general complex. In particular, the off-diagonal density matrix element evolves deterministically due to the slight differences in χ between the two qubits (Equation 5.16). However, note that Equation 5.5 refers only to the amplitude $|\rho_{ge,eg}|$, and not to its complex phase. Therefore, the amplitudes contain all the information we need to study entanglement. In Figure 5.13, we show the concurrence calculated from these density matrices as a function of measurement integration time.

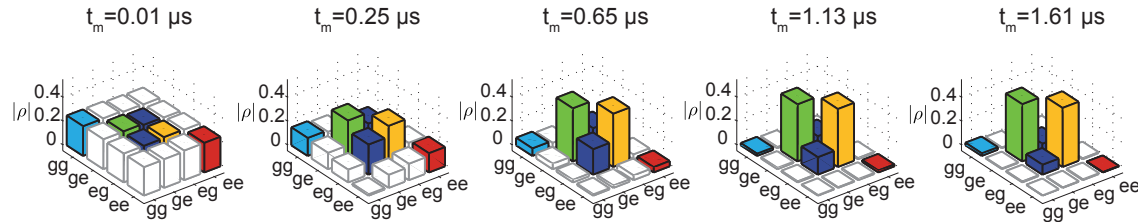


Figure 5.12: Full density matrices of the post-selected entangled subspace for increasing t . The off-diagonal elements corresponding to coherences outside of the odd-parity subspace decay much more rapidly than $|\rho_{ge,eg}|$, as required for entanglement generation. The off-diagonal elements outside the entangled subspace can be calculated phenomenologically using the Bayesian formalism, and from first-principles using the SME formalism [179].

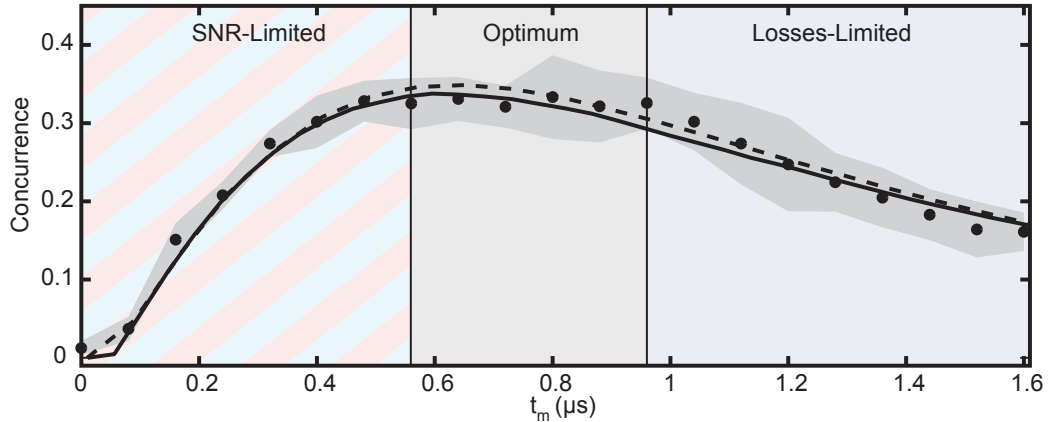


Figure 5.13: Concurrence of the post-selected entangled state as a function of t . As in Figure 5.11, the dashed lines represent the Bayesian analysis; solid lines represent the SME approach; closed circles represent the data; and the shaded region represents the standard deviation of the tomographic set. We see three qualitative regions: an initial purification of entanglement, rate-limited by the SNR; an optimum region with balance between SNR improvement and losses; and a region of decay where the dynamics are dominated by loss mechanisms.

5.6 Discussion of Results

In describing the evolution of the density matrix elements and overall concurrences in Figures 5.11, 5.12, and 5.13, we note three qualitative regimes: SNR-dominated evolution; stabilization; and decay due to decoherence. Since the SNR for integrated gaussian noise is proportional to \sqrt{t} , it dominates the evolution at short times $t < 0.75\tau_{\text{meas}}$. Here, the dynamics are governed by changes to population probabilities; i.e., the increase of $\rho_{\text{eg},\text{eg}}$ and $\rho_{\text{ge},\text{ge}}$ and decrease of $\rho_{\text{gg},\text{gg}}$ and $\rho_{\text{ee},\text{ee}}$ in the post-selected ensemble. The rapid decay of $\rho_{\text{gg},\text{gg}}$ and $\rho_{\text{ee},\text{ee}}$ compared to $\rho_{\text{ge},\text{eg}}$, results in growth of concurrence in this regime. For intermediate times ($0.75\tau_{\text{meas}} < t < 1.25\tau_{\text{meas}}$), the SNR improvement rate decreases and decoherence begins to take a more noticeable effect. Decoherence is caused by intrinsic dephasing of the qubits $\Gamma_{2,i}^* = 1/T_{2,i}^*$ and by η_{loss} , which contributes an additional measurement-induced dephasing of the first qubit at a rate

$$\Gamma_{\text{loss}} \simeq 2(1 - \eta_{\text{loss}}) |A_d|^2 \sin(\Delta\phi)^2. \quad (5.25)$$

At intermediate times, the SNR improvement rate and Γ_{loss} are roughly equal, and hence the concurrence reaches a maximum value of 0.35. This value is comparable to what was obtained recently using optical communications [164, 165], however, thanks to our time-continuous measurement scheme, the rate at which an entangled state is created is orders of magnitude higher ($\Gamma_{\text{creation}}/2\pi = 1 \text{ kHz}$). For longer times ($t > 1.25\tau_{\text{meas}}$), the density matrix evolution is dominated by decoherence, which eventually drives the system into an incoherent mixture of $|\text{ge}\rangle$ and $|\text{eg}\rangle$.

These ensemble dynamics are well-described both by a Bayesian statistical model (dashed lines), and by a rigorous stochastic master-equation treatment (solid lines) [179]. The models, which account for the chief technical limitations of our scheme (i.e. the inefficiencies η_{loss} , the losses between the cavities and η_{meas} , the finite detection efficiency), indicate that reasonable technical improvements could lead to concurrence of 70% [167, 179]. The two theories used to model our data represent a rigorous microscopic analysis that natively accounts for all density matrix elements, in the case of the stochastic master equation formalism; and a straightforward phenomenological extension of the single-qubit Bayesian theory, in the case of the Bayesian formalism. The agreement between these models indicates a thorough understanding of the experimental system that enables our entangling measurement.

This work beautifully demonstrates the delicate interplay between measurement and dissipation. Without performing an entangling measurement, there is no direct means of entangling the qubits in our system, so the measurement serves to purify, rather than destroy, an important quantum resource. However, that purification is impeded by two loss mechanisms, η_{loss} and η_{meas} , which affect the measurement dynamics in very different ways. The additional dephasing of the first qubit, and therefore of the entangled state, is principally caused by losses between the two cavities (η_{loss}). Along the path between the cavities, the propagating coherent state only carries information about the state of the first qubit. In the language of SMEs developed in Chapter 2, this is a dissipation term takes the form $\frac{\Gamma_{\text{loss}}}{2} \mathcal{D} [\hat{\sigma}^{ZI}] \rho$, a dephasing term on the Qubit 1 subspace. Any information lost between the

cavities - particularly at the circulators, which contribute an intrinsic loss of nearly 0.4 dB each - is equivalently a measurement of the first qubit that we must average over, which contributes to an effective measurement-induced dephasing.

However, after the second cavity, the signal no longer contains information that distinguishes between $|ge\rangle$ and $|eg\rangle$: the dissipator being applied is of form $\Gamma_{\text{meas}} \mathcal{D} [\hat{\sigma}^{ZI} + \hat{\sigma}^{IZ}] \rho$. In the odd-parity subspace, this term has an expectation value of zero, so the odd-parity subspace is protected from further decoherence due to inefficient transmission to and amplification by the LJPA (captured in η_{meas}). Thus, this second form of loss serves only to limit the rate at which entanglement is generated by slowing the rate of SNR improvement, but does not itself contribute to decoherence. The overall dynamics of the entanglement generation process are governed by an interplay between measurement, dissipation-induced dephasing and collection efficiency, nicely capturing all of the relevant dynamics in a measurement/dissipation process.

Our experiments demonstrate that quantum entanglement can be established between distant systems that interact only through a coherent signal propagating along low loss electrical wires, a functionality that will be integral to the realization of complex, distributed quantum networks. We take advantage of the versatility of continuous measurement to monitor the dynamics of entanglement generation, and demonstrate quantitative agreement to a theoretical model that captures the experimental details of the physical circuit. Moreover, our characterization of the state of the joint system under continuous measurement suggests the feasibility of future *continuous* feedback stabilization of entanglement [171, 177, 183]. Further technical improvements in quantum efficiency, coherence times, and transmission characteristics hold the promise of on-demand, stabilized remote entanglement—a powerful resource for quantum information processing.

Chapter 6

Quantum Trajectories in an Entangling Measurement

A careful analysis of the process of observation in atomic physics has shown that the subatomic particles have no meaning as isolated entities, but can only be understood as interconnections between the preparation of an experiment and the subsequent measurement.

Erwin Schrödinger, *Unsourced Attribution*

Our high-efficiency continuous measurement allows us to go one step further in decomposing the dynamics of measurement-induced entanglement: we can directly observe the individual quantum trajectories [176, 184–187] of our two qubit system. The ability to reconstruct individual quantum trajectories is a tremendous advantage of weak measurements: we can ask not only “Where did the qubits start?” (state initialization) and “Where did they end?” (projective readout) but also “How did they get there?”. By peering into the ensemble to resolve the *single-shot*, dynamical evolution of a quantum system, we gain access to a rich new tapestry of scientific questions:

1. What is the complete characterization of the dynamics of entanglement creation as a continuous trajectory?
2. What is the statistical distribution of the entanglement at any time during the process?
3. What is the most likely way in which entanglement is created?

In this chapter, we give a systematic answer to these questions and more, by analyzing entangled quantum trajectories of jointly measured qubits and by developing a comprehensive theory to understand them. We resolve and describe the full spectrum of evolution paths as the two-qubit state gradually projects onto the entangled subspace or onto a separable state.

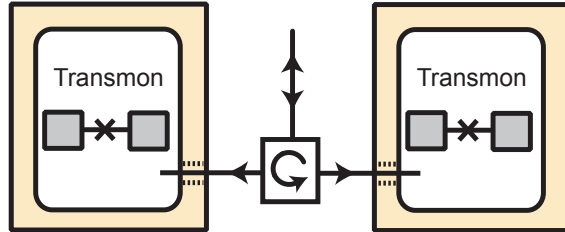


Figure 6.1: Schematic of experimental setup optimized for transmission losses. The cavities are directly connected to a single microwave circulator in order to reduce η_{loss} and therefore to enable the generation of higher-quality entangled states.

We explore the probability distribution of the qubits' concurrence to understand how the distribution changes in time, from a separable state with zero concurrence, to projected states in either a separable subspace or an entangled subspace [170]. This can also be seen from the most likely path analysis, showing the emergence of different most probable paths for each final state. Moreover, we investigate the distribution of the time-to-maximum-concurrence, finding that the most probable time to maximum values of concurrence has a bimodal structure. Studying the statistics of a large set of trajectories - rather than averaging over all of them to study the dynamics of the ensemble - enables an unprecedented understanding of the dynamics of entanglement creation under measurement.

This work was originally published in Ref. [188], and also appears in the thesis of Areeya Chantasri.

6.1 Experimental Generation and Verification of Entangled Trajectories

The experimental setup for this experiment is quite similar to that in Chapter 5. However, in this set of experiments we are more interested in the entanglement generation process than in the remoteness of the measurement; we therefore remove the 1.3 meters of delay cable and one of the circulators (Figure 6.1). By removing these components, we increase the signal transmission efficiency η_{loss} from 0.75 to 0.92, which reduces the measurement-induced dephasing and allows us to reach higher values of concurrence. We characterize and calibrate the system as in Section 5.4; the qubit and cavity parameters are tabulated in Table 6.1.

Table 6.1: Calibrated system parameters

System Parameters		
	Qubit 1	Qubit 2
$\omega_q/2\pi$	4.27225 GHz	4.37226 GHz
$\omega_r/2\pi$	7.1871 GHz	7.1988 GHz
$\kappa/2\pi$	19.8 MHz	18.2 MHz
$\chi/2\pi$	-1.015 ± 0.025 MHz	-1.085 ± 0.035 MHz
T_1	27 ± 4 μ s	17 ± 3 μ s
T_2^*	18 ± 3 μ s	14 ± 2 μ s
η_{loss}	0.92 ± 0.03	
η_{meas}	0.22 ± 0.05	
G_{chain}	12.8 ± 1.3	

6.1.1 Generating quantum trajectories

The pulse sequence used is identical to that shown in Figure 5.9; however, the data collection and processing required to generate trajectories differs. In order to track the trajectories we keep the entire instantaneous homodyne detection signal rather than averaging it over t . The dynamics or the trajectory of the system state can be obtained via the full master equations [177, 179], using a two-cavity polaron transformation to account for the cavity degree of freedom, giving the stochastic master equation for the qubit trajectories. This is a similar procedure to that outlined in Section 4.3. Alternatively, in a limit of large cavity decay rate $\kappa \gg |\chi|$, the qubits evolution can be continuously tracked via the quantum Bayesian approach [156, 172], inferring the current states of the system from the measurement readouts and how likely they are to occur.

In this chapter, as in the previous one, we focus on the quantum Bayesian approach, as it is directly related to the probability distribution of the measurement readout and naturally leads to the probability distribution of quantum trajectories. Following Section 2.2, let us denote $p_{ij}(V_t)$ as a probability density function of a measurement readout V_t conditioned on the two-qubit fiducial states $|ij\rangle$. Here, we define

$$V_t \equiv (f/t) \left[\int_0^t \tilde{V}(t') dt' \right] - v_0 \quad (6.1)$$

as the scaled, averaged readout signal, where $\tilde{V}(t)$ is the instantaneous measurement voltage, and f and v_0 are scaling factors enabling us to translate from the raw experimental data to the theoretical distributions. The quantum Bayesian update for this type of double-qubit measurement provides a convenient way to calculate the joint state at time t , given a known

state at the initial time and the integrated signal V_t ,

$$\rho_{ij,kl}(t) = \frac{\rho_{ij,kl}(0)\sqrt{p_{ij}(V_t)p_{kl}(V_t)}e^{-\gamma_{ij,kl}t}}{\sum \rho_{mn,mn}(0)p_{mn}(V_t)}, \quad (6.2)$$

where $\gamma_{ij,kl}$ is a generalized decoherence rate associated to the matrix element. The decoherence rates combine pure dephasing with measurement-induced dephasing due to η_{loss} and η_{meas} . The form of $\gamma_{eg,ge}$ is given by Eq. (5.15); we do not explicitly derive the other terms decay rates, although they have a similar form. Eq. (6.2) is a generalized formulation of Eq. (5.14) that applies to all density matrix elements. We have neglected T_1 -type decay.

Given a properly calibrated measurement chain, we can *a priori* predict the distributions $p_{ij}(V_t)$ using the Bayesian update formulae in Eqs. (5.11) and (5.12); predicting the density matrix evolution given a measurement record $\tilde{V}(t)$ is then straightforward. Specifically, the conditional readout distributions $p_{ij}(V_t)$ are well-approximated by Gaussian functions

$$p_{ij}(V_t) = (t/\pi s)^{-1/2} \exp\{-[V_t - S_{ij}]^2 t/s\} \quad (6.3)$$

with the signal centroids S_{ij} as defined in Eq. (5.11) and $s = 1/2\eta_{\text{meas}}$. The measurement process cannot distinguish the two states in the odd-parity subspace, therefore the readout distributions corresponding to the states $|ge\rangle$ and $|eg\rangle$ are completely (or nearly) overlapped, giving $S_{ge} \approx S_{eg} \approx 0$ and $-S_{gg} \approx S_{ee} \equiv S$. The measurement strength is characterized by an inverse of a characteristic measurement time $\tau_m \approx 1/S^2\eta_{\text{meas}}$. The dephasing rates $\gamma_{ij,kl}$ for $S_{ij} \neq S_{kl}$ are dominated by the effect of the distinguishability between states $|ij\rangle$ and $|kl\rangle$, $\gamma_{ij,kl} \sim (\eta_{\text{meas}}^{-1} - 1)(S_{ij} - S_{kl})^2/4s$, resulting in the strong suppression of all off-diagonal elements except $\rho_{ge,eg}$ when the system is projected towards the entangled subspace. In an ideal half-parity measurement, the decay of $\rho_{ge,eg}$ would be limited only by the intrinsic lifetimes of the qubits; however, we must additionally account for experimental imperfections in the matching of S_{ge} and S_{eg} and for the loss of photons between the two cavities. These effects are included in the (slightly time-dependent) dephasing rate $\gamma_{ge,eg}$.

6.1.2 Validating the quantum trajectories

The previous development allows us to predict, based on a thorough calibration of the experimental system and a careful collection of the measurement output signal, the continuous trajectory of a single experimental iteration. However, we would like to experimentally verify that the actual trajectory of the system matches the Bayesian prediction. In other words, we would like to experimentally generate a mapping $V_t \mapsto \rho(V_t)$ and compare it to the Bayesian update provided by Eq. (6.2). To do so, we perform a series of experiments very similar to those described in Chapter 5. We collect a large set of trajectories for which we record only the integrated signal V_t , not the instantaneous signal $\tilde{V}(t)$, while varying the integration time t . Instead of post-selecting an entangled ensemble, however, we collect all experiments with similar weak measurement outcomes $V_t \pm \epsilon$ at *fixed* time t , and perform a conditional tomographic state reconstruction of those trajectories. This is in principle the same procedure

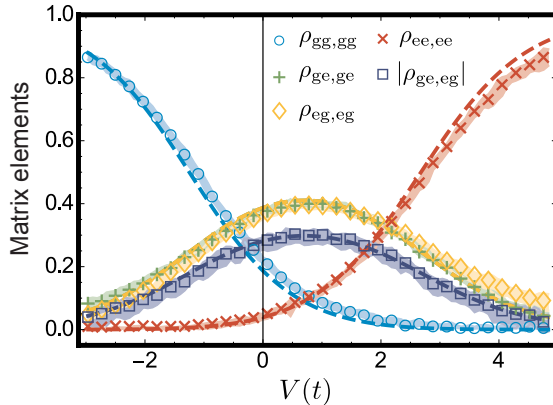


Figure 6.2: Comparison of conditional tomography to predicted $\rho(V_t)$ at fixed $t = 0.48 \mu\text{s}$. Experimentally constructed conditional density matrices are shown using open symbols; the colored shaded regions denote error bars. The predicted density matrix $\rho(V_t)$ from the Bayesian formalism is shown by dashed lines.

carried out in Section 5.5; however here, we use $p_{\text{ent}} \ll 1$ and sweep the target V_t over all values, rather than specializing to the V_t most likely to maximize entanglement. Figure 6.2 shows a comparison between the experimentally constructed ρ and the Bayesian prediction for all V_t at a single t : we see in fact that there is excellent agreement between the Bayesian prediction and the experimental trajectory¹.

Having verified the Bayesian trajectory at a single measurement time, we can proceed to reproduce this data for all time, and thus generate a complete experimental mapping $V_t \mapsto \rho(V_t)$. Figure 6.3 which presents full tomographic mappings for the diagonal matrix elements $\rho_{gg,gg}$, $\rho_{ge,ge}$, $\rho_{eg,eg}$, and $\rho_{ee,ee}$ at all times. We then record a set of trajectories in which we keep the full instantaneous voltage, and integrate it in post-processing for a range of t so that we can reconstruct the full continuous trajectories $\rho(t)$ for the *individual* experimental realizations. Figure 6.4 shows an exemplar trajectory for a full measurement time of $1.6 \mu\text{s}$. The Bayesian update (shown as solid lines) is performed every 10 ns; due to hardware limitations, the experimental conditional tomography is updated every 80 ns. The slightly jagged nature of the Bayesian data is due to finite bin size.

This particular trajectory takes a very interesting path through state space. Early fluctu-

¹ It is of some philosophical interest to note that, in constructing the mapping $V_t \mapsto \rho(t)$ in this way, we have explicitly made the Markov approximation. There is no *a priori* reason to presume that the final state of the system should depend only on the average signal, and not on the specific path (fluctuations) that led to that average signal. Indeed, the thousands of trajectories making up the ensemble used to reconstruct $\rho(t)$ for a given V_t will in general all have unique paths up until t , when their mean signals coincide. Therefore, in some sense the quantitative agreement seen in Figure 6.2 between theory and data is a confirmation that the Markov approximation is appropriate in this system

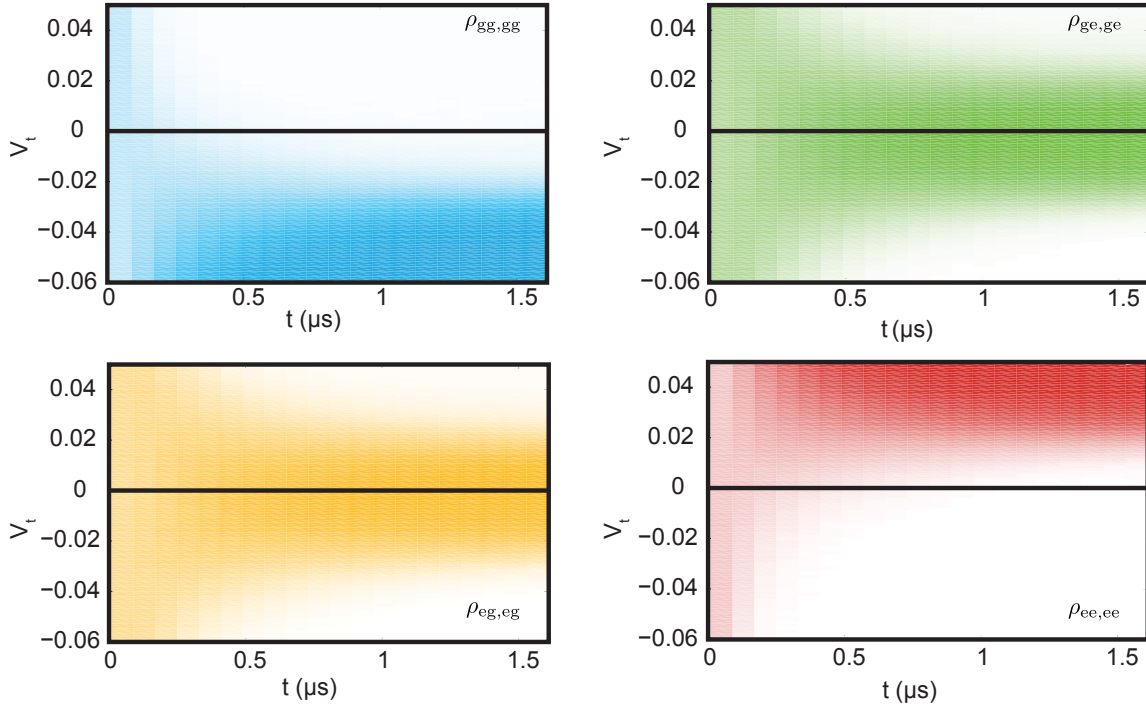


Figure 6.3: Full experimental mapping $V_t \mapsto \rho(V_t)$ for the diagonal density matrix elements.

ations appear to be driving the system toward the joint ground state as $\rho_{gg,gg}$ increases; however, the system then seems to stabilize into the entangled subspace for $0.4 \mu\text{s} < t < 1 \mu\text{s}$, with concurrence $\mathcal{C} \approx 0.45$. After this, fluctuations again take the system out of the entangled state and toward $|gg\rangle$, only to return to the entangled state as the measurement concludes. We emphasize here that this is the true trajectory of this iteration of the entangling measurements, and that this exciting path represents the predicted and experimentally confirmed back-action of the fluctuating measurement field on the qubit pair. The excellent agreement between the tomographic reconstructions of the trajectories and theoretical predictions based on Bayesian updates, even for this complicated trajectory, demonstrates the validity of Bayesian quantum trajectory theories for cascaded quantum systems. In Ref. [167], we show equally clean agreement between tomographically reconstructed trajectories and the full master equation approach laid out in Ref. [179], providing further, more theoretically rigorous support for the quantum trajectory approach first developed in Refs. [189, 190].

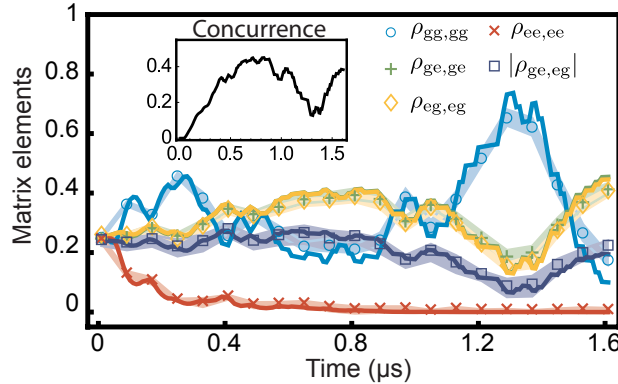


Figure 6.4: Comparison of experimentally constructed trajectories to the Bayesian prediction. Experimental data are shown with open signals and shaded error bars; the Bayesian prediction is shown in solid lines. The inset displays the trajectory of the concurrence as calculated from the Bayesian formalism.

6.2 Statistical Properties of Concurrence Trajectories

We have now seen that a minimal Bayesian formula well-describes the evolution of a bipartite quantum system under the influence of an entangling measurement. We would now like to go a step further: we will use our well-calibrated experimental system to explore the statistical properties of entangled trajectories. Doing so allows us to peer inside the ensemble dynamics observed in Chapter 5 and to develop a deeper and more sophisticated understanding of continuous measurement-induced entanglement.

As we saw in Chapter 3, concurrence is a convenient choice of measure for bipartite entanglement because can be computed directly from the density matrix of the system [107]. The concurrence formula for the partial-parity setup is greatly simplified because of the suppression of most matrix elements, so for the theoretical development below we use the simplified formula. In this section, we will develop a Bayesian prediction of the concurrence directly from the measurement readout, which then leads to the derivation of the concurrence probability distribution as a function of the measurement readout and measuring time.

6.2.1 Concurrence-readout relationship

Let us consider the concurrence formula for the odd-parity subspace,

$$\mathcal{C} = 2 \max(0, |\rho_{ge,eg}| - \sqrt{\rho_{gg,gg}\rho_{ee,ee}}). \quad (6.4)$$

We will define the comparator function as

$$c_t = 2 \left\{ |\rho_{ge,eg}(t)| - \sqrt{\rho_{gg,gg}(t)\rho_{ee,ee}(t)} \right\} \quad (6.5)$$

If c_t is non-negative, then the concurrence is simply given by $\mathcal{C}(t) = c_t$. We will show at the end of this section that this is always the case for our chosen initial qubit state and parameter regimes, but is not true in general [170]. From the Bayesian update and the readout distribution functions in Section 6.1.1, we calculate the quantity,

$$c_t(V_t) = \frac{2}{N} \left\{ |\rho_{ge,eg}(0)| \sqrt{p_{ge}(V_t)p_{eg}(V_t)e^{-\gamma t}} - \sqrt{\rho_{gg,gg}(0)\rho_{ee,ee}(0)p_{gg}(V_t)p_{ee}(V_t)} \right\}, \quad (6.6)$$

where $\gamma \equiv \gamma_{ge,eg}$ and N is a normalized factor given by $N = \sum_{ij} \rho_{ij,ij}(0)p_{ij}(V_t)$. Substituting the arbitrary probability distribution functions for Gaussian functions with mean S_{ij} and widths $\sigma(t)$ we obtain a form of $c_t(V_t)$ explicitly as a function of V_t and t ,

$$c_t(V_t) = \frac{2}{\mathcal{M}} \left\{ |\rho_{ge,eg}(0)| e^{[\alpha_{ge,eg} V_t - \beta_{ge,eg} - \gamma]t} - \sqrt{\rho_{gg,gg}(0)\rho_{ee,ee}(0)} e^{[\alpha_{gg,ee} V_t - \beta_{gg,ee}]t} \right\}, \quad (6.7)$$

where the prefactor is given by $\mathcal{M} = \sum_{ij} \rho_{ij,ij}(0)e^{2\alpha_{ij}V_t - 2\beta_{ij}t}$ using a set of defined variables:

$$\alpha_{ij} = S_{ij}/s \quad \alpha_{ij,kl} = \alpha_{ij} + \alpha_{kl}; \quad (6.8)$$

$$\beta_{ij} = S_{ij}^2/2s \quad \beta_{ij,kl} = \beta_{ij} + \beta_{kl}. \quad (6.9)$$

Critically, $c_t(V_t)$ depends only on the starting state of the system and the integrated measurement voltage, such that we can quantitatively predict the entanglement using only the inputs already required for the Bayesian update.

The quantity $c_t(V_t)$ represents the true concurrence of the joint qubit state if $c_t \geq 0$ is satisfied. For our chosen initial state, a product of single qubit \hat{x} -states, $c_t(V_t)$ is non-negative whenever the condition

$$(\gamma - \alpha_{ge,eg}V_t + \beta_{ge,eg}) < (\beta_{gg,ee} - \alpha_{gg,ee}V_t) \quad (6.10)$$

is true. In our experiment, we have $-S_{gg} \approx S_{ee}$ and $S_{ge} \approx S_{eg} \approx 0$, giving $\alpha_{gg,ee}, \alpha_{ge,eg}, \beta_{ge,eg} \approx 0$. For $\tau_m = 0.60 \mu s$ we have $\beta_{gg,ee} \sim 3.4$ MHz, while $\gamma < 1.7$ MHz. With these values, the condition in Eq. (6.10) is always satisfied. The second term in the bracket of Eq. (6.7) decays faster than the first term, so that the concurrence is always nonzero. Consequently, we can define the concurrence-readout relationship $\mathcal{C}(V_t) = c_t(V_t)$, such that the concurrence at any time t can be determined directly from the time-average measurement readout V_t .

The concurrence formula in Eq. (6.7) can be simplified further by considering a perfectly symmetric partial-parity measurement, $S_{ge} = S_{eg} = 0$ and $-S_{gg} = S_{ee} = S$. Given the initial state, a product of two qubit \hat{x} -states, the concurrence is then given by,

$$\mathcal{C}_{sp,\hat{x}}(V_t) = \frac{e^{-\gamma t} - e^{-S^2 t/s}}{1 + \cosh[2V_t St/s]e^{-S^2 t/s}}, \quad (6.11)$$

where the subscript ‘sp, \hat{x} ’ indicates the perfectly symmetric partial-parity measurement given the specific initial state.

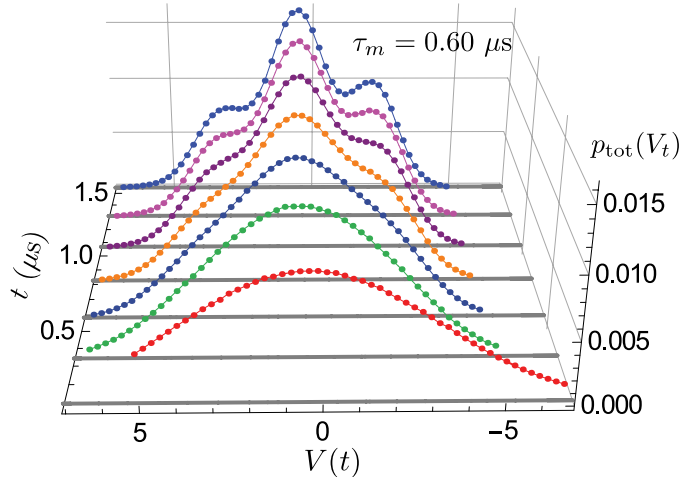


Figure 6.5: Evolution of $p_{\text{tot}}(V_t)$ as integration time increases.

6.2.2 Probability density function for concurrence trajectories

From the direct relationship between the measurement readout and the concurrence of the qubits state, the probability density function of the concurrence can be derived from the probability distribution of the measurement signal. The distribution of the time-average readout is given by a sum of Gaussians,

$$p_{\text{tot}}(V_t) = \sum_{ij} \rho_{ij,ij}(0) p_{ij}(V_t). \quad (6.12)$$

The variance of the distribution $\sigma^2 = s/2t$ narrows as time increases, leading to the collapse of the joint qubit state into three categories: $|gg\rangle$, $|ee\rangle$, and some superposition state of $|ge\rangle$ and $|eg\rangle$ after a few characteristic measurement times τ_m . The experimental measurement probability distribution shown in Figure 6.5 slowly resolves into the three peaks expected for a half-parity measurement, and the resulting concurrence probability density is shown in Figure 6.6.

Given the distribution of the time-averaged signal, we follow the transformation of random variables $V_t \mapsto \mathcal{C}(V_t)$ using the concurrence-readout relationship. The concurrence is not a monotonic function in V_t ; instead it has a bell-like shape as shown in the inset of Figure 6.6a. We write the cumulative distribution function of the concurrence

$$F(c, t) = p(\mathcal{C} \leq c, t) = p_{\text{tot}}(V_t \leq V_-) + [1 - p_{\text{tot}}(V_t \leq V_+)], \quad (6.13)$$

where V_+ , V_- are two solutions that arise from solving Eq. (6.7) for $\mathcal{C}(V_t) = c$. The concur-

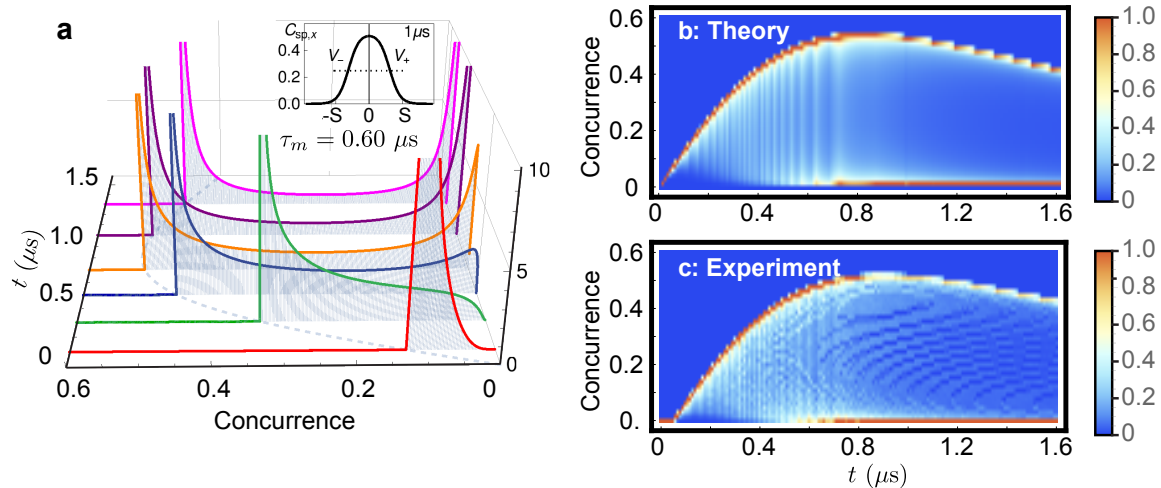


Figure 6.6: Concurrence distribution for the qubits under the partial-parity measurement. In panel (a), we plot the concurrence probability density function Eq. (6.14) for different values of time. The values of time for the presented curves are chosen so as to see their unique features as they develop. The grey dotted curve joining the high-concurrence peaks shows the concurrence upper bound Eq. (6.15). The inset shows an example of how the concurrence (at time $t = 1 \mu s$) varies as a function of the readout V_t . (b) and (c) are the histograms of the concurrence at any time points from $t = 0$ to $t = 1.6 \mu s$ (with a step size $0.01 \mu s$), comparing theory and experimental data. For the theory plot, we coarse-grain the distribution $p_{c,t}(c)$ in Eq. (6.14) by integrating it with a pixel size $\delta c \sim 0.015$, which is the bin size of the experimental histogram. For presentation purposes, a histogram at any time t is normalized by its maximum element.

rence distribution is then obtained by taking a derivative of the cumulative distribution,

$$p(c, t) = p_{\text{tot}}(V_-) \left| \frac{\partial V_-}{\partial c} \right| + p_{\text{tot}}(V_+) \left| \frac{\partial V_+}{\partial c} \right|, \quad (6.14)$$

noting that $V_-(c, t)$ and $V_+(c, t)$ are functions of the concurrence c and time t . The full solution of $p(c, t)$ is quite lengthy and is not shown.

We show in Figure 6.6a the plots of concurrence probability distributions Eq. (6.14) for several different values of time t . In Figure 6.6b-c, we show a comparison between the theoretical $p(c, t)$ and the experimental distribution of concurrence. At an early time, the distribution of concurrence is narrowly peaked near its maximum which increases over time, whereas at later times, a second peak emerges near the zero concurrence, showing a bimodal distribution. In Figure 6.6b, the theoretical histogram for the concurrence is obtained by integrating the theory curve Eq. (6.14) for the probability over small intervals

$\delta c \approx 0.015$. This is to make a fair comparison with the histogram of the experimental data in Figure 6.6c, calculated with a bin size of 0.015. We note that a short delay in the experimental entanglement creation is a result of the cavity ring-up time.

Examining the probability distributions, we see a number of interesting features. First, we note that there are two apparent most likely branches of the concurrence trajectories, one high and one low. This is what we expect given that the qubits may project into an entangled (high) or an unentangled (low) subspace. However, note that for short times, even the low-concurrence branch shows increasing entanglement: the two branches increase in concurrence together before separating into their two paths, which occurs at $t \ll \tau_m$. One might expect that the separation between entangled and unentangled trajectories happens on average at a time near τ_m ; we see clearly from the concurrence probability distribution function that in general, that separation happens much more rapidly.

Finally, we see that the concurrence distribution has a sharp upper bound (shown as a grey dotted curve in Figure 6.6a), which the concurrence cannot exceed. In order to understand why the probability distribution for the concurrence has a sharp upper cut-off at any time, we recall that the density matrix of the two-qubit system, conditioned on the time-integrated readout V_t , is entirely specified by that (random) outcome, together with the initial state, the dephasing rate, and other parameters of the problem according to Eq. (6.2). As can be seen from the inset of Figure 6.6a, the concurrence, plotted as a function of the measured signal V_t , is bounded from above for any fixed time t by some amount we call C_{\max} . Because $C(V_t)$ is determined entirely by V_t , a value of concurrence higher than that maximum (whose value will change as the time increases) cannot physically be realized. Therefore the probability distribution of concurrence has a sharp upper cut-off given by $C_{\max}(t)$. Physically, this indicates that there is an upper limit on how fast entanglement can be created by the continuous measurement in this situation, even for rare events of the measurement process.

The value of C_{\max} evolves based on the interaction between SNR improvement, pure dephasing and decay, and loss-induced measurement dephasing. For the perfectly symmetric case in Eq. (6.11), we can find an analytic solution for the upper bound of the concurrence. Noting that $\cosh(x)$ has its minimum at $x = 0$, $C_{\text{sp},\hat{x}}(V_t)$ must have its maximum at $V_t = 0$. Consequently, the concurrence upper bound is given by

$$C_{\max,\text{sp},\hat{x}}(t) = \frac{e^{-\gamma t} - e^{-S^2 t/s}}{1 + e^{-S^2 t/s}}. \quad (6.15)$$

The behavior of this bound is a result of two competing rates, between the extra dephasing rate γ and a measurement rate S^2/s . Eq. (6.15) increases from zero for small time and decays for long time after reaching its maximum concurrence as seen in Figure 6.6. The maximum possible concurrence for this qubit partial-parity measurement and the time this happens can be obtained from this relation.

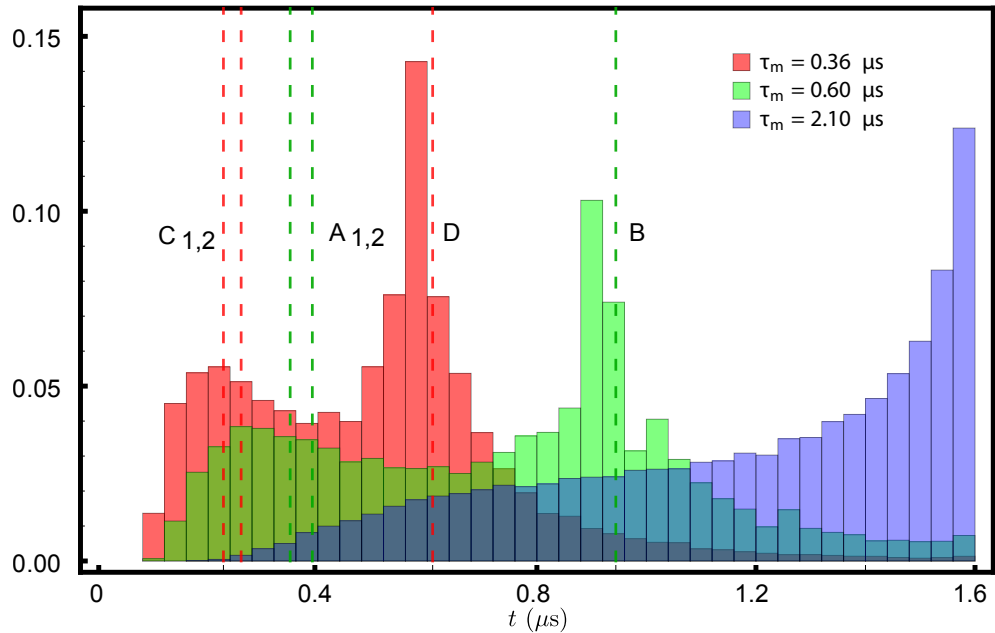


Figure 6.7: Histograms of the time-to-maximum concurrence for individual trajectories for three measurement strengths indicated by the values of τ_m . For the two cases with strong readout powers (shown in red and green histograms), there exists two peaks corresponding to two most likely times to reach their most entangled states. The theoretical prediction of these times are shown as vertical dashed lines labelled as $A_{1,2}, B, C_{1,2}, D$.

6.2.3 Distribution of time to maximum concurrence

In the process of the entanglement generation, there are interesting quantities to investigate such as the maximum concurrence each individual trajectory can reach, and the time it takes to reach the highest value. Using a most-likely-path analysis developed in Ref. [188], we can show that the high- and low- concurrence trajectory branches correspond to projection onto the odd-parity subspace, and onto the $|gg\rangle$ and $|ee\rangle$ states respectively. Therefore, one would expect that there are at least *two* most likely times for the qubit trajectories to reach their maximum concurrences (or their most entangled states).

We show in Figure 6.7 the normalized histograms of time for transmon qubit trajectories to reach their maximum concurrence. The histograms for the $\tau_m = 0.36 \mu\text{s}$ and $0.60 \mu\text{s}$ measurement cases explicitly show double peaks, which agree with the branching of concurrence and the most likely qubit paths in Figure 6.6b-c. The times at which these peaks are located can be theoretically predicted from the time-to-maximum-concurrence of the solutions of the most likely paths; as shown by the vertical dashed lines in Figure 6.7: $A_{1,2}, B$ are the two

most likely times to reach maximum concurrence (for low and high concurrence branches, respectively) for $\tau_m = 0.60 \mu s$, and $C_{1,2}, D$ are the same but for the case with $\tau_m = 0.36 \mu s$. We note that for the weak measurement regime, $\tau_m = 2.10 \mu s$, the bifurcation has not occurred yet during the measurement time $T = 1.6 \mu s$. One would expect to see a branching effect, when the total measurement time is long enough.

6.3 Conclusion

We have investigated the process of entanglement generation between two spatially separated superconducting transmon qubits, and their statistical properties. The entanglement of the two qubits is created as a result of the partial-parity dispersive measurement, via the microwave pulses sequentially interacting with both qubits. The strength of the joint measurement is arbitrary and we have studied three different values of the measurement strength. We examine the concurrence of individual trajectories both as experimentally generated and as theoretically calculated from the quantum Bayesian approach, gradually projecting the two-qubit states to entangled states with high concurrence, and to separable states with zero concurrence. We remind the reader that the Bayesian approach is purely phenomenological: we trade off an accurate microscopic theoretical model for reduced computational intensity in comparison to the stochastic master equation approach. It also can be susceptible to the integration timescale - one must ensure that the data acquisition rate is significantly faster than the underlying system and measurement dynamics in order to fully capture the evolution of the system. Therefore, the effectiveness of the Bayesian approach is somewhat surprising, and remarkable.

Because we can generate arbitrarily many trajectories, we can investigate the statistical properties of the concurrence probability distribution, which immediately shows two interesting and nontrivial properties: a sharp cutoff above which there are rigorously zero concurrence trajectories, and an initial transient period, much shorter than the characteristic measurement time τ_m , during which all trajectories develop significant concurrence. Moreover, we have presented the distributions of the time to the maximum concurrence for individual trajectories, which has clear applications to entanglement optimization. Our ability to reconstruct the full spectrum of possible concurrences for all times and all measurement strengths represents an exceptional level of insight into the internal dynamics underlying an ensemble of states that are entangled by measurement.

We conclude that the accurate tracking of quantum trajectories of a jointly measurement qubit system is possible, and that the physics of the entanglement creation statistics is well described by a quantum trajectory theoretical approach, which produces a concurrence distribution that matches the experiment excellently. Because the Bayesian approach relies only on a well-calibrated experimental system and the calibration protocols are the same for an N-qubit system as for a 2-qubit system, we expect the Bayesian protocol to scale nicely to multiple-qubit systems, enabling continuous trajectory tracking in a multipartite system. Of course, in order to verify the trajectories, one must still perform a complete

tomography. The number of measurements required scales in the worst case as $2^{2n} - 1$ and presents a well-known barrier to the full characterization of a large quantum system. In addition, intra-cavity losses create a technological barrier: we expect the Bayesian approach to perform perfectly well, but the quality of entanglement generated may suffer without the development of low-loss intra-cavity components [191, 192]. The work described here represents an important means to use measurement processes as a control mechanism to entangle remote systems for quantum information processing purposes.

Chapter 7

Deterministic Entanglement via Symmetry-Selective Dissipation Engineering

We have to remember that what we observe is not nature herself, but nature exposed to our method of questioning.

Werner Heisenberg, *Physics and Philosophy*, 1958

To this point, we have used dissipation in the form of a measurement to generate entanglement, and to comprehensively study the dynamics of the entangling back action. However, there is a central limitation to the approach described in Chapters 5 and 6: because we generate entanglement using a *half-parity* measurement, the process is probabilistic: at best, we have a 50% chance to generate entanglement. In this chapter, we develop a dissipative method to generate entanglement *deterministically* - that is, without any post-selection required. Interestingly, this approach relies only on dissipation; as we will see, the very presence of a dissipative mode is sufficient to generate entanglement, with out any need to record the instantaneous cavity output or to track qubit state evolution.

In this chapter, we use an approach that is often called quantum bath engineering, reservoir engineering, or dissipation engineering [58, 59, 194, 195]. Bath engineering explicitly utilizes the coupling of the qubits to their environment as a resource. By designing the density of states in a lossy mode and driving that mode unconditionally, we modify the dissipative environment and dynamically cool to a desired quantum state. We essentially use additional microwave drives to alter the driven ground state of the system into a non-trivial - in this case, entangled - quantum state. Bath engineering in superconducting qubits has resulted in the stabilization of a single qubit on the Bloch sphere [61], a Bell-state of two qubits housed in the same cavity [63], many-body states [62], and non-classical resonator states [64, 196]. Additionally, theoretical proposals have been put forward for dissipative error correction [197–199] and ultimately universal quantum computation [200].

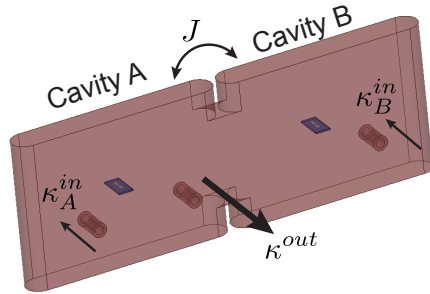


Figure 7.1: To-scale schematic of aperture-coupled cavities, with weakly-coupled input ports κ_i^{in} , strongly-coupled output port κ^{out} , and inter-cavity coupling J .

Bath engineering approaches require careful selection of the bath modes, and often many drives to excite these modes so as to produce a non-trivial ground state. Bath engineering schemes have typically focused on sculpting a density of states conducive to cooling, relying on the conservation of energy between drive, qubit, and resonator modes in multi-photon processes. Here, we harness an additional degree of freedom: the spatial symmetry of the bath, which mandates conservation of parity. We combine both spectral and symmetry selectivity of the bath to provide a scalable protocol for generating on-demand entanglement using only a single microwave drive with a controllable spatial profile. As a demonstration of this scheme, we stabilize two-qubit entangled states in the single-excitation subspace using two tunable 3D transmon qubits [115] in independent microwave cavities. Our results demonstrate the viability of this protocol for stabilizing many-body entangled states in extended arrays.

7.1 Experimental Design and Protocol

The experiments are implemented (Figure 7.1) using two copper waveguide cavities (indexed as A and B) that are aperture-coupled on the transverse (magnetic) axis, with an independent flux-tunable transmon embedded in each cavity. The cavities are fabricated with near-identical resonance frequencies $\omega_{A,B}^c \equiv \omega^c$; the qubits are flux-tuned to resonance at $\omega_{A,B}^q \equiv \omega^q$. The full set of qubit and cavity parameters are tabulated in Table 7.1. The cavities are individually addressable via a weakly-coupled port (κ_i^{in}) through which we apply qubit pulses and bath drives; cavity A has an additional strongly coupled port for read-out. A full elaboration of the cavity design, experimental setup and calibration procedure is provided in Section 7.3.

The unitary dynamics of the system are described by a Hamiltonian that can be subdi-

vided in the rotating wave approximation into qubit, cavity, and drive components:

$$\hat{H}_q = \sum_{i=A,B} \left[\frac{\omega^q}{2} \hat{\sigma}_i^Z + g_i (\hat{\sigma}_i^+ \hat{a}_i + \hat{\sigma}_i^- \hat{a}_i^\dagger) \right] \quad (7.1a)$$

$$\hat{H}_a = \sum_{i=A,B} \left[\omega^c \hat{a}_i^\dagger \hat{a}_i \right] + J (\hat{a}_A \hat{a}_B^\dagger + \hat{a}_A^\dagger \hat{a}_B) \quad (7.1b)$$

$$\hat{H}_d = \sum_{i=A,B} \epsilon_i^d \left[\hat{a}_i^\dagger e^{-i(\omega^d t + \phi_i)} + \hat{a}_i e^{i(\omega^d t + \phi_i)} \right] \quad (7.1c)$$

Here, $\hat{\sigma}_i^{Z,\pm}$ are Pauli operators on the qubits; \hat{a}_i^\dagger are creation operators on the cavity modes; ϵ_i^d are Rabi drives applied at a single frequency ω^d to the respective cavities with a tunable phase ϕ_i ; and g_i are the qubit-cavity couplings. Decay mechanisms not accounted for in these unitary dynamics include qubit energy relaxation (Γ_1) and dephasing (Γ_ϕ), and cavity photon leakage (κ).

The effects of the coupling terms g_i and J manifest in both the qubit and cavity sectors. The central cavity resonances hybridize into symmetric and antisymmetric modes, with the former having a lower frequency (Figure 7.2a). We define these modes as $\omega_\pm^c \equiv \omega^c \mp J$. In the dispersive limit where the qubit-cavity detuning $\Delta_\pm^{\text{qc}} \equiv \omega^q - \omega_\pm^c$ is large in comparison to g , the qubit-cavity coupling creates a photon-mediated XY interaction between the qubits, lifting the degeneracy in the single-excitation subspace [201]. Defining $\delta = J \frac{g_A g_B}{\Delta_+^{\text{qc}} \Delta_-^{\text{qc}}}$, the coupled eigenstates and eigenenergies are given by the following:

$$|T_+\rangle \equiv |ee\rangle \quad \omega_{|T_+\rangle} = 2\omega^q \quad (7.2a)$$

$$|S\rangle \equiv \frac{|ge\rangle - |eg\rangle}{\sqrt{2}} \quad \omega_{|S\rangle} = \omega^q + \delta \quad (7.2b)$$

$$|T_0\rangle \equiv \frac{|ge\rangle + |eg\rangle}{\sqrt{2}} \quad \omega_{|T_0\rangle} = \omega^q - \delta \quad (7.2c)$$

$$|T_-\rangle \equiv |gg\rangle \quad \omega_{|T_-\rangle} = 0 \quad (7.2d)$$

We can then define full basis states of the system including the cavity modes, as

$$|i,j,k\rangle = |n_+\rangle \otimes |n_-\rangle \otimes |\psi_q\rangle \quad (7.3)$$

where n_\pm indexes the Fock state of the respective hybridized cavity modes and $|\psi_q\rangle$ is a coupled qubit state $|\psi_q\rangle \in \{|S\rangle, |T_{0,\pm}\rangle\}$. Figure 7.2b shows the qubit-sector avoided crossing of width $2\delta = 2\pi \times 2.7$ MHz, in quantitative agreement with independently-characterized system parameters.

7.1.1 Entangling protocol

Because the Bell states $|S\rangle$ and $|T_0\rangle$ are eigenstates of the coupled Hamiltonian, it is in principle possible to coherently pulse to these states. However, because the splitting is

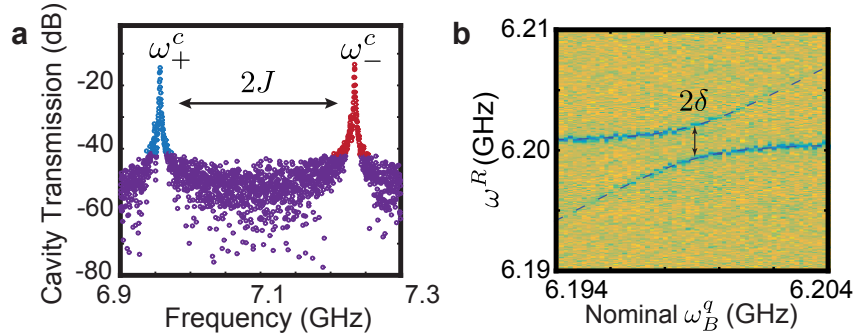


Figure 7.2: Avoided crossings in cavity and qubit sectors. **a:** Transmission spectrum of the coupled cavity modes, showing the symmetric (blue) and antisymmetric (red) peaks. **b:** Pump-probe spectroscopy of the coupled qubit modes, exhibiting an avoided crossing. Cavity B is driven at the symmetric cavity resonance conditioned on the qubit state $|gg\rangle$, and cavity A is driven at a swept frequency ω^R . A dip in transmission (blue) indicates that ω^R is resonant with a qubit mode. The dashed line is a fit of the spectral data, from which we extract δ .

small, a coherent pulse with narrow enough bandwidth to drive selectively to one of these states would need to be several microseconds long, and therefore would be spoiled by qubit decay. Bath engineering, which stabilizes against this decay, provides an alternative means of entanglement in this system.

We aim to stabilize the entangled state of choice ($|S\rangle$ or $|T_0\rangle$) by taking advantage of the distinct symmetries of the bath modes at ω_+^c and ω_-^c . We do this by simultaneously applying a two-photon drive at the individual cavity ports while varying the relative phase between the cavities (Figure 7.3). This work represents a generalization to arbitrary drive phase of the proposal in [201]; a full theoretical treatment (including dynamics) is presented in Section 7.2

Our cooling protocol relies on transitions between the neighboring $n_{\pm} = \{0, 1\}$ rungs of the Jaynes-Cummings ladder. The appropriate drive frequencies are given by

$$\begin{aligned}\omega_{|T_0\rangle}^d(\pm) &= \frac{1}{2} \{ \omega_{\pm}^c + [\tilde{\omega}^q + 2\chi_{\pm}] - \delta \} \\ \omega_{|S\rangle}^d(\pm) &= \frac{1}{2} \{ \omega_{\pm}^c + [\tilde{\omega}^q + 2\chi_{\pm}] + \delta \}\end{aligned}\quad (7.4)$$

where χ_{\pm} is a cross-Kerr term leading to a n_{\pm} -dependent shift in the effective qubit frequency, and $\tilde{\omega}^q$ represents the dressed qubit frequency, which has a power-dependent red shift due to the off-resonant displacement of the cavity field by the drive. Because the qubit-cavity couplings g_i differ, the qubit frequencies shift by different amounts when exposed to the same intra-cavity field. To correct for this, we place the bare qubit frequencies slightly off

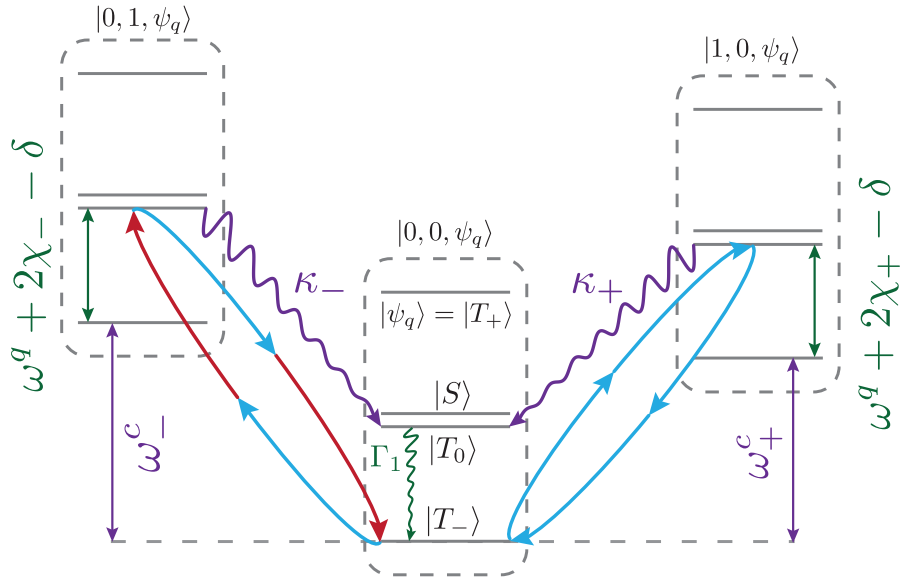


Figure 7.3: Protocol for cooling to $|0,0,T_0\rangle$ via ω_c^- (left) and ω_c^+ (right). Each set of levels outlined in grey represents a rung on the Jaynes-Cummings ladder; the states $|\psi_q\rangle$ are the coupled qubit states. The illustrated drives (arrows) represent $\omega_{|T_0\rangle}^d(\pm)$ from Equation 7.4. Parity conservation requires that if cooling via ω_c^+ , the drive must be overall symmetric (indicated by blue lines), with $\phi = \{0, \pi\}$; if cooling via ω_c^- , the drive must comprise one antisymmetric (red) photon for each symmetric photon. If this condition is met, leakage of cavity photons (purple, κ) brings the system to the entangled state $|0,0,T_0\rangle$. Leakage from the entangled state is dominated by qubit decay (green, Γ_1).

of resonance such that the *dressed* qubit frequencies $\tilde{\omega}_i^q$ are identical. This adjustment is power-dependent, but is on the order of 1 MHz.

When a microwave drive is applied at one of these frequencies, a two-photon transition is created between the un-driven ground state $|0,0,T_-\rangle$ and the resonant partner state $|\psi\rangle \in \{|1,0,S\rangle, |1,0,T_0\rangle, |0,1,S\rangle, |0,1,T_0\rangle\}$. However, when $n_\pm > 0$ the cavities decay stochastically and irreversibly at a rate κ_\pm to $|0,0,T_0\rangle$ or $|0,0,S\rangle$; this is the critical dissipative element in the protocol. There are no transitions from this state that are resonant with the drive. In the case of a T_1 decay, the drive rapidly repumps the qubits, thus creating a stabilized entangled state. A weak off-resonant pumping into $|T_+\rangle$, which is depleted by T_1 rather than by active cooling, sets an upper limit on the cooling rate.

7.1.2 Symmetry-selectivity of protocol

Until now we have only described the *frequency* of the bath drive; we have said nothing about its symmetric properties. Because we can drive the two cavities individually, we are able to continuously tune phase relationship between the drive at Cavity A and that at Cavity B, $\phi \equiv \phi_B - \phi_A$. The phase-dependent properties of the bath engineering protocol can be understood as a parity selection rule that is dynamically generated by altering the drive profile across the cavities. The starting permutation-exchange parity is comprised of the initial qubit state ($|T_-\rangle$, a symmetric state) and the two photons used to generate the drive (which vary from symmetric to antisymmetric with ϕ); the output parity is comprised of the qubit state symmetry and the dissipated photon. Conservation of parity requires that the net parity of the output state respect that of the input state - remembering that the net exchange symmetry of two antisymmetric components is overall even. By varying the relative phase of the drives, we vary the input symmetry and therefore control the parity selection rules. We therefore expect special symmetry points to exist at $\phi = 0$, $\phi = \pi$, and $\phi = \pi \pm \pi/2$, the first two of which represent exchange-symmetric drives, and the final of which are exchange-antisymmetric drives. We will derive this rigorously in Section 7.2.

7.2 Theoretical Treatment of the Bath Drives

In this section, we will provide a thorough theoretical treatment of the coupled cavity system that we study here. We will show the following:

- A coupling Hamiltonian that leads to a degeneracy lifting in both the qubit and cavity sectors;
- A rigorous derivation of the two-photon drive used to generate transitions into the entangled state of our choosing;
- The origin of the parity selection rules discussed above, which fall naturally out of the drive dynamics.

Our experimental setup can be modeled by a pair of two identical two-level systems housed in two identical single-mode optical cavities which can exchange photons via coherent tunneling. Both cavities are driven out of equilibrium by two coherent microwave drives with same frequency ω^d detuned from the cavity frequency. In the frame rotating at ω^d , after a rotating-wave approximation (*i.e.* neglecting counter-rotating terms), the setup is well described by the following Hamiltonian [201]:

$$\hat{H} = \hat{H}_q + \hat{H}_{q,a} + \hat{H}_a, \quad (7.5)$$

with \hat{H}_q , $\hat{H}_{q,a}$, and \hat{H}_a respectively being the qubit, the light-matter coupling, and the photon Hamiltonians given by (we set $\hbar = 1$)

$$\hat{H}_q = \sum_i (\omega^q - \omega^d) \frac{\hat{\sigma}_i^Z}{2}; \quad (7.6a)$$

$$\hat{H}_{q,a} = \sum_i g_i \left[\hat{a}_i^\dagger \hat{\sigma}_i^- + \hat{a}_i \hat{\sigma}_i^+ \right]; \quad (7.6b)$$

$$\hat{H}_a = \sum_i \left[(\omega^c - \omega^d) \hat{a}_i^\dagger \hat{a}_i + \epsilon^d (\hat{a}_i^\dagger e^{i\phi_i} + \text{h.c.}) \right] - J(\hat{a}_A^\dagger \hat{a}_B + \hat{a}_B^\dagger \hat{a}_A). \quad (7.6c)$$

This is identical to the Hamiltonian in Eq. (7.1) in the rotating frame, regrouped for convenience here. The two-level systems are represented by Pauli matrices obeying $[\hat{\sigma}_i^a, \hat{\sigma}_j^b] = 2i\delta_{ij}\epsilon_{abc}\hat{\sigma}_i^c$ where the indices $a, b, c \in \{X, Y, Z\}$, the cavity indices $i, j = A, B$ and $\hat{\sigma}_i^\pm \equiv (\hat{\sigma}_i^X \pm i\hat{\sigma}_i^Y)/2$. All parameters are as defined in Section 7.1; given that physics only depends on the relative phase difference, we shall henceforth work with $\phi \equiv \phi_B - \phi_A$.

Let us neglect the light-matter coupling for a moment. On the qubit side, the eigenstates and eigenenergies of \hat{H}_q in the rotating frame are given by the triplet and singlet states:

$$\begin{aligned} |T_+\rangle &\equiv |ee\rangle, & E_{|T_+\rangle} &= \Delta^{qd}, \\ |S\rangle &\equiv [|ge\rangle - |eg\rangle]/\sqrt{2}, & E_{|S\rangle} &= 0, \\ |T_0\rangle &\equiv [|ge\rangle + |eg\rangle]/\sqrt{2}, & E_{|T_0\rangle} &= 0, \\ |T_-\rangle &\equiv |gg\rangle, & E_{|T_-\rangle} &= -\Delta^{qd}, \end{aligned} \quad (7.7)$$

where $\Delta^{qd} \equiv \omega^q - \omega^d$ is the detuning between the qubits and the drive. On the photonic side, the two coupled cavities being identical, the eigenmodes of the undriven photonic backbone are naturally symmetric and antisymmetric excitations with the creation operators

$$\hat{A}^\dagger \equiv \frac{\hat{a}_A^\dagger + \hat{a}_B^\dagger}{\sqrt{2}} \text{ and } \hat{a}^\dagger \equiv \frac{\hat{a}_A^\dagger - \hat{a}_B^\dagger}{\sqrt{2}},$$

respectively. In this basis, \hat{H}_a reads

$$\hat{H}_a = \Delta_+^{cd} \hat{A}^\dagger \hat{A} + \Delta_-^{cd} \hat{a}^\dagger \hat{a} + \sqrt{2}\epsilon^d [\hat{A}^\dagger \cos(\phi/2) - i\hat{a}^\dagger \sin(\phi/2)] + \text{h.c.}, \quad (7.8)$$

with $\Delta_\pm^{cd} \equiv \omega_\pm^c - \omega^d$.

We will include the total photon leakage outside the cavities with a rate κ_+ for the symmetric mode and κ_- for the antisymmetric mode. The density of states for the antisymmetric and symmetric modes are $\rho_\pm(\omega) = -\text{Im } G_\pm^R(\omega)/\pi$ where the retarded Green's function are given by, in the rotating frame, $G_\pm^R(\omega) = 1/[\omega - \Delta_\pm^{cd} + i\kappa_\pm/2]$. We also include qubit decay and pure dephasing rates, Γ_1 and Γ_φ respectively. These dissipative processes will play a paramount role in the cooling scheme and protocol.

7.2.1 Dynamics

Altogether, the driven-dissipative dynamics of the entire system (qubits and photons) is well described by the following Master equation on the density matrix ρ :

$$\begin{aligned}\dot{\rho} = & -i[\hat{H}, \rho] \\ & + \kappa_+ \mathcal{D}[\hat{A}] \rho + \kappa_- \mathcal{D}[\hat{a}] \rho \\ & + \Gamma_{1,A} \mathcal{D}[\hat{\sigma}_A^-] \rho + \Gamma_{1,B} \mathcal{D}[\hat{\sigma}_B^-] \rho \\ & + \frac{\Gamma_{\varphi,A}}{2} \mathcal{D}[\hat{\sigma}_A^Z] \rho + \frac{\Gamma_{\varphi,B}}{2} \mathcal{D}[\hat{\sigma}_B^Z] \rho,\end{aligned}\tag{7.9}$$

where the Lindblad dissipators are defined as in Chapter 2. This SME includes photon leakage from the two cavity modes at generally non-equal rates; individual qubit decay; and effective qubit dephasing rates. Eq. (7.9) can be solved numerically and $\rho(t)$ rigorously accessed at all times, so in principle writing down the SME provides the final story. In particular, the knowledge of the non-equilibrium steady-state (NESS) density matrix $\rho^{\text{NESS}} = \lim_{t \rightarrow \infty} \rho(t)$ allows us to compute the fidelities of interest. However, the implications of the SME for the dynamics in the qubit sector are not transparent, and we would like to do a more thorough analytical development in order to predict the behavior of the system more intuitively. The results obtained from full numerical computations agree with the experimental results and are also a way to check the validity of the different layers of approximations that are performed in the analytic approach developed below.

7.2.2 Effective driven-dissipative XY model

We now present an analytic approach to compute the steady-state fidelities for the qubit subsystem. In a nutshell, it consists of eliminating the explicit time-dependence of the problem by means of a rotating-wave approximation; treating the light-matter interaction by second-order perturbation theory; linearizing the photonic degrees of freedom around mean-field solutions; and integrating out the remaining photon-fluctuations by means of a Master-equation approach. The result is a set of rate equations that characterize the population of the qubit eigenstates, directly in the steady state, *by-passing* the transient dynamics. The expressions for these rates make transparent the cooling protocol described in Section 7.1.1 and also allow to quantify the expected fidelity of this protocol.

For clarity and relative ease of calculation our approach is presented for a setup without asymmetry in the parameter values, *i.e.*

$$\begin{aligned}g_A &= g_B = g, \\ \Gamma_{1,A} &= \Gamma_{1,B} = \Gamma_1, \\ \Gamma_{\varphi,A} &= \Gamma_{\varphi,B} = \Gamma_\varphi.\end{aligned}$$

Furthermore, the experimental energy scales correspond to the following hierarchies:

$$\begin{aligned}\Delta^{\text{qc}} &\gg g, \\ J &\gg \kappa_{\pm} \gg \Gamma_1 \gg \Gamma_{\varphi}.\end{aligned}$$

In order to make the calculation more transparent, we have made the additional approximation $\omega_+^c = \omega_-^c$ such that $\Delta_+^{\text{qc}} = \Delta_-^{\text{qc}} \equiv \Delta^{\text{qc}}$. This is justified when $\Delta_{\pm}^{\text{qc}} \gg J$, which is not a particularly good approximation for our system (as we will see). However, this approximation does not qualitatively impact the features of the experiment, and it is straightforward to describe the effects of this approximation not holding well. We will do so throughout this section.

The non-linear light-matter coupling in $\hat{H}_{q,a}$ can be eliminated by means of a second-order perturbation theory in g/Δ^{qc} using methods similar to the dispersive approximation derived in Section 4.2.3. In the coupled-cavity case, the good unitary transformation is given by $e^{\hat{c}}$ where

$$\hat{c} = \frac{g}{\sqrt{2}} \left[\frac{\hat{A}(\hat{\sigma}_A^+ + \hat{\sigma}_B^+)}{\Delta_+^{\text{qc}}} + \frac{\hat{a}(\hat{\sigma}_A^+ - \hat{\sigma}_B^+)}{\Delta_-^{\text{qc}}} + \text{h.c.} \right] \quad (7.10)$$

Carrying through the transformation reveals a photon-mediated interaction between the qubits, providing an experimental realization of a two-site transverse-field XY model, as in Eq. (7.2). We furthermore decompose the photon fields into mean fields plus bosonic fluctuations: $\hat{A} \equiv \bar{A} + \hat{D}$, $\hat{a} \equiv \bar{a} + \hat{d}$, $\bar{N}_+ \equiv |\bar{A}|^2$ and $N_- \equiv |\bar{a}|^2$ where, to the lowest order in the light-matter coupling,

$$\bar{A} \simeq \frac{\sqrt{2}\epsilon^d \cos(\phi/2)}{-\Delta_+^{\text{cd}} + i\kappa_+/2} \quad \text{and} \quad \bar{a} \simeq -\frac{i\sqrt{2}\epsilon^d \sin(\phi/2)}{-\Delta_-^{\text{cd}} + i\kappa_-/2}. \quad (7.11)$$

We neglect the resulting quadratic terms in the fluctuations which couple to the qubits, *e.g.* $(g/\Delta^{\text{qc}})^2 \hat{D}^\dagger \hat{D} \hat{\sigma}_i^Z$ [61]. Notice that for fixed drive amplitude ϵ^d at relevant drive frequencies $\omega^d < \omega_{\pm}^c$, the intra-cavity field is larger at the symmetric mode because the detuning is smaller. As a result, the value of ϕ at which $\bar{N}_+ = \bar{N}_-$ is not generically equal to $\pi \pm \pi/2$. Rather, it is given by

$$\tan(\phi/2) = \pm \Delta_-^{\text{cd}} / \Delta_+^{\text{cd}}. \quad (7.12)$$

This is one of the places in which the failure of the approximation $\omega_+^c = \omega_-^c$ has an impact.

To maintain consistency with Schrieffer-Wolff perturbation theory we make sure to work in regimes where the photon fluctuations are relatively small [202]. Altogether, this yields the following Hamiltonian

$$\tilde{H} = \tilde{H}_q + \tilde{H}_{q,d} + \tilde{H}_d, \quad (7.13)$$

with

$$\tilde{H}_q = \sum_i \mathbf{h} \cdot \frac{\boldsymbol{\sigma}_i}{2} - \frac{1}{2} J \left(\frac{g}{\Delta^{\text{qc}}} \right)^2 [\hat{\sigma}_A^X \hat{\sigma}_B^X + \hat{\sigma}_A^Y \hat{\sigma}_B^Y], \quad (7.14)$$

where

$$h_A^x = 2 \frac{g}{\Delta_{qc}} \epsilon^d \cos(\phi/2), \quad h_A^y = -2 \frac{g}{\Delta_{qc}} \epsilon^d \sin(\phi/2), \quad (7.15)$$

$$h_B^x = 2 \frac{g}{\Delta_{qc}} \epsilon^d \cos(\phi/2), \quad h_B^y = 2 \frac{g}{\Delta_{qc}} \epsilon^d \sin(\phi/2), \quad (7.16)$$

$$h_{A,B}^z = \tilde{\Delta}^{qd}, \quad (7.17)$$

$$\tilde{\Delta}^{qd} \equiv \Delta^{qd} + \Delta^{qc} (g/\Delta^{qc})^2 \left[1 + 2 \left(\epsilon^d / \Delta^{cd} \right)^2 \left(1 + \Delta^{cd} / \Delta^{qc} \right) \right]. \quad (7.18)$$

Equation 7.18 is a formulation of the ac-Stark shift on the qubits due to the presence of the drive, such that $\tilde{\Delta}^{qd}$ represents the detuning between the drive tone and the Stark-shifted qubit frequency $\tilde{\omega}^d$. Under the approximation that $\Delta_+^{cd} \approx \Delta_-^{cd}$ it is independent of phase; experimentally it has a slight phase dependence. Thus, we have derived and quantified the effective XY coupling between the qubits that is mediated by the coupling between the cavities.

The eigenstates of \tilde{H}_σ are, to first order in g/Δ^{qc} ,

$$\begin{aligned} |\tilde{T}_+\rangle &= |T_+\rangle + \sqrt{2} \frac{g\epsilon^d}{\tilde{\Delta}^{qd}\Delta^{qc}} [\cos(\phi/2) |T_0\rangle - i \sin(\phi/2) |S\rangle], \\ |\tilde{S}\rangle &= |S\rangle - \sqrt{2}i \frac{g\epsilon^d}{\tilde{\Delta}^{qd}\Delta^{qc}} \sin(\phi/2) [|T_+\rangle - |T_-\rangle], \\ |\tilde{T}_0\rangle &= |T_0\rangle - \sqrt{2} \frac{g\epsilon^d}{\tilde{\Delta}^{qd}\Delta^{qc}} \cos(\phi/2) [|T_+\rangle - |T_-\rangle], \\ |\tilde{T}_-\rangle &= |T_-\rangle - \sqrt{2} \frac{g\epsilon^d}{\tilde{\Delta}^{qd}\Delta^{qc}} [\cos(\phi/2) |T_0\rangle - i \sin(\phi/2) |S\rangle]. \end{aligned} \quad (7.19)$$

The corresponding eigenenergies of \tilde{H}_q are

$$\begin{aligned} E_{\tilde{T}_+} &\simeq \tilde{\Delta}^{qd} + 2(n_+ \chi_+ + n_- \chi_-) \\ E_{\tilde{S}} &\simeq \delta, \\ E_{\tilde{T}_0} &\simeq -\delta, \\ E_{\tilde{T}_-} &\simeq -\tilde{\Delta}^{qd} - 2(n_+ \chi_+ + n_- \chi_-), \end{aligned} \quad (7.20)$$

where $\delta \equiv J(g/\Delta^{qc})^2$ and n_\pm is the Fock state of the relevant coupled cavity mode. The degeneracy between $|S\rangle$ and $|T_0\rangle$ has been lifted by the effective photon-mediated qubit-qubit interaction. The photon fluctuations on top of the coherent mean-field part are governed by the quadratic Hamiltonian

$$\tilde{H}_d = \Delta_+^{cd} \hat{D}^\dagger \hat{D} + \Delta_-^{cd} \hat{d}^\dagger \hat{d}. \quad (7.21)$$

We shall assume that these non-interacting degrees of freedom equilibrate with the outside environment at zero temperature. Furthermore, these photon fluctuations couple to the

qubits via

$$\begin{aligned} \tilde{H}_{q,d} = & \frac{1}{\sqrt{2}} \left(\frac{g}{\Delta_{\text{qc}}} \right)^2 \epsilon^d \left\{ \left(\Delta_{\text{qc}} / \Delta_+^{\text{cd}} + 1/2 \right) [\cos(\phi/2) (\hat{\sigma}_A^Z + \hat{\sigma}_B^Z) - i \sin(\phi/2) (\hat{\sigma}_A^Z - \hat{\sigma}_B^Z)] \hat{D}^\dagger \right. \\ & \left. + \left(\Delta_{\text{qc}} / \Delta_-^{\text{cd}} + 1/2 \right) [\cos(\phi/2) (\hat{\sigma}_A^Z - \hat{\sigma}_B^Z) - i \sin(\phi/2) (\hat{\sigma}_A^Z + \hat{\sigma}_B^Z)] \hat{d}^\dagger \right\} + \text{h.c. } \end{aligned} \quad (7.22)$$

which induces transitions between the eigenstates of \tilde{H}_q .

We integrate the photon-fluctuation degrees of freedom by treating $\tilde{H}_{q,d}$ as a perturbation to \tilde{H}_q and we derive the dynamics of the reduced density matrix of the qubit sector, ρ_q . Under standard assumptions, we obtain the following non-equilibrium steady-state Master equation [201]

$$\partial_t \rho_q^{\text{NESS}} = 0 = -i \sum_k E_k [|k\rangle\langle k|, \rho_q^{\text{NESS}}] + \sum_{kl} \Gamma_{k \rightarrow l} \mathcal{D} [|k\rangle\langle l|] \rho_q^{\text{NESS}}, \quad (7.23)$$

where k and l span the eigenstates of \tilde{H}_q .

The $\Gamma_{k \rightarrow l}$'s are steady-state transition rates between the qubit eigenstates. They read $\Gamma_{k \rightarrow l} = \Gamma_{k \rightarrow l}^b + \Gamma_{k \rightarrow l}^d$ with

$$\Gamma^b = \begin{pmatrix} - & \Gamma_1 & \Gamma_1 & 0 \\ 0 & - & \Gamma_\phi & \Gamma_1 \\ 0 & \Gamma_\phi & - & \Gamma_1 \\ 0 & 0 & 0 & - \end{pmatrix} \quad (7.24)$$

originating from the qubit decay and pure dephasing processes, and with the non-equilibrium drive part given by

$$\Gamma_{k \rightarrow l}^d = 2\pi |\Lambda_{kl}^+|^2 \rho_+ (E_k - E_l + \omega^d) + 2\pi |\Lambda_{kl}^-|^2 \rho_- (E_k - E_l + \omega^d), \quad (7.25)$$

where

$$\Lambda^+ = \lambda_+ \begin{pmatrix} - & \alpha & \beta & 0 \\ \alpha & - & \sin(\phi/2) & \alpha \\ \beta & \sin(\phi/2) & - & \beta \\ 0 & \alpha & \beta & - \end{pmatrix}, \quad \Lambda^- = \lambda_- \begin{pmatrix} - & \beta & \alpha & 0 \\ \beta & - & \cos(\phi/2) & \beta \\ \alpha & \cos(\phi/2) & - & \alpha \\ 0 & \beta & \alpha & - \end{pmatrix}, \quad (7.26)$$

in which

$$\begin{aligned} \lambda_\pm &\equiv \sqrt{2} (g/\Delta_{\text{qc}})^2 \epsilon^d (1/2 + \Delta_{\text{qc}} / \Delta_\pm^{\text{cd}}) ; \\ \alpha &\equiv \sqrt{2} (g/\Delta_{\text{qc}}) (\epsilon^d / \tilde{\Delta}^{\text{qd}}) \cos \phi ; \\ \beta &\equiv \sqrt{2} (g/\Delta_{\text{qc}}) (\epsilon^d / \tilde{\Delta}^{\text{qd}}) \sin \phi . \end{aligned} \quad (7.27)$$

Recall that $\rho_{\pm}(\omega)$ here are the density of states of the bath modes. Matrix rows (columns) are ordered according to $|\tilde{T}_-\rangle$, $|\tilde{T}_0\rangle$, $|\tilde{S}\rangle$, and $|\tilde{T}_+\rangle$ from left to right (top to bottom). Note that in equilibrium, *i.e.* $\epsilon^d = 0$, one has $\Gamma_{k \rightarrow l}^d = 0$.

One can re-write the SME (7.23) as the rate equations governing the population of each of the eigenstates $|k\rangle$ of \tilde{H}_q , $n_k \equiv \langle k| \rho_q |k\rangle$:

$$\frac{dn_k^{\text{NESS}}}{dt} = 0 = \sum_l n_l^{\text{NESS}} \Gamma_{l \rightarrow k} - n_k^{\text{NESS}} \Gamma_{k \rightarrow l}, \quad (7.28)$$

which in conjugation with the conservation law $\sum_k n_k = 1$, provides a direct access to the non-equilibrium steady-state fidelities, by-passing the transient dynamics.

7.2.3 Protocol for generating entanglement

By judiciously tuning the drive frequency amplitude ϵ^d , frequency ω^d , and phase ϕ , one can drive the qubit subsystem to one of the maximally entangled eigen-states. We will discuss the protocol to achieve convergence to the singlet state, $\rho_q^{\text{NESS}} \approx |\tilde{S}\rangle\langle\tilde{S}|$ and compute its fidelity $n_{\tilde{S}}^{\text{NESS}} \equiv \langle\tilde{S}|\rho_q^{\text{NESS}}|\tilde{S}\rangle$. The extension to cooling to the triplet state is straightforward.

By selecting ω^d such that $\omega^d = \omega_-^c + E_{\tilde{S}} - E_{\tilde{T}_-}$, *i.e.* $\omega_{|S\rangle}^d(-) \approx \frac{1}{2} [\omega_-^c + \tilde{\omega}^q + 2\chi + \delta]$, the ρ_- term in the expression of $\Gamma_{\tilde{T}_- \rightarrow \tilde{S}}^d$ given in Eq. (7.25) is maximized to $2/(\pi\kappa_-)$. Therefore, we have a maximal pumping rate

$$\Gamma_{\tilde{T}_- \rightarrow \tilde{S}}^d \approx 400 \left(\frac{g}{\Delta^{\text{qc}}} \right)^6 \frac{|\epsilon^d|^4}{(\Delta^{\text{qc}})^2} \frac{\cos^2(\phi)}{\kappa_-}. \quad (7.29)$$

The mechanism associated with this rate corresponds to a two-photon process in which the incoming energy is used to add a photon in the antisymmetric cavity mode and simultaneously perform a qubit transition from $|\tilde{T}_-\rangle$ to $|\tilde{S}\rangle$ (Stokes scattering). Note that the phase at which $\Gamma_{\tilde{T}_- \rightarrow \tilde{S}}^d$ goes to zero when cooling via the antisymmetric cavity mode is exactly equal to $\pi/2$ in this derivation because we have approximated $\Delta_+^{\text{cd}} \approx \Delta_-^{\text{cd}}$. Experimentally, when this equality does not hold, the phase at which the transition rate goes to zero is given by Equation 7.12.

By selecting ω^d such that $\omega^d = \omega_+^c + E_{\tilde{S}} - E_{\tilde{T}_-}$, *i.e.* $\omega_{|S\rangle}^d(+) \approx \frac{1}{2} [\omega_+^c + \tilde{\omega}^q + 2\chi + \delta]$, it is the ρ_+ term in the expression of $\Gamma_{\tilde{T}_- \rightarrow \tilde{S}}^d$ given in Eq. (7.25) which is maximized. Therefore, the pumping rate is given by,

$$\Gamma_{\tilde{T}_- \rightarrow \tilde{S}}^d \approx 400 \left(\frac{g}{\Delta^{\text{qc}}} \right)^6 \frac{|\epsilon^d|^4}{(\Delta^{\text{qc}})^2} \frac{\sin^2(\phi)}{\kappa_+}. \quad (7.30)$$

Here, it is the symmetric-cavity mode which is used in the Stokes scattering process. Noting that this transition rate goes to zero at $\phi = 0$ and at $\phi = \pi$.

In both cases, if the condition $\Gamma_{\tilde{T}_- \rightarrow \tilde{S}}^d \gg \Gamma_{\tilde{S} \rightarrow \tilde{T}_-}^d = \Gamma_1$ is met, this facilitates a rapid pumping from the ground state $|\tilde{T}_-\rangle$ to the singlet state $|\tilde{S}\rangle$ via Stokes (red-shifted) scattering. One must also avoid off-resonant pumping from $|\tilde{S}\rangle$ to the $|\tilde{T}_+\rangle$ state, labeled as $\Gamma_{\tilde{S} \rightarrow \tilde{T}_+}^d$ here. Altogether, the cooling to the singlet state is achieved with high fidelity whenever the hierarchy

$$\Gamma_{\tilde{S} \rightarrow \tilde{T}_+}^d \ll \Gamma_1 \ll \Gamma_{\tilde{T}_- \rightarrow \tilde{S}}^d \quad (7.31)$$

is obeyed where the off-resonant rate from \tilde{S} to \tilde{T}_+ is given by

$$\Gamma_{\tilde{T}_- \rightarrow \tilde{S}}^d \approx 25(g/\Delta^{qc})^2(|\epsilon^d|^2/\Delta^{qc}J)^2\kappa_- \cos^2(\phi) \quad (7.32)$$

or

$$\Gamma_{\tilde{T}_- \rightarrow \tilde{S}}^d \approx 25(g/\Delta^{qc})^2(|\epsilon^d|^2/\Delta^{qc}J)^2\kappa_+ \sin^2(\phi) \quad (7.33)$$

depending whether the antisymmetric or the symmetric cavity mode is used. The condition (7.31) transparently elucidates that the fidelity is the result of a delicate interplay between drive, cavity decay, qubit dissipation and light-matter coupling. In particular, ϵ^d enters both sides of the inequality above, and thus, large fidelity is obtained in a finite window of the drive strength ϵ^d .

In regimes where all the off-resonant rates are strongly suppressed compared to the other rates involved, *i.e.* $\Gamma_{k \rightarrow l}^d \approx 0$ except from $|\tilde{T}_-\rangle$ to $|\tilde{S}\rangle$, the steady-state population of the singlet state can be approximated to

$$n_{\tilde{S}}^{\text{NESS}} = \langle \tilde{S} | \rho_q^{\text{NESS}} | \tilde{S} \rangle \approx \frac{1}{1 + 2\Gamma_\phi/\Gamma_1} \frac{1 + \Gamma_\phi/\Gamma_1}{1 + \Gamma_1/\Gamma_{\tilde{T}_- \rightarrow \tilde{S}}^d}. \quad (7.34)$$

Therefore, if the hierarchy given in Eq. (7.31) is satisfied, the maximum steady-state fidelity to cooling to the singlet state simply reads

$$n_{\tilde{S}}^{\max} \approx \frac{1}{1 + 2\Gamma_\phi/\Gamma_1}. \quad (7.35)$$

This result clearly highlights that, in contrast to the dephasing rate Γ_ϕ which is detrimental to the protocol, the dissipative qubit decay process is instrumental in achieving large fidelities.

In this section, we have seen that the coupled cavity Hamiltonian that we realize here gives rise to natural exchange symmetries in the dissipation mechanisms. We can purposefully harness these symmetries order to turn a given entangled state into a symmetry-protected state under the bath drive, or conversely, in order to suppress the state. We have rigorously derived the drive dynamics using a master equation approach, and have examined the steady-state populations in order to provide an estimate for the degree of entanglement we expect to produce under a detailed balance picture. The expected entangled state populations can be quite large, if the rates are well tuned: we can hope to generate significant entanglement using this protocol.

Table 7.1: Calibrated experimental parameters

$\omega_+^c/2\pi$	6.9524	GHz
$\omega_-^c/2\pi$	7.2310	GHz
$\omega^q/2\pi$	6.2000	GHz
$\kappa_+/2\pi$	650	kHz
$\kappa_-/2\pi$	820	kHz
$\alpha_A/2\pi$	-210	MHz
$\alpha_B/2\pi$	-210	MHz
$J/2\pi$	139.3	MHz
$g_A/2\pi$	89	MHz
$g_B/2\pi$	98	MHz
$T_{1,A}$	4	μs
$T_{1,B}$	7.2	μs
$T_{2,A}$	2.6	μs
$T_{2,B}$	3	μs

7.3 Full Experimental Calibration

As always, a full calibration of the experimental setup is critical for understanding and predicting the behavior of quantum system under the presence of the bath drives described above. Here, we provide a full accounting of the experimental system design and characterization methodologies. The full set of relevant qubit and cavity parameters include the coupled cavity mode frequencies (ω_\pm^c); the cavity-cavity coupling (J); the qubit anharmonicities (α_i); the qubit-cavity couplings (g_i); the symmetric and antisymmetric cavity linewidths (κ_\pm); and the qubit lifetimes ($T_{1,i}$) and dephasing times ($T_{\phi,i}$). These parameters are tabulated in Table 7.1.

7.3.1 Detailed Experimental Setup

There are three principal drives used in this experiment (Figure 7.4), generated by APSIN and Agilent microwave generators. The readout drive (purple block) is mixed at DC with readout pulses generated by a marker output of a Tektronix AWG520 two-channel arbitrary waveform generator (AWG); amplified to achieve sufficient power for high-power single-shot readout [135]; gated by a fast switch to avoid excessive qubit dephasing from readout leakage; and sent through a LabBrick digital attenuator for fine-tuning of readout amplitude. The readout is combined with qubit and cooling drive pulses that are input at cavity B . Additionally, half of the generator output signal serves as the local oscillator (LO) for an IQ demodulator for homodyne detection of the readout signal.

The qubit drives are generated by a microwave source at 6.075 GHz. This drive serves

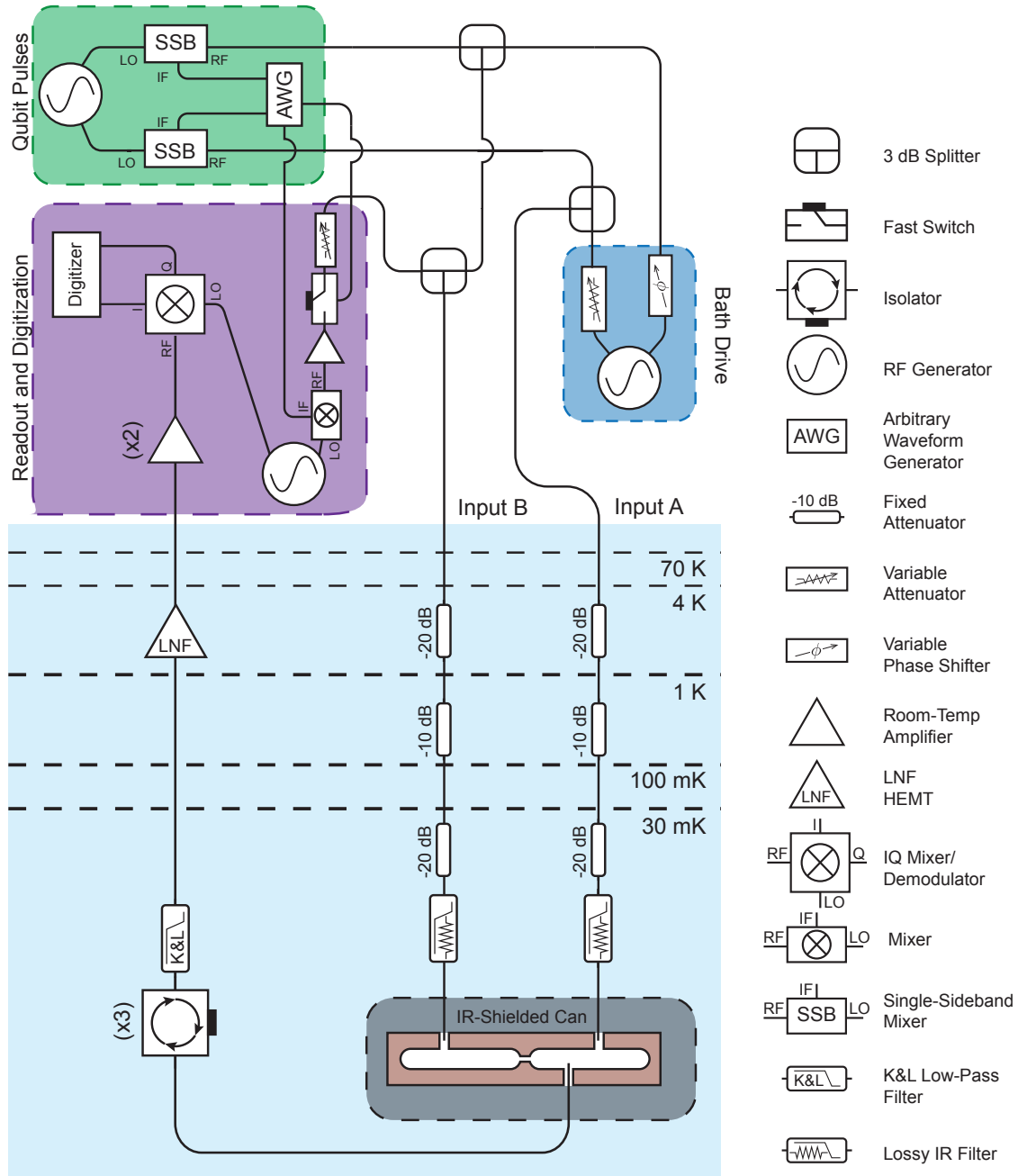


Figure 7.4: Experimental setup. Not shown is an SRS DG535 Digital Delay Generator, which is responsible for triggering the AWG (which generates qubit rotations and gated readout pulses), the cooling drive generator, and the Alazar digital acquisition card.

as the LO for two single-sideband modulators (SSBs) optimized for upper sideband signal output. The two channel outputs of the AWG generate qubit rotation pulses at 125 MHz, with X - and Y - rotations defined by the relative starting phases of the pulses; these are mixed up to 6.2 GHz, the operating frequency of the qubits. Since the qubits are resonant, the difference in path length between the generator and the two cavity inputs is important; we describe the calibration of this angle in the next section. Qubit pulse amplitudes are calibrated via the AWG.

The cooling drive is split in two: the tone that is sent to cavity A passes through a digital attenuator for amplitude balance, and the drive *en route* to cavity B passes through a digital phase shifter to enable facile manipulation of the symmetry of the drives.

The timing of the experiment is controlled by an SRS DG535 digital delay generator (not shown). The DG535 serves three purposes: it gates the cooling drive generator, setting the start and length of the cooling operation; it triggers the AWG to perform qubit rotations and readout; and it triggers the Alazar digital acquisition card to accept input data.

The qubit, cavity, and cooling drives are thermalized to base by 20-, 10-, and 20- dB attenuators thermalized to the 4 K, 1 K, and 30 mK stages of a closed-cycle He-3 dilution refrigerator. At base, they are further filtered for stray infrared (IR) by homemade lossy Eccosorb filters, and input into a secondary copper containment canister containing the coupled cavity system. This can is indium-sealed and coated with further IR-absorbing material. The coupled-cavity output passes through three cryogenic isolators and a commercial K&L low-pass filter at base. It is then amplified by a Low Noise Factory HEMT at 4 K and by two room-temperature amplifiers before being demodulated and digitized.

7.3.2 Coupling of the cavities

The cavities are designed with dimensions of 1.20" x 0.20" x 1.00", with the long axis terminated cylindrically at both ends with a diameter of 0.20 inches (see Figure 7.1). HFSS modal analysis predicts these cavities to have a TE₁₀₁ mode at 7.2 GHz in the absence of a qubit chip. The measured resonator frequency in the presence of a qubit chip is 7.114 GHz at base temperature; the silicon chip lowers the cavity frequency due to the silicon dielectric. The two cavities are machined in HOFC copper and are coupled by an aperture on the transverse axis of width 0.04" and height 0.52". HFSS modeling again predicts that this aperture will couple the two cavity modes with a splitting $2J = 290$ MHz, where the magnitude of J is highly sensitive to the machining tolerances of the cavity. This compares well to $2J = 280$ MHz that we measure experimentally.

Since we cannot separate the cavities to directly measure their bare frequencies, we manually fine-tune the cavity frequencies by referring to the avoided crossing between them, which results in two coupled cavity modes at $\omega_{\pm}^c = \frac{1}{2}(\omega_A^c + \omega_B^c) \mp \frac{1}{2}\sqrt{(\omega_A^c - \omega_B^c)^2 + 4J^2}$. The splitting between the two modes is minimized when the cavities are exactly on resonance ($\omega_A^c = \omega_B^c$). By slightly adjusting the positions of the qubit chips and employing standard S_{21} transmission measurements to find the coupled cavity modes, we minimize this splitting and

thus tune the cavities to resonance. These fine adjustments are on the order of millimeters, and correct for minor inhomogeneities in machining as well as for chip size mismatch. The coupling of the cavities shifts the spatial mode structure of the symmetric and antisymmetric modes, leading to unequal photon decay rates κ_{\pm} via the strongly-coupled output port. We calibrate ω_{\pm}^c and κ_{\pm} via a standard transmission measurement, as shown in Figure 7.2.

7.3.3 Qubit parameters

The qubit-cavity couplings g_i are calibrated by measuring the cross-Kerr nonlinearity of the antisymmetric mode (χ_-) as a function of qubit-cavity detuning. Unlike in Chapter 5, the ratio $|\chi|/\kappa$ is quite large, so the χ -calibration method described in Section 5.4 cannot be used. Instead, we calibrate χ by performing two-tone qubit spectroscopy (as in Figure 7.2b) at a slightly higher readout power, such that the photon number occupation of the measurement mode (ω_-^c , in this instance) is equal to $\bar{n} \approx 0.5$. The experiments are performed in the photon number-resolved limit ($\chi > \kappa, 1/T_2$), such that we can resolve two spectral lines at $\omega^q|_{n_-=0}$ and $\omega^q|_{n_-=1}$, which are split by $2\chi_-$. The splitting χ_- is related to g by

$$\chi_- = \frac{\alpha}{(\Delta_-^{qc} + \alpha)} \frac{g^2}{\Delta_-^{qc}}. \quad (7.36)$$

Here, α is the transmon nonlinearity. We sweep the bias coils that independently govern the qubit frequencies and plot $|2\chi_-|$ as a function of $|\Delta_-^{qc}|$ for both qubits independently. Fitting to Equation 7.36 provides the fit shown in Figure 7.5(c-d) and tabulated in Table 7.1. We extract a fit for both χ_- and for α ; the fits for α are consistent with independent calibrations accomplished by high-power two-tone spectroscopy that drives the two-photon $|g\rangle \rightarrow |f\rangle$ transition. Note that we can also independently calibrate χ_+ , the cross-Kerr coupling to the symmetric cavity mode, and from it extract g_i and α_i ; we do not show these fits here, but they are quantitatively consistent with $\{g_A, g_B\}$ as extracted from the χ_- calibration.

The bare (uncoupled) qubit coherence times T_1, T_2 are calibrated via standard T_1 and Ramsey measurement protocols. These measurements are performed for each qubit at the operating frequency of 6.2 GHz, while the qubit not under test is detuned by 50 MHz and is therefore unaffected by qubit excitation pulses at 6.2 GHz. This detuning is additionally important because when the qubits are on resonance, an excitation in Qubit A will begin to oscillate coherently into Qubit B; we would like to avoid these oscillations in order to characterize the bare qubit parameters. The Purcell limit is set by the photonic density of states at the individual qubit positions, summed over all the normal modes of the system. The qubits couple most strongly to the symmetric and antisymmetric combinations of the TE₁₀₁ modes, but the higher-order modes also participate. The total Purcell decay limit on T_1 considering only the lowest two modes is approximately 8-10 μ s (although we note that the 3D multimode Purcell effect typically reduces Purcell decay when the qubits are red-detuned from the fundamental cavity mode due to interference between the modes).

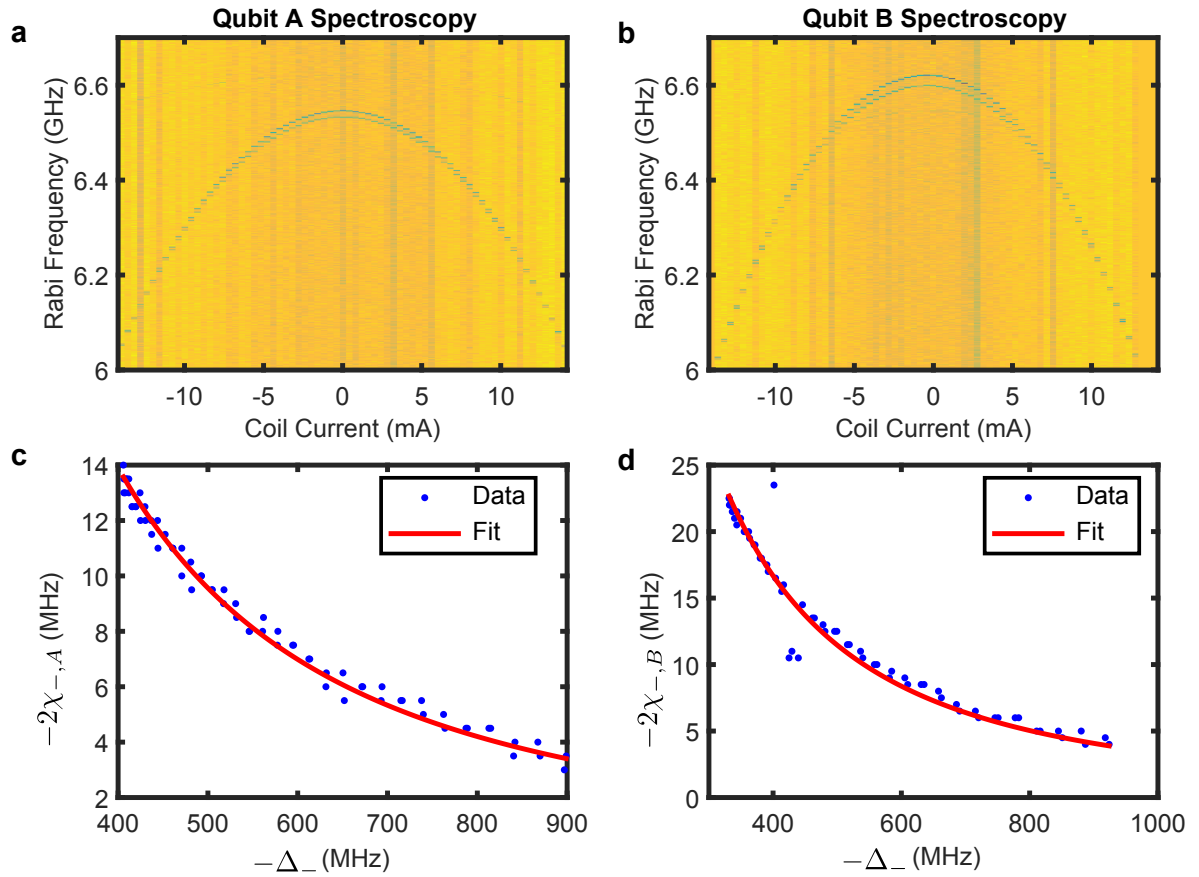


Figure 7.5: Calibration of the qubit-cavity couplings g_i . We sweep the qubit frequency and measure the cross-Kerr nonlinearity of the antisymmetric cavity mode (χ_-) as a function of qubit-cavity detuning for qubit A (panels a, c) and B (panels b, d). This provides a fit of g_i as per Equation 7.36. The outlier points in Panel d result from an avoided crossing as qubit B tunes through qubit A.

The coherence times we achieve are shorter than state-of-the-art 3D transmons, although T_1 is near the single-mode Purcell limit. However, note that T_1 is built as a feature into our cooling protocol, as it depopulates unwanted qubit states, and T_ϕ , the pure dephasing rate that can be extracted from $\frac{1}{T_2} = \frac{1}{T_\phi} + \frac{1}{2T_1}$, is lengthened by a factor of 10 or more by the lifting of the degeneracy between the $|S\rangle$ and $|T_0\rangle$ states when the qubits are tuned to resonance, as we will see in Section 7.4. Lifting this degeneracy implies that the noise that couples these two states is no longer at DC, but is in fact the noise at $\omega = 2\delta$. This effect provides protection from low-frequency noise, and results in an increased effective phase coherence between $|S\rangle$ and $|T_0\rangle$.

7.3.4 Path length calibration

Because the qubits are tuned to degeneracy, the qubit pulses are performed in the same rotating frame. It is critical to properly calibrate the path length difference between pulses arriving at cavities A and B in order to ensure that pulses are performed along common X- and Y-axes. In principle, we can use our knowledge that the higher-energy state to which we cool using our bath engineering scheme is the $|S\rangle$ state, but we also must independently verify this hypothesis.

We follow the methods in the supplementary material of Ref. [26]: noting that the XY Hamiltonian drives oscillations between $|ge\rangle$ and $i|eg\rangle$, we perform a $R_X^{\pi/2}$ rotation on qubit A , along with a $R_\theta^{\pi/2}$ rotation about an arbitrary axis on qubit B , and then allow the coupled qubit state to freely evolve, performing tomographic reconstructions along the way in order to resolve the joint density matrix $\rho(\theta, t)$. When $\theta = \pi/2$ (that is, when we perform a qubit B rotation about the true y-axis), the oscillation amplitudes between $\rho_{ge,ge}$ and $\rho_{eg,eg}$ (that is, the qubit populations in $|ge\rangle$ and $|eg\rangle$, respectively) are maximized, and oscillations are minimized at $\theta = \{0, \pi\}$. We perform a first Rabi oscillation measurement at arbitrary θ ; we then fix the Rabi oscillation time to a maximum of $\rho_{ge,ge}$ and sweep θ . We add a constant phase offset to the qubit rotation pulses applied to qubit B such that the oscillations are suppressed at $\theta = \{0, \pi\}$ (Figure 7.6).

7.3.5 Balancing the cooling drive amplitudes

Achieving symmetry-selective bath engineering in our experimental setup requires a careful calibration of the relative drive amplitudes inside the two cavities, such that the two-photon coherent driving rate is the same for both qubits. If the cavity input amplitudes are not properly balanced, then even when the phases are properly aligned (say, fully symmetrically), the excess drive in one of the cavities means that the decomposition of the total drive into symmetric and antisymmetric drives will have a nonzero amplitude in the undesired component (antisymmetric, in this case). This reduces the symmetry selectivity, so balancing the cavity amplitudes is critical. Quantitatively, this condition is met if $g_A^2 \bar{n}_A = g_B^2 \bar{n}_B$, or

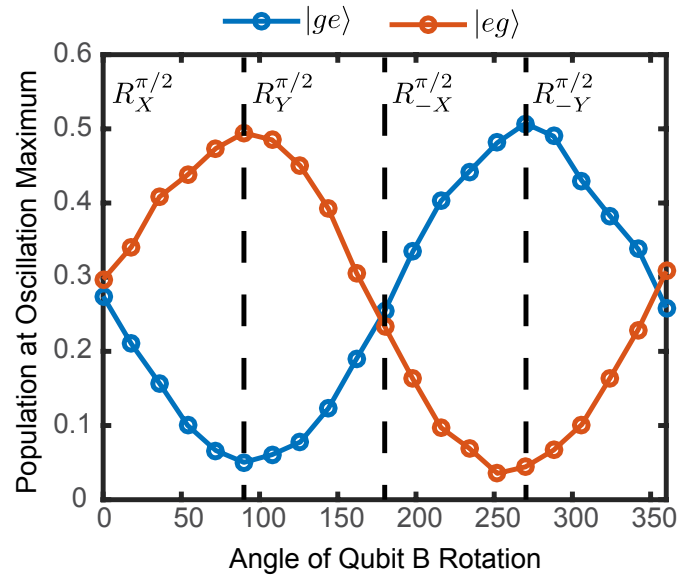


Figure 7.6: Calibration of the relative path lengths of qubit pulses. We prepare the qubits using $R_X^{\pi/2}$ on qubit A and $R_\theta^{\pi/2}$ on qubit B , and fix the free evolution time to $\tau = 400$ ns, where we find a maximum in the oscillation amplitude between $\rho_{\text{ge,ge}}$ and $\rho_{\text{eg,eg}}$. We then vary θ and fix an offset such that the amplitude of oscillation is damped at $\theta = \{0, \pi\}$.

alternatively, if

$$\frac{g_A \sqrt{\kappa_A P_A^{in}}}{\omega^c - \omega^d} = \frac{g_B \sqrt{\kappa_B P_B^{in}}}{\omega^c - \omega^d}. \quad (7.37)$$

where we emphasize that P_i^{in} is a controllable parameter and is related to ϵ_i^d by

$$\kappa_i P_i^{in} = |\epsilon_i^d|^2. \quad (7.38)$$

Several of these parameters are not experimentally measurable - in particular, we cannot independently extract the cavity decay rates κ_i because the resonances that we measure are hybrids of both cavity modes and are affected by both κ_A and κ_B . Therefore, we use pump-probe spectroscopy of the bath engineering drive to directly balance the drive amplitudes (Figure 7.7). We adjust the relative phase of the drives to $\phi = \pi$ such that the drive is fully antisymmetric; we then sweep the cooling drive across the expected frequencies for cooling to both $|S\rangle$ and $|T_0\rangle$. In Figure 7.7, we calibrate the drive amplitudes for cooling via ω_-^c , the antisymmetric cavity mode; in this case, we expect $|T_0\rangle$ to be a forbidden state when the amplitudes are properly balanced. We choose the digital attenuation setting that best suppresses $|T_0\rangle$ as our operating point (as indicated by the arrow). A similar, independent

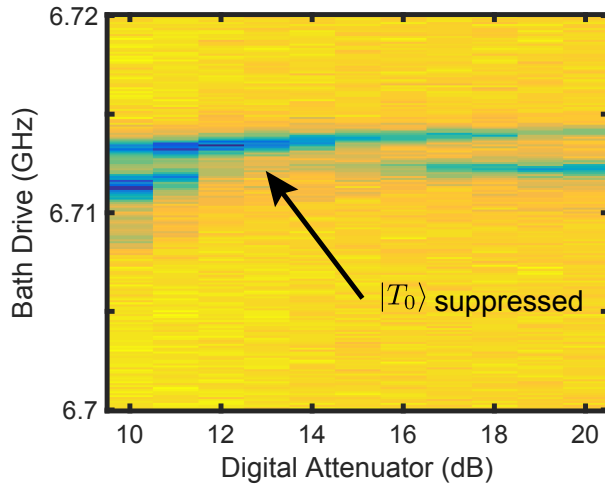


Figure 7.7: Calibration of the relative cooling drive amplitudes. Here, we cool via ω_-^c and fix $\phi = \pi$, such that we expect $|T_0\rangle$ to be fully suppressed when the drive amplitudes are balanced. We perform spectroscopy of the cooling drive while varying the set point of the digital attenuator that controls the relative amplitude of the two cavity drives. Away from the ideal balance, both the upper and the lower cooling lines appear; however, when the drives are balanced (arrow), symmetry selectivity suppresses $|T_0\rangle$. The red-shifting of the cooling frequencies that occurs at lower attenuator settings is due to the AC Stark effect.

calibration is performed when cooling via ω_+^c , in order to account for any potential frequency-dependent losses in the system.

7.3.6 Tomography calibration

Tomography in this experiment is performed, as in Chapter 5, based on the method outlined in Chow et al. [181]. Because the cavity bandwidth is narrow, we use high-power readout [135] that is optimized to discriminate the joint ground state $|gg\rangle$ from the other three eigenstates of the system. Thus, unlike in the measurement-induced entanglement and trajectories experiments, we do *not* have access to the $|ee\rangle$ population: we must base our tomography only on readout of the $|gg\rangle$ state. Also note that because high-power readout is a latching measurement that involves flooding the cavities with tens of thousands of photons, it is not possible to use it to do a ground-state heralding measurement. Thus, in these experiments we have no post-selected state initialization.

The high-power readout accomplishes a measurement of the form $\mathcal{M} = \beta_{II}\hat{\sigma}^{II} + \beta_{IZ}\hat{\sigma}^{IZ} + \beta_{ZI}\hat{\sigma}^{ZI} + \beta^{ZZ}\hat{\sigma}_{ZZ}$, where the β -coefficients are calibrated using the double-Rabi oscillation method in the previous reference. We perform a set of 30 (overspecified) positive and negative

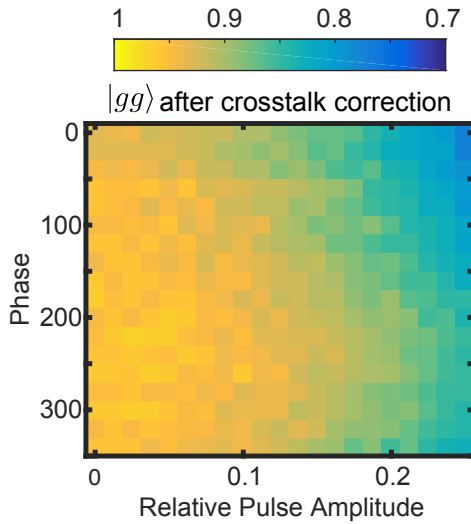


Figure 7.8: Calibration of the qubit pulse cross-talk. We apply the equivalent of a π -pulse to Cavity A while Qubit A is detuned, and implicitly measure the effect on Qubit B by performing crosstalk correction pulses at swept relative amplitude (x-axis) and phase (y-axis). The point at which the ground-state population is maximized (yellow) indicates that the cross-talk rotation has been corrected. The color scale indicates the ground-state population.

qubit rotations in order to fully determine the 15 degrees of freedom of the density matrix, and use maximum likelihood estimation to infer the trace-normalized, positive-semidefinite density matrix that is consistent with our tomographic data. In order to accomplish single-qubit pulses despite the resonant coupling of the qubits, we apply 32-ns qubit pulses such that the pulse envelope is broader than the qubit splitting, enabling single-qubit rotations. While the qubit coupling induces mixing between the $|ge\rangle$ and $|eg\rangle$ states, it does not affect the $|gg\rangle$ population from which we infer the density matrix; this limits the effect of the qubit coupling on tomographic reconstruction.

Finite-element simulations show that a pulse at the qubit frequency, when applied to a given cavity, remains localized in that cavity and does not propagate to the neighboring cavity. However, we would like to calibrate *in-situ* the qubit pulse cross-talk (i.e. the amount by which a rotation on Qubit A will also rotate Qubit B). To do so, we calibrate a π -pulse on Qubit A, and then detune it by 50 MHz so that the pulse does not in fact affect the state of Qubit A. We then (Figure 7.8) apply compensating pulses to Qubit B at a swept amplitude and frequency. When the $|gg\rangle$ population is maximized (yellow), the crosstalk has been undone; this provides a direct calibration of the crosstalk. We see a slight phase-dependence in the data, indicating that the crosstalk occurs at a relative phase of 250° ,

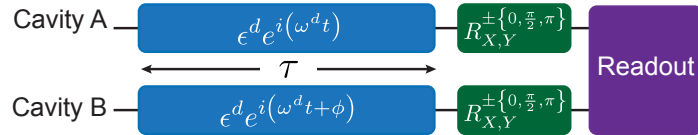


Figure 7.9: Pulse sequence. A bath tone (blue) is applied, for varying time τ and with varying relative phase ϕ ; a set of tomography pulses are performed, followed by a readout in order to reconstruct the density matrix.

and estimate that the amplitude of the crosstalk is less than 5%. The fact that we do both positive and negative tomographic rotations partially corrects for this crosstalk, as the two sets of rotations will induce opposite cross-talk.

7.4 Experimental Implementation of the Bath Engineering Protocol

With a fully calibrated experimental system, we can now proceed to realizing the symmetry-selective bath engineering protocol. The pulse sequence used to implement the protocol is shown in Figure 7.9. We apply simultaneous, amplitude-balanced drives with a relative phase ϕ to the input of the cavities. In a first experiment, we apply the bath drive for a fixed interval of $\tau = 10\mu\text{s}$, and sweep the drive frequency (ω^d , y -axis) and relative phase (ϕ , x -axis). We then reconstruct the joint qubit density matrix ρ using tomographic reconstruction techniques [26, 181] based on high-power readout [135]. Figure 7.10 shows the fidelity to $|S\rangle$ (red) and to $|T_0\rangle$ (blue), where the fidelity to a target state $|\psi\rangle$ is given by $\mathcal{F} = \langle\psi|\rho|\psi\rangle$. We use fidelity here instead of concurrence because, unlike in Chapters 5 and 6, we are specifically concerned here not with just the quality of the entanglement, but the specific entangled state generated. In this context, a fidelity $\mathcal{F} \geq 0.50$ corresponds to nonzero concurrence, and therefore is a confirmation of entanglement.

The *symmetry-selective* aspect of the protocol manifests at three symmetry points. In particular, there are four bands in which the protocol achieves entanglement, corresponding to the frequencies in Equation 7.4: entanglement via ω_+^c (ω_-^c) occurs at $\omega^d = 2\pi \times 6.572$ (6.713) ± 0.0013 GHz. However, at $\phi = 0, \phi = \pi$, and $\phi \sim 180^\circ \pm 67^\circ$, the resonant transitions are selectively suppressed for one of the target states, and the suppressed states are reversed between the ω_+^c and ω_-^c cooling bands. At these symmetry points, the frequency-crowding of the qubit spectrum is alleviated: it is effectively lifted from δ to J , representing two orders of magnitude of improvement.

Under an even-parity drive, when the cooling drive is comprised of two symmetric or two antisymmetric photons (*i.e.* $\phi = 0$ or π), we can only cool to the qubit state whose parity is

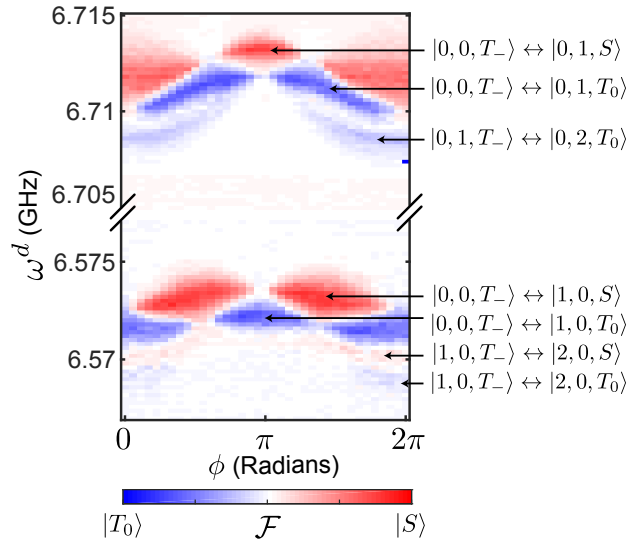


Figure 7.10: Symmetry- and frequency-selective bath engineering. We plot $\mathcal{F}_{|S\rangle} - \mathcal{F}_{|T_0\rangle}$ such that $|S\rangle$ is red and $|T_0\rangle$ is blue. At the symmetry points $\phi = 0, \phi = \pi$, and $\bar{n}_+ = \bar{n}_-$, the drive is both frequency- and symmetry-selective. The $|\psi_1\rangle \leftrightarrow |\psi_2\rangle$ notation indicates the transition with which the drive is resonant for the labelled band. Transitions between higher cavity occupation states are red-detuned by $\chi_+ = -2\pi \times 2.5$ MHz for the lower-frequency bands, and $\chi_- = -2\pi \times 1.4$ MHz for the higher-frequency bands.

the same as the cavity output photon. Indeed, population in the antisymmetric $|S\rangle$ is fully suppressed in the lower (symmetric) band at $\phi = \{0, \pi\}$, and $|T_0\rangle$ is similarly suppressed in the upper band (where the scattered photon is antisymmetric). There also exists a relative phase at which the drive is comprised equally of symmetric and antisymmetric photons, leading to an overall odd-parity drive. This phase is $\phi \approx 180^\circ \pm 67^\circ$ in these experiments, which differs from $\pi \pm \pi/2$ because of the detuning $\omega_+^c \neq \omega_-^c$, and is well-predicted by Equation 7.12. At these phases, the parity of the target qubit state must be *opposite* that of the cavity output photon. Cooling to $|T_0\rangle$ occurs only via the antisymmetric mode in this case, and cooling to $|S\rangle$ occurs via the ω_+^c mode. These symmetry restrictions are lifted for generic ϕ , in which case both cavity modes can be equivalently used to target $|T_0\rangle$ or $|S\rangle$, and only energy conservation of input and output photons is required. Thus, simply by tuning a readily-adjustable drive parameter, we turn a given entangled state from a forbidden into a symmetry-protected state.

The undulation in the cooling bands is an effect of the phase-dependence of $\tilde{\omega}^q$, due to the detuning between ω_+^c and ω_-^c : a drive of fixed amplitude is closer in frequency and therefore

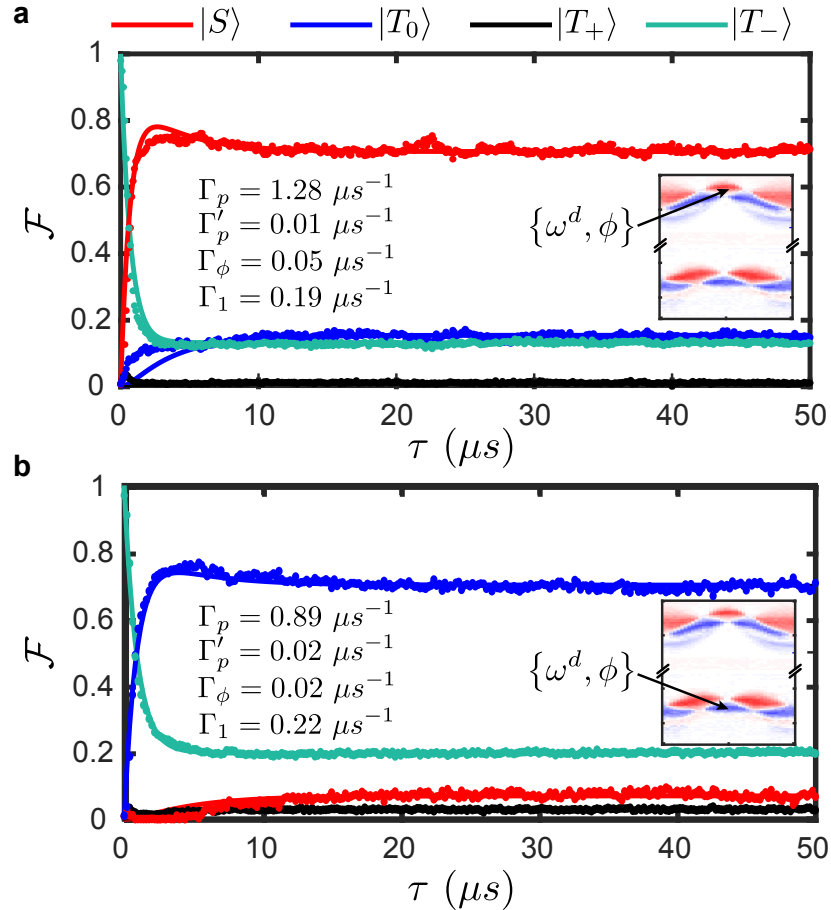


Figure 7.11: Cooling dynamics. (a) We prepare $|S\rangle$ using $\phi = \pi$ by cooling via the antisymmetric cavity mode (inset). (b) Similarly, we prepare $|T_0\rangle$ using $\phi = \pi$ via the symmetric cavity mode. In both cases, we fix ϕ and ω^d ; apply the drive for time τ ; and then tomographically reconstruct the resultant joint qubit state. The experimental data are represented as dots; solid lines are fits to a coupled rate equation with rates as noted. The preparation of $|S\rangle$ reaches maximum entanglement in approximately $3.5 \mu s$; $|T_0\rangle$ reaches maximum entanglement in $3.8 \mu s$.

fore coupled more strongly to the lower-frequency symmetric mode, resulting in a stronger AC Stark shift at $\phi \approx 0$. The broadening of the cooling spectrum at $\phi = 0$ represents the same phenomenon, this time manifesting as power-broadening. The faint red-shifted cooling bands, detuned by χ_{\pm} , represent cooling between higher photon-number subspaces, as labeled.

By moving to the time-domain (Figure 7.11), we can resolve the effects of the several dynamical rates that govern the non-equilibrium steady state. For each experiment we fix ω^d and ϕ , and apply the bath drive for a variable time τ , again finally tomographically reconstructing the joint qubit state. We utilize $\phi = \pi$ such that parity rules require cooling to $|S\rangle$ ($|T_0\rangle$) via ω_-^c (ω_+^c). The dominant rates in the system are Γ_p , the pumping rate from $|T_-\rangle$ to the target state; Γ'_p , a weak off-resonant pumping to $|T_+\rangle$; Γ_1 , the spontaneous decay rates of the qubits; and Γ_ϕ , the effective dephasing rate between $|S\rangle$ and $|T_0\rangle$. Provided that we meet the inequality $\Gamma_\phi, \Gamma'_p < \Gamma_1 < \Gamma_p$, we expect the steady-state population to be entangled. We fit the data to a coupled rate equation and extract the pumping and decay rates. The quality of the fit to a simple exponential indicates that the dynamics of this system are dominated by incoherent processes, which is consistent with $\kappa_\pm \gg \Gamma_p$: in this regime, photons stochastically leak from the cavity much more quickly than the drive is able to repopulate them.

The steady state saturates to the entangled state of choice after a transient ring-up (dominated by Γ_p) and a small overshoot (related to Γ_ϕ). The steady-state fidelities are $\mathcal{F}(|T_0\rangle) = 0.70$ and $\mathcal{F}(|S\rangle) = 0.71$, well beyond the threshold $F = 0.5$ indicative of quantum entanglement. The fidelity loss is dominated by residual $|T_-\rangle$ population and by transitions to the entangled state of opposite symmetry $|T_0\rangle \leftrightarrow |S\rangle$. Increasing Γ_p in principle helps to depopulate the initial $|T_-\rangle$ state; however, increasing the pump power leads to power-broadening of both the desired transition and of the off-resonant pumping to $|T_+\rangle$. Since $|T_+\rangle$ decays equally to $|S\rangle$ and to $|T_0\rangle$, this creates a drive-dependent dephasing that sets an upper limit on the pumping rate. In an on-chip implementation with currently-accessible qubit coherence times, this protocol can be expected to produce on-demand entanglement with fidelity in excess of 0.90.

7.5 Discussion

In this chapter, we have demonstrated symmetry-selective bath engineering, harnessing both the spatial symmetry and the density of states of the dissipative environment to achieve and preserve on-demand entanglement. The engineered symmetries in our system distinguish it from the two-qubit bath engineering experiment in Ref. [63], where cooling to $|S\rangle$ is achieved by utilizing far-detuned qubits in a single cavity; stabilizing entanglement in this system required six microwave drives, and only $|S\rangle$ was accessible. In our implementation, the resonant construction of the photonic lattice imprints itself onto the effective qubit Hamiltonian and lifts the degeneracy in the single-excitation subspace. The lifting of this degeneracy allows us to reduce the number of required drives from six to one, and the use of separate cavities allows us to easily modify the spatial profile of this drive in order to capitalize on the permutation symmetries of the coupled cavity resonances.

Our work demonstrates that engineering symmetries of a dissipative environment provides a powerful route to quantum control. Furthermore, this protocol is highly amenable to scaling beyond bipartite entanglement into multiple qubits and cavities. In this case, the

symmetric and antisymmetric combinations generalize to highly-entangled quasi-momentum eigenstates, represented by many-body W -states [203]. Critically, adjusting the phase relationships of a single driving tone applied across the lattice still provides symmetry selectivity, allowing for efficient stabilization of many-body entanglement in an extended system. The ease of access to single-qubit manipulation and readout makes this experimental geometry a promising testbed for transport and studies of high-symmetry (e.g. quadrupole) states and long-range entanglement in Bose-Hubbard systems and other quantum lattices.

Chapter 8

Conclusions and Outlook

A scientist in his laboratory is not a mere technician: he is also a child confronting natural phenomena that impress him as though they were fairy tales.

Marie Curie

In this dissertation, we have explored a number of ways in which dissipation can serve as a useful tool for generating quantum resources in superconducting cQED systems. We first engineered a half-parity measurement that, when properly tuned, probabilistically generates entanglement between remote superconducting qubits. This experiment demonstrates that coherent quantum information can be efficiently transferred along ordinary microwave cables, which is a crucial capability for any potential quantum network with superconducting qubits at the nodes. We also performed a deep dive into this half-parity measurement by unravelling individual quantum trajectories in the system. This allowed us to explore the full distribution of stochastic trajectories that lead the system into an entangled state or into one of the two unentangled states, and to study both the most likely path and the most likely time to entanglement. Through these sets of experiments, we developed a deeper understanding the interplay between measurement and dissipation: the measurement signal we collect allows us to generate entanglement, but the signal that is lost along the way leads to dissipation that destroys that entanglement.

We then continued to demonstrate a purely dissipative means of generating entanglement in a two-qubit, two-cavity system. By directly coupling the cavities to generate a dissipative bath with opposite spatial symmetries imprinted on bath modes at distinct frequencies, we preserve the ability to perform individual qubit manipulations while still coupling the qubits to common dissipative modes. We drive the bath with a single microwave tone with a controllable spatial profile in order to achieve symmetry-enhanced dissipative stabilization of an odd-parity entangled state of choice. This represents a first demonstration of a scalable protocol for generating multipartite entangled states.

Throughout these experiments, we have grown to appreciate that dissipative processes need not be the enemy of a coherent quantum system. When understood and utilized

properly, dissipation can serve a unique role in both generating and stabilizing entanglement. The half-parity measurement that we perform in the remote entanglement experiments uses a propagating coherent state to carry information from one qubit to the next, generating an effective interaction between the qubits where no local entangling interactions exist. In fact, entanglement in this system is made possible precisely by the measurement. In the bath engineering experiments, the interaction between two cavity modes creates an effective interaction between the qubits; driving those modes allows us to generate entanglement on-demand, and stabilize it for arbitrary time. These complementary techniques demonstrate the power and flexibility of tailored dissipation in the generation of quantum resources.

8.1 Extensions of Measurement-Induced Entanglement

There are a number of interesting follow-on experiments that one could imagine for the remote measurement-induced entanglement work. The most interesting are targeted at making the experiment amenable to deterministic, rather than probabilistic entanglement. If one could precisely tune the phase shifts at the cavities to $\pi/2$, the measurement would implement a full-parity measurement. Zero phase shift would correspond to projection onto the odd-parity subspace, and a π -phase shift would correspond to projection onto the even-parity subspace. The technical challenge to this approach is that, as the phase shift increases, the dephasing rate for a fixed cavity displacement increases as well, such that the measurement induced dephasing caused by losses between the cavities becomes a more significant experimental hurdle. Ongoing efforts to engineer a lossless circulator [191, 204] would be an important enabling technology for such an experiment.

Moreover, our characterization of the state of the joint system under continuous measurement suggests the feasibility of future *continuous* feedback stabilization of entanglement [171, 177, 178, 183], even when using a half-parity measurement. These proposals apply a drive to the qubits that is proportional to the homodyne current. If the signal fluctuations indicate that the system is projecting toward $|gg\rangle$, a positive rotation is applied to repopulate the entangled subspace; if the signal indicates projection toward $|ee\rangle$, a negative rotation is applied. This stabilizes the two-qubit system in the odd-parity subspace. In addition, the proposal in Ref. [177] includes a means not only for stabilizing the population in the odd-parity subspace, but also for stabilizing the phase *within* that subspace. This protocol is a particularly attractive option because it can correct for dephasing as well as for qubit decay.

Finally, the cascaded qubit chain can be extended to the multi-qubit domain. In the three-qubit case, if we are able to engineer all three phase shifts to be identical, then we can probabilistically generate W-states, which share a single excitation amongst all three qubits. In addition, it is often possible (given appropriate asymmetries in the system) to engineer a combination of phase shifts such that the phase shifts for $|gge\rangle$ and $|eeg\rangle$ coincide;

we can then perform a bit flip on the final qubit to generate the GHZ state. Again, however, inter-cavity losses will create a dissipation-induced dephasing that limits the applicability of this protocol in the absence of lossless directional elements [191, 192]. An additional source of complication is the exponentially increasing number of measurements required in order to perform a full tomographic reconstruction: the number of free parameters in an n -qubit density matrix scales as $2^{2n} - 1$, which rapidly becomes intractable. However, there are a number of proposals for continuous-measurement based tomography and compressed sensing [205–207] that may ameliorate the scaling issue.

Because the Bayesian approach is phenomenological, extends naturally from the single-qubit Bayesian formalism, and has been validated in a two-qubit cascaded measurement, we expect it to perform well in a multipartite system (conditioned on a well-calibrated measurement chain). However, one always needs a model for the effective cascaded dynamics originating from a microscopic understanding of the system in order to justify and validate the extension of the phenomenological Bayesian model. This is particularly true as the expanse of off-diagonal elements becomes larger, or for experiments in which there are significant or interesting dynamics outside of the target subspace.

8.2 Further Applications of Dissipation-Induced Entanglement

There are a number of interesting extensions of the pure dissipation-induced entanglement scheme. When moving to the coupled-cavity architecture, we gave up the remote aspect of our system in order to gain determinism in the entanglement protocol. The reason for this is that, if there is significant spatial distance between the cavities, the cable used to connect the two cavities can no longer be treated as a lumped element. The cavities act as mirrors at the ends of the connecting cable, setting up a third resonant mode that mediates the qubit coupling and leads generally to a reduction in the coupling. However, there is an interesting recent proposal that overcomes this challenge, and enables bath engineering of entanglement in fully remote cQED systems [208]. This is a promising approach because it allows us to couple determinism with spatial separation in the generation of entanglement. While this system would not be appropriate for loophole-free tests of Bell’s inequalities - the protocol relies on the exchange of photons between the two cavities - it nevertheless could be a useful approach for distributing entanglement in a multiple-qubit device of arbitrary size.

In addition, the symmetry-selective bath engineering scheme we describe in Chapter 7 is itself well-suited for scaling to larger system size [203]. The protocol relies on spatial symmetries for entangled state selectivity, which allows us to utilize only a single measurement tone with a controllable spatial profile in order to generate an entangled state of our choosing within the odd-parity subspace. We note that the entangled states $|S\rangle$ and $|T_0\rangle$ are in fact many-body W-states for a two-qubit system. Our protocol scales naturally to a chain of multiple qubits and cavities. The cavity-mediated coupling leads to a lifting of the degener-

acy between the W-states in the single-excitation subspace; by driving the bath modes with a tone at the appropriate frequency and with a well-adjusted spatial profile, we can stabilize the W-state of our choosing. This opens the door to studying driven-dissipative dynamics in many-body systems, which is a subject of great theoretical interest. More broadly, the approach of purposefully designing symmetry-based selection rules in a dissipative bath is quite general, and will provide a useful tool for tailoring cavity-induced qubit interactions to simulate a Hamiltonian of interest.

Bibliography

1. J. I. Cirac, P. Zoller, *Physical Review Letters* **74**, 4091–4094 (1995).
2. R. Blatt, D. Wineland, *Nature* **453**, 1008–1015 (2008).
3. D. Leibfried, R. Blatt, C. Monroe, D. Wineland, *Reviews of Modern Physics* **75**, 281–324 (2003).
4. D. Wineland *et al.*, *Fortschritte der Physik* **46**, 363–390 (1998).
5. J. T. Barreiro *et al.*, *Nature* **470**, 486–91 (2011).
6. C Monroe, J Kim, *Science* **339**, 1164–9 (2013).
7. H Mabuchi, A. C. Doherty, *Science* **298**, 1372–7 (2002).
8. J. M. Raimond, M. Brune, S. Haroche, *Reviews of Modern Physics* **73**, 565–582 (2001).
9. S. Haroche, J.-M. Raimond, *Exploring the Quantum: Atoms, Cavities, and Photons* (Oxford University Press, 2006).
10. M. Saffman, T. G. Walker, K. Mølmer, *Reviews of Modern Physics* **82**, 2313–2363 (2010).
11. I. Bloch, J. Dalibard, S. Nascimbène, *Nature Physics* **8**, 267–276 (2012).
12. V. Dobrovitski, G. Fuchs, A. Falk, C. Santori, D. Awschalom, *Annual Review of Condensed Matter Physics* **4**, 23–50 (2013).
13. J. Wrachtrup, F. Jelezko, *Journal of Physics: Condensed Matter* **18**, S807–S824 (2006).
14. J. R. Petta *et al.*, *Science* **309** (2005).
15. R. Hanson, L. P. Kouwenhoven, J. R. Petta, S. Tarucha, L. M. K. Vandersypen, *Reviews of Modern Physics* **79**, 1217–1265 (2007).
16. R. Hanson, D. D. Awschalom, *Nature* **453**, 1043–1049 (2008).
17. R. J. Thompson, G. Rempe, H. J. Kimble, *Physical Review Letters* **68**, 1132–1135 (1992).
18. T. Aoki *et al.*, *Nature* **443**, 671–674 (2006).
19. Y. Kubo *et al.*, *Physical Review Letters* **105**, 140502 (2010).
20. M. H. Devoret, A. Wallraff, J. M. Martinis, arXiv: 0411174 [cond-mat] (2004).

21. J. Clarke, F. K. Wilhelm, *Nature* **453**, 1031–1042 (2008).
22. M. H. Devoret, R. J. Schoelkopf, *Science* **339**, 1169–74 (2013).
23. A. Blais, R.-S. Huang, A. Wallraff, S. Girvin, R. Schoelkopf, *Physical Review A* **69**, 062320 (2004).
24. A. Wallraff *et al.*, *Physical Review Letters* **95**, 060501 (2005).
25. K. W. Murch, R. Vijay, I. Siddiqi, in *Superconducting Devices in Quantum Optics*, pp. 163–185.
26. M. Steffen *et al.*, *Science* **313**, 1423–5 (2006).
27. R. C. Bialczak *et al.*, *Nature Physics* **6**, 409–413 (2010).
28. L DiCarlo *et al.*, *Nature* **460**, 240–4 (2009).
29. J. M. Chow *et al.*, en, *New Journal of Physics* **15**, 115012 (2013).
30. S. Poletto *et al.*, *Physical Review Letters* **109**, 240505 (2012).
31. J. M. Martinis, A. Megrant, arXiv: 1410.5793 (2014).
32. O. Dial *et al.*, *Superconductor Science and Technology* **29**, 044001 (2016).
33. C. Rigetti *et al.*, *Physical Review B* **86**, 100506 (2012).
34. F. Yan *et al.*, arXiv: 1508.06299 (2015).
35. R. Barends *et al.*, *Physical Review Letters* **111**, 080502 (2013).
36. Y. Nakamura, Y. A. Pashkin, J. S. Tsai, *Nature* **398**, 786–788 (1999).
37. K Geerlings *et al.*, *Applied Physics Letters* **100**, 192601 (2012).
38. C. Wang *et al.*, *Applied Physics Letters* **107**, 162601 (2015).
39. Y. Chen *et al.*, *Physical Review Letters* **113**, 220502 (2014).
40. Z. Chen *et al.*, *Applied Physics Letters* **104**, 052602 (2014).
41. M. D. Reed *et al.*, *Applied Physics Letters* **96**, 203110 (2010).
42. A. D. Córcoles *et al.*, *Applied Physics Letters* **99**, 181906 (2011).
43. A. Kamal *et al.*, arXiv: 1606.09262 (2016).
44. J. M. Martinis, M. R. Geller, *Physical Review A* **90**, 022307 (2014).
45. C. M. Quintana *et al.*, *Applied Physics Letters* **105**, 062601 (2014).
46. S Ohya *et al.*, *Superconductor Science and Technology* **27**, 015009 (2014).
47. J. Chang *et al.*, *Applied Physics Letters* **103**, 012602 (2013).
48. A. Bruno *et al.*, *Applied Physics Letters* **106**, 182601 (2015).
49. J. M. Sage, V. Bolkhovsky, W. D. Oliver, B. Turek, P. B. Welander, *Journal of Applied Physics* **109**, 063915 (2011).

50. J. Preskill, *Proceedings of the Royal Society A: Mathematical, Physical and Engineering Sciences* **454**, 385–410 (1998).
51. M. Nielsen, I. Chuang, *Quantum Computation and Quantum Information* (Cambridge University Press, Cambridge, UK, 2000), p. 702.
52. A. G. Fowler, M. Mariantoni, J. M. Martinis, A. N. Cleland, *Physical Review A* **86**, 032324 (2012).
53. M. D. Reed *et al.*, *Nature* **482**, 382–5 (2012).
54. Y. P. Zhong *et al.*, *Nature Communications* **5** (2014).
55. J. M. Chow *et al.*, *Nature Communications* **5**, 4015 (2014).
56. A. Córcoles *et al.*, en, *Nature Communications* **6**, 6979 (2015).
57. J. Kelly *et al.*, *Nature* **519**, 66–69 (2015).
58. J. F. Poyatos, J. I. Cirac, P. Zoller, *Physical Review Letters* **77**, 4728–4731 (1996).
59. F. Verstraete, M. M. Wolf, J. Ignacio Cirac, *Nature Physics* **5**, 633–636 (2009).
60. S. O. Valenzuela *et al.*, *Science* **314**, 1589–92 (2006).
61. K. W. Murch *et al.*, *Physical Review Letters* **109**, 183602 (2012).
62. S. Hacohen-Gourgy, V. Ramasesh, C. De Grandi, I. Siddiqi, S. M. Girvin, 5 (2015).
63. S. Shankar *et al.*, *Nature* **504**, 419–22 (2013).
64. Z. Leghtas *et al.*, *Science* **347**, 853–7 (2015).
65. A. Einstein, M. Born, H. Born, *The Born-Einstein Letters: Correspondence between Albert Einstein and Max and Hedwig Born from 1916 to 1955 with commentaries by Max Born*. (Macmillian, London, 1971), p. 240.
66. R. Littlejohn, in *Physics 221 Course Notes* (Berkeley, CA, 2011), chap. 2.
67. J. von Neumann, *Mathematische Grundlagen der Quantenmechanik* (Springer Verlag, Berlin, 1932), p. 262.
68. W. Gerlach, O. Stern, *Zeitschrift für Physik* **9**, 349–352 (1922).
69. A. N. Korotkov, *Physical Review B* **60**, 5737–5742 (1999).
70. A. N. Korotkov, *Physical Review B* **63**, 115403 (2001).
71. R. Schack, T. Brun, C. M. Caves, *Physical Review A* **64**, 1–4 (2001).
72. A. N. Jordan, A. N. Korotkov, *Physical Review B* **74**, 1–13 (2006).
73. C. A. Fuchs, R. Schack, *Reviews of Modern Physics* **85**, 1693–1715 (2013).
74. A. N. Korotkov, *Physical Review B* **63**, 15 (2000).
75. A. A. Clerk, M. H. Devoret, S. M. Girvin, F. Marquardt, R. J. Schoelkopf, *Reviews of Modern Physics* **82**, 1155–1208 (2010).

76. H. M. Wiseman, G. J. Milburn, *Quantum Measurement and Control* (Cambridge University Press, 2009), p. 476.
77. C. W. Gardiner, M. J. Collett, *Physical Review A* **31**, 3761–3774 (1985).
78. V. B. Braginsky, F. Y. Khalili, *Quantum Measurement*, ed. by K. S. Thorne (Cambridge University Press, Cambridge, UK, 1992).
79. K. Jacobs, D. A. Steck, *Contemporary Physics* **47** (2007).
80. D. T. Gillespie, *American Journal of Physics* **64** (1996).
81. G. Lindblad, *Communications in Mathematical Physics* **48**, 119–130 (1976).
82. P. G. Kwiat *et al.*, *Physical Review Letters* **75**, 4337–4341 (1995).
83. Z. Y. Ou, L. Mandel, *Physical Review Letters* **61**, 50–53 (1988).
84. Y. H. Shih, C. O. Alley, *Physical Review Letters* **61**, 2921–2924 (1988).
85. A. Einstein, B. Podolsky, N. Rosen, *Physical Review* **47**, 777–780 (1935).
86. J. S. Bell, *Speakable and Unspeakable in Quantum Mechanics* (Cambridge University Press, Cambridge, UK, 1988), p. 290.
87. R. Horodecki, P. Horodecki, M. Horodecki, K. Horodecki, *Reviews of Modern Physics* **81**, 865–942 (2009).
88. B. Hensen *et al.*, *Nature* **526**, 682–686 (2015).
89. L. K. Shalm *et al.*, *Physical Review Letters* **115**, 250402 (2015).
90. M. Giustina *et al.*, *Physical Review Letters* **115**, 250401 (2015).
91. P. W. Shor, *SIAM Journal on Computing* **26**, 1484–1509 (1997).
92. L. K. Grover, presented at the Proceedings of the twenty-eighth annual ACM symposium on Theory of computing - STOC '96, pp. 212–219.
93. A. K. Ekert, *Physical Review Letters* **67**, 661–663 (1991).
94. N. Gisin, G. Ribordy, W. Tittel, H. Zbinden, *Reviews of Modern Physics* **74**, 145–195 (2002).
95. L.-M. Duan, M. D. Lukin, J. I. Cirac, P. Zoller, *Nature* **414**, 413–418 (2001).
96. B. P. Lanyon *et al.*, *Nature Chemistry* **2**, 106–111 (2010).
97. R. Blatt, C. F. Roos, *Nature Physics* **8**, 277–284 (2012).
98. J. R. McClean, J. Romero, R. Babbush, A. Aspuru-Guzik, *New Journal of Physics* **18**, 023023 (2016).
99. I. Georgescu, S. Ashhab, F. Nori, *Reviews of Modern Physics* **86**, 153–185 (2014).
100. S. J. van Enk, N. Lütkenhaus, H. J. Kimble, *Physical Review A* **75**, 1–14 (2007).
101. O. Gühne, G. Tóth, *Physics Reports* **474**, 1–75 (2009).

102. C. H. Bennett, D. P. DiVincenzo, J. A. Smolin, W. K. Wootters, *Physical Review A* **54**, 3824–3851 (1996).
103. M. Lewenstein, B. Kraus, J. I. Cirac, P. Horodecki, *Physical Review A* **62**, 052310 (2000).
104. J. F. Clauser, M. A. Horne, A. Shimony, R. A. Holt, *Physical Review Letters* **23**, 880–884 (1969).
105. J. S. Bell, in *Speakable and Unspeakable in Quantum Mechanics: Collected Papers on Quantum Philosophy* (Cambridge University Press, Cambridge, U.K., 1987), chap. 4, pp. 29–39.
106. J. S. Bell, *Physics* **1**, 195–200 (1964).
107. W. K. Wootters, *Physical Review Letters* **80**, 2245–2248 (1998).
108. J. J. Sakurai, *Modern quantum mechanics* (Addison-Wesley, 2nd, 1994), p. 550.
109. W. K. Wootters, *Quantum Information and Computation* **1**, 27–44 (2001).
110. L. Jakóbczyk, A. Jamróz, *Physics Letters A* **347**, 180–190 (2005).
111. R. Jozsa, *Journal of Modern Optics* **41**, 2315–2323 (1994).
112. R. P. Feynman, A. Zee, *QED : the strange theory of light and matter* (Princeton University Press, Princeton, NJ, 1985), p. 192.
113. D Vion *et al.*, *Science* **296**, 886–9 (2002).
114. J. Koch *et al.*, *Physical Review A* **76**, 042319 (2007).
115. H. Paik *et al.*, *Physical Review Letters* **107**, 240501 (2011).
116. J. E. Mooij, T. P. Orlando, L Levitov, L. Tian, *Science* **285**, 1036–1039 (1999).
117. V. E. Manucharyan, J. Koch, L. I. Glazman, M. H. Devoret, *Science* **326**, 113–6 (2009).
118. J. Gambetta *et al.*, *Physical Review A* **77**, 012112 (2008).
119. D. Schuster, PhD thesis, Yale University, 2006, p. 255.
120. D. H. Slichter, PhD thesis, University of California, Berkeley, 2011, p. 196.
121. M. Devoret, B. Huard, R. Schoelkopf, L. F. Cugliandolo, Eds., *Quantum Machines: Measurement and Control of Engineered Quantum Systems* (Oxford University Press, 2014).
122. M. D. Reed, PhD thesis, Yale University, 2013, arXiv: 1311.6759v1.
123. J. M. Gambetta, J. M. Chow, M. Steffen, 10 (2015).
124. B. D. Josephson, *Physics Letters* **1**, 251–253 (1962).
125. S. M. Girvin, in *Quantum Machines: Measurement and Control of Engineered Quantum Systems*, ed. by M. H. Devoret, B. Huard, R. Schoelkopf, L. F. Cugliandolo (Oxford University Press, Oxford, UK, 2011), chap. 3.

126. F. Motzoi, J. M. Gambetta, P. Rebentrost, F. K. Wilhelm, *Physical Review Letters* **103**, 1–4 (2009).
127. V. Vesterinen, O. P. Saira, A. Bruno, L. DiCarlo, arXiv: 1405.0450 (2014).
128. J. M. Gambetta, F. Motzoi, S. T. Merkel, F. K. Wilhelm, *Physical Review A* **83**, 1–15 (2011).
129. M. H. Goerz, F. Motzoi, K. B. Whaley, C. P. Koch, arXiv: 1606.08825 (2016).
130. M. Steffen *et al.*, *Physical Review Letters* **105**, 100502 (2010).
131. M. Stern *et al.*, *Physical Review Letters* **113**, 123601 (2014).
132. J. S. Birenbaum, PhD thesis, University of California, Berkeley, 2014, p. 162.
133. D. Sank *et al.*, arXiv: 1606.05721 (2016).
134. G. Johansson, T. Bauch, *Quantized electromagnetic field and the Jaynes-Cummings Hamiltonian*, 2012.
135. M. D. Reed *et al.*, *Physical Review Letters* **105**, 173601 (2010).
136. D. Walls, G. J. Milburn, Eds., *Quantum Optics* (Springer Berlin Heidelberg, Berlin, Heidelberg, 1994).
137. J. Gambetta *et al.*, *Physical Review A* **74**, 1–14 (2006).
138. A. N. Korotkov, in *Quantum Machines: Measurement and Control of Engineered Quantum Systems*, ed. by M. H. Devoret, B. Huard, R. Schoelkopf, L. F. Cugliandolo (Oxford University Press, 2014), chap. 17.
139. H. M. Wiseman, G. J. Milburn, *Physical Review A* **47**, 646 (1993).
140. M. A. Castellanos-Beltran, K. D. Irwin, G. C. Hilton, L. R. Vale, K. W. Lehnert, *Nature Physics* **4**, 929–931 (2008).
141. M. Hatridge, R. Vijay, D. H. Slichter, J. Clarke, I. Siddiqi, *Physical Review B* **83**, 134501 (2011).
142. J. Y. Mutus *et al.*, *Applied Physics Letters* **104**, 263513 (2014).
143. *Applied Physics Letters* **107**, 262601 (2015).
144. F. D. O. Schackert, PhD thesis, Yale University, 2013, p. 159.
145. N. Roch *et al.*, *Physical Review Letters* **108**, 147701 (2012).
146. B. Abdo, A. Kamal, M. Devoret, *Physical Review B* **87**, 014508 (2013).
147. N. Bergeal *et al.*, *Nature* **465**, 64–68 (2010).
148. C Macklin *et al.*, en, *Science* **350**, 307–10 (2015).
149. A. Dewes *et al.*, *Physical Review Letters* **108**, 057002 (2012).
150. M. Neeley *et al.*, *Nature* **467**, 570–3 (2010).
151. R Barends *et al.*, *Nature* **508**, 500–3 (2014).

152. J. M. Chow *et al.*, *Physical Review Letters* **107**, 080502 (2011).
153. A Fedorov, L Steffen, M Baur, M. P. da Silva, A Wallraff, *Nature* **481**, 170–2 (2012).
154. D Ristè *et al.*, *Nature* **502**, 350–4 (2013).
155. A. F. van Loo *et al.*, *Science* **342**, 1494–6 (2013).
156. R. Ruskov, A. Korotkov, *Physical Review B* **67**, 241305 (2003).
157. H.-A. Engel, D. Loss, *Science* **309**, 586–8 (2005).
158. B. Trauzettel, A. Jordan, C. Beenakker, M. Büttiker, *Physical Review B* **73**, 235331 (2006).
159. C. L. Hutchison, J. M. Gambetta, A. Blais, F. K. Wilhelm, en, *Canadian Journal of Physics* **87**, 225–231 (2009).
160. K. Lalumière, J. M. Gambetta, A. Blais, *Physical Review A* **81**, 040301 (2010).
161. F. Helmer, F. Marquardt, *Physical Review A* **79**, 052328 (2009).
162. C. W. Chou *et al.*, *Nature* **438**, 828–32 (2005).
163. J. Hofmann *et al.*, *Science* **337**, 72–5 (2012).
164. D. L. Moehring *et al.*, *Nature* **449**, 68–71 (2007).
165. H Bernien *et al.*, *Nature* **497**, 86–90 (2013).
166. J. Kerckhoff, L. Boutingen, A. Silberfarb, H. Mabuchi, *Physical Review A* **79** (2009).
167. N Roch *et al.*, *Physical Review Letters* **112**, 170501 (2014).
168. C. Hong, Z. Ou, L. Mandel, *Physical Review Letters* **59**, 2044–2046 (1987).
169. W. Mao, D. V. Averin, R. Ruskov, A. N. Korotkov, *Physical Review Letters* **93**, 056803 (2004).
170. N. S. Williams, A. N. Jordan, *Physical Review A* **78**, 062322 (2008).
171. S. G. Hofer, D. V. Vasilyev, M. Aspelmeyer, K. Hammerer, *Physical Review Letters* **111**, 170404 (2013).
172. A. N. Korotkov, *Physical Review A* **65**, 052304 (2002).
173. C. Sayrin *et al.*, *Nature* **477**, 73–77 (2011).
174. D. Ristè, C. C. Bultink, K. W. Lehnert, L. DiCarlo, *Physical Review Letters* **109**, 240502 (2012).
175. R Vijay *et al.*, *Nature* **490**, 77–80 (2012).
176. P. Campagne-Ibarcq *et al.*, *Physical Review X* **3**, 021008 (2013).
177. L. Martin, F. Motzoi, H. Li, M. Sarovar, K. B. Whaley, *Physical Review A* **92**, 062321 (2015).
178. Z. Liu *et al.*, *Physical Review A* **82**, 032335 (2010).

179. F. Motzoi, K. B. Whaley, M. Sarovar, *Physical Review A* **92**, 032308 (2015).
180. J. E. Johnson *et al.*, *Physical Review Letters* **109**, 050506 (2012).
181. J. M. Chow *et al.*, *Physical Review A* **81**, 062325 (2010).
182. K. Banaszek, G. M. D'Ariano, M. G. A. Paris, M. F. Sacchi, *Physical Review A* **61**, 010304 (1999).
183. M. Sarovar, H.-S. Goan, T. Spiller, G. Milburn, *Physical Review A* **72**, 1–10 (2005).
184. K. W. Murch, S. J. Weber, C. Macklin, I. Siddiqi, *Nature* **502**, 211–4 (2013).
185. S. J. Weber *et al.*, *Nature* **511**, 570–3 (2014).
186. S. J. Weber, K. W. Murch, M. E. Kimchi-Schwartz, N. Roch, I. Siddiqi, *Comptes Rendus Physique* **17**, 766–777 (2016).
187. P. Campagne-Ibarcq *et al.*, *Physical Review X* **6**, 011002 (2016).
188. A. Chantasri, M. E. Kimchi-Schwartz, N. Roch, I. Siddiqi, A. N. Jordan, arXiv: 1603.09623 (2016).
189. H. Carmichael, *Physical Review Letters* **70**, 2273–2276 (1993).
190. C. Gardiner, *Physical Review Letters* **70**, 2269–2272 (1993).
191. J. Kerckhoff, K. Lalumière, B. J. Chapman, A. Blais, K. W. Lehnert, *Physical Review Applied* **4**, 034002 (2015).
192. K. Sliwa *et al.*, *Physical Review X* **5**, 041020 (2015).
193. W. Heisenberg, *Physics and Philosophy: The Revolution in Modern Science* (Harper & Row, New York, NY, 1958), p. 256.
194. Y. Lin *et al.*, *Nature* **504**, 415–8 (2013).
195. H. Krauter *et al.*, *Physical Review Letters* **107**, 080503 (2011).
196. E. Holland *et al.*, *Physical Review Letters* **115**, 180501 (2015).
197. J. Cohen, M. Mirrahimi, *Physical Review A* **90**, 062344 (2014).
198. E. Kapit, J. T. Chalker, S. H. Simon, *Physical Review A* **91**, 062324 (2015).
199. J. Kerckhoff, H. I. Nurdin, D. S. Pavlichin, H. Mabuchi, *Physical Review Letters* **105**, 040502 (2010).
200. M. Mirrahimi *et al.*, en, *New Journal of Physics* **16**, 045014 (2014).
201. C. Aron, M. Kulkarni, H. E. Türeci, *Physical Review A* **90**, 062305 (2014).
202. M. Boissonneault, J. M. Gambetta, A. Blais, *Physical Review A* **79**, 013819 (2009).
203. C. Aron, M. Kulkarni, H. E. Türeci, *Physical Review X* **6**, 011032 (2016).
204. B. Abdo *et al.*, *Physical Review Letters* **112**, 167701 (2014).
205. A. Silberfarb, P. S. Jessen, I. H. Deutsch, *Physical Review Letters* **95**, 030402 (2005).

206. D. Gross, Y.-K. Liu, S. T. Flammia, S. Becker, J. Eisert, *Physical Review Letters* **105**, 150401 (2010).
207. A. Smith *et al.*, *Physical Review A* **87**, 030102 (2013).
208. F. Motzoi, E. Halperin, X. Wang, K. B. Whaley, S. Schirmer, 9 (2015).